

TOWARDS ADVERSARIAL ROBUSTNESS OF DEEP VISION ALGORITHMS



Hanshu Yan

(*M.Sc., NUS; B.Eng. & B.Sc., BUAA*)

A thesis submitted for the degree of

Doctor of Philosophy

Department of Electrical and Computer Engineering

National University of Singapore

Supervisor:

Associate Professor Vincent Y. F. Tan

Examiners:

Assistant Professor Bryan Hooi Kuen-Yew

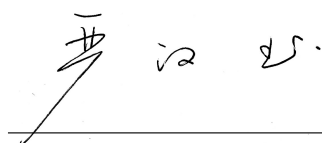
Assistant Professor Xinchao Wang

November 2022

Declaration

I hereby declare that except where specific reference is made to the work of others, the contents of this thesis are original and have not been submitted in whole or in part for consideration for any other degree or qualification in this or any other university. This thesis is my own work and contains nothing which is the outcome of work done in collaboration with others, except as specified in the text and Acknowledgements. I have duly acknowledged all the sources of information that have been used in the thesis.

YAN HANSHU

A handwritten signature in black ink, appearing to be 'YAN HANSHU' in stylized Chinese characters, written over a horizontal line.

Hanshu Yan
(*M.Sc., NUS; B.Eng.& B.Sc., BUAA*)

November 2022

Acknowledgements

This has been a happy, fortunate, and fruitful journey. It is also long and, sometimes, arduous. I am very grateful for the help of many individuals. It would have been much longer without their support.

I would like to thank my supervisors, Prof. Vincent Y. F. Tan and Dr. Jiashi Feng, for teaching me research thinking and supporting me in pursuing my research interests. They taught me to think deeply about the value and feasibility of potential problems. They scheduled weekly meetings to discuss ongoing projects and gave me suggestions on promising research directions. I have benefitted from their broad range of knowledge and deep insights into research problems. These help me establish my long-term research objectives. I also want to thank them for teaching me to write academic papers rigorously and present ideas cogently. Vincent always spares no effort to help me with English and mathematical writing. I am pleased that my writing and presentation skills have improved significantly during the past four years. Besides, I am grateful that they help me build connections with many brilliant researchers in academia and industry. Without the support and encouragement of my supervisors, this thesis would never have happened. They are excellent supervisors and good friends (良师益友 in Chinese).

I would like to express my sincere gratitude to Dr. Jingfeng Zhang, Dr. Gang Niu, and Prof. Masashi Sugiyama from RIKEN-AIP and the University of Tokyo. I met with Jingfeng to discuss the robustness of deep neural networks when he was doing his Ph.D. in NUS. We were both interested in developing robust network architectures. After he joined the RIKEN-AIP, we carried out a series of collaborations to robustify deep vision algorithms. I truly appreciated that Prof. Sugiyama and Dr. Niu joined the discussion, helped examine the technical reasonableness, and edited research papers. Working with the team was a memorable and invaluable experience for my Ph.D.

I would thank my friends in Vincent's group and Jiashi's group. They created a homely atmosphere where we support, inspire, and encourage each other. I particularly appreciate two individuals, Dr. Junhao Liew and Ms. Haiyun He. Junhao has always encouraged and comforted me like a big brother when the going gets tough. He also shared with me his experience and lessons in research unreservedly. Haiyun and I are in the same class. We helped each other in curriculum modules and collaborated on research work. The collaboration has been fruitful and enjoyable.

I hope we can continue working together in the future. I also want to thank my lab mates, Jiawei Du, Mengjiun Chiou, Kuangqi Zhou, Yifan Zhang, Yanfei Dong, Dapeng Hu, Jian Liang, Kaixin Wang, Yujun Shi, Pan Zhou, and others, for the inspiring discussions and far too many things to mention here.

I would like to thank many other students from different departments at NUS. It has been a wonderful experience to extend my research areas and apply deep learning techniques to scientific and engineering problems.

Lastly, I am extremely indebted to my parents for their love, and the support in my pursuits and decisions. I am also very grateful to my girlfriend, Tan Ye, for her deep love, unwavering support, and company. Words cannot express my love and gratitude to all of them.

Table of contents

Summary	viii
List of tables	x
List of figures	xii
List of Symbols	xiii
1 Introduction	1
1.1 Background	3
1.1.1 Adversarial Robustness	4
1.1.2 Robustifying Deep Neural Networks	7
1.2 Thesis Focus and Main Contributions	9
1.3 Organization of Thesis	12
2 Towards Adversarially Robust Deep Image Denoising	13
2.1 Introduction	14
2.2 Notation and Background	16
2.3 ObsAtk for Robustness Evaluation	18
2.3.1 Observation-based Zero-mean Attack	19
2.3.2 Robustness Evaluation via ObsAtk	21
2.4 Robust and Generalizable Denoising via HAT	23
2.4.1 Hybrid Adversarial Training	24
2.4.2 Robustness Enhancement via HAT	25
2.4.3 Robustness Benefits Generalization to Unseen Noise	27
2.5 Chapter Summary	29
2.6 Appendices	30
2.6.1 Two-step Projection	30
2.6.2 Experiments of Robustness Enhancement on Set12 and Kodak24	33
2.6.3 Ablation study	34
2.6.4 Visual results of real-world noise removal	37

3	On Robustness of Neural Ordinary Differential Equations	38
3.1	Introduction	39
3.2	Preliminaries on neural ODE	42
3.3	An empirical study on the robustness of ODEnets	43
3.3.1	Experimental settings	44
3.3.2	Robustness of ODEnets trained only on non-perturbed images	46
3.3.3	Robustness of ODEnets trained on original images together with Gaussian perturbations	47
3.3.4	Insights on the robustness of ODEnets	49
3.4	TisODE: boosting the robustness of neural ODEs	50
3.4.1	Time-invariant steady neural ODEs	50
3.4.2	Evaluating robustness of TisODE-based classifiers	53
3.4.3	TisODE - A generally applicable drop-in technique for improving the robustness of deep networks	54
3.5	Related works	56
3.6	Chapter Summary	58
3.7	Appendices	58
3.7.1	Networks used on the MNIST, the SVHN, and the ImgNet10 datasets	58
3.7.2	The Construction of ImgNet10 dataset	59
3.7.3	Gronwall's Inequality	59
3.7.4	More experimental results	60
4	Improving Adversarial Robustness of CNNs via Channel-wise Importance- based Feature Selection	63
4.1	Introduction	64
4.2	Related Works	67
4.3	Channel-wise Importance-based Feature Selection	70
4.3.1	Non-robust CNNs vs. Robustified CNNs: A Channel-wise Activation Perspective	70
4.3.2	Importance-based Channel Adjustment	72
4.3.3	Verification of Hypothesis \mathcal{H} on Robustness Enhancement	76
4.4	Experiments	78
4.4.1	Robustness Evaluation	78
4.4.2	Ablation Study	83
4.5	Chapter Summary	84
4.6	Appendices	85
4.6.1	Details on Visualizing Channel-wise Activations	85
4.6.2	Robustness Evaluation on CIFAR10	86
4.6.3	Robustness Evaluation on SVHN	93
4.6.4	More Results on FMNIST	94

4.6.5	More Results on Ablation Study	95
5	Conclusion	99
5.1	Summary of Contributions	99
5.2	Recommendations for Future Research	100
	References	103

Towards Adversarial Robustness of Deep Vision Algorithms

Hanshu Yan

Submitted to the Department of Electrical and Computer Engineering in May 2022,
in partial fulfillment of the requirements for the degree of Doctor of Philosophy

Summary

Deep learning methods have achieved great successes in solving computer vision tasks and they have been widely utilized in artificially intelligent systems for image processing, analysis, and understanding. However, deep neural networks (DNNs) have been shown to be vulnerable to adversarial perturbations in input data. The security issues of deep neural networks have thus come to the fore. It is imperative to comprehensively study the adversarial robustness of deep vision algorithms. This thesis focuses on the robustness of deep classification models and deep image denoisers.

For image denoising, we systematically investigate the robustness of deep image denoisers. Specifically, we propose a novel attack method, observation-based zero-mean attack (ObsAtk), that considers the zero-mean assumption of natural noise, to generate adversarial perturbations of noisy input images. We develop an effective and theoretically-grounded PGD-based optimization technique to implement ObsAtk. With ObsAtk, we propose the hybrid adversarially training (HAT) to enhance the robustness of deep image denoisers. Extensive experiments demonstrate the effectiveness of HAT. Furthermore, we explore the connection between the adversarial robustness of denoisers and the adaptivity to unseen types of real-world noise. We find that deep denoisers that are HAT-trained only with synthetic noisy data can generalize well to unseen types of noise. The noise removal capabilities are even comparable to the denoisers trained with true real-world noise.

For image classification, we explore novel robust architectures other than vanilla convolutional neural networks (CNNs). First, we study the robustness of neural ordinary differential equations (NODE). We empirically demonstrate that NODE-based classifiers show superior robustness against input perturbations in comparison to CNN-based classifiers. To further boost the robustness of NODE-based models, we introduce the time-invariant property to NODEs and impose a steady-state constraint to regularize the flow of ODEs on perturbed data. We demonstrate that the resultant model, dubbed as time-invariant steady neural ODE (TisODE), is more robust than the vanilla NODE.

Second, we also investigate the robustness of vanilla CNNs from the perspective of channel-wise activations and propose a feature selection mechanism to enhance

the robustness of vanilla CNNs. In particular, we compare the channel-wise activations of normally-trained classifiers when dealing with natural and adversarial data. We observe that adversarial data mislead the deep classifiers by over-activating negatively-relevant (NR) channels but under-activating positively-relevant (PR) ones. We also compare the channel-wise activations of normally-trained models to the adversarially-trained ones and observe that adversarial training robustifies models by promoting the under-activated PR channels and suppressing the over-activated NR ones. Thus, we hypothesize that scaling the activations of channels corresponding to their relevances to the true categories improves the robustness. To examine this hypothesis, we develop a novel channel manipulation technique, namely channel-wise importance-based feature selection (CIFS), that can scale channels' activations by generating non-negative multipliers based on their relevances. Extensive experimental results verify the hypothesis and the superior robustness of CIFS-modified CNNs.

In summary, this thesis systematically studies the robustness of deep vision algorithms, including robustness evaluation (ObsAtk), robustness improvement (HAT, TisODE, and CIFS), and the connection between adversarial robustness and generalization capability to new domains.

List of tables

2.1	The average PSNR (in dB) results of DnCNN denoisers on the gray-scale and RGB datasets.	23
2.2	Robustness comparison between normally and adversarially-trained DnCNN-B denoisers on the gray-scale Set68 dataset.	26
2.3	Robustness comparison between normally and adversarially-trained DnCNN-B denoisers on the RGB BSD68 dataset.	27
2.4	Comparison of different methods for denoising real-world noisy images in terms of PSNR (dB).	27
2.5	The average PSNR (in dB) results of DnCNN-B denoisers on the gray-scale Set12 dataset.	34
2.6	The average PSNR (in dB) results of DnCNN-C denoisers on the RGB Kodak24 dataset.	34
3.1	Robustness comparison between CNNs and ODEnets.	47
3.2	Robustness comparison of different models trained with Gaussian noisy images.	48
3.3	Robustness improvement via TisODE.	53
3.4	Robustness improvement via TisODE in conjunction with other techniques.	55
3.5	The architectures of the ODEnets on different datasets.	59
3.6	The corresponding indexes to each class in the original ImageNet dataset	60
3.7	Robustness comparison of different models under adversarial training.	61
3.8	Robustness improvement on CIFAR10.	61
3.9	The architecture of the ODEnet on CIFAR10.	62
4.1	Robustness comparison of defense methods on CIFAR10.	80
4.2	Robustness comparison of defense methods on SVHN.	81
4.3	Robustness comparison of defense methods trained with FAT on CIFAR10.	82
4.4	Top- k accuracies (%) against adversarial attacks on CIFAR10 of an adversarially trained ResNet-18.	83

4.5	Robustness comparison (%) of importance assessment based on top- k results.	84
4.6	Robustness comparison (AutoAttack) of defense methods on CIFAR10.	90
4.7	Robustness comparison (best-epoch) of defense methods on CIFAR10	91
4.8	Robust accuracies (%) for values of β_{atk} on CIFAR10.	92
4.9	Robustness comparison of vanilla CNNs and their CIFS-modified version under various AT-based strategies.	93
4.10	Robustness comparison (AutoAttack) of defense methods on SVHN.	93
4.11	Robustness comparison (best-epoch) of defense methods on SVHN.	94
4.12	Robustness comparison of defense methods on FMNIST.	95
4.13	Robustness accuracies (%) on CIFAR10 for CIFS with various values of β	96
4.14	Robustness (%) comparison of the positions where CIFS modules are placed.	97
4.15	Robustness comparison (%) of the probe architectures in CIFS modules (at P1-P2).	97

List of figures

2.1	Illustration of ObsAtk.	18
2.2	Vulnerability of normally-trained deep denoisers under adversarial attacks.	21
2.3	Robustness comparison between normally and HAT-trained denoisers.	25
2.4	Illustration of Theorem 2.6.1.	31
2.5	Ablation study on the effect of α in HAT.	35
2.6	Ablation study on the effect of ε in HAT.	35
2.7	Comparison of different denoisers for denoising SIDD-val set.	36
3.1	The architecture of an ODEnet.	40
3.2	No integral curves intersect.	49
3.3	An illustration of the time-invariant property of ODEs.	51
4.1	Comparison of channel activations of adversarial data between normally and adversarially trained models.	68
4.2	Illustration of CIFS.	73
4.3	Comparison of channel activations of adversarial data between non-CIFS and CIFS modified models.	77
4.4	Comparison of training dynamics of non-CIFS and CIFS modified ResNet-18 models.	81
4.5	More comparison of channel activations of adversarial data between normally and adversarially trained models.	87
4.5	More comparison of channel activations of adversarial data between normally and adversarially trained models.	88
4.5	More comparison of channel activations of adversarial data between normally and adversarially trained models.	89
4.6	Robust accuracies (%) of PGD-20 adversarial data for various classes of the CIFAR10 dataset.	90

List of Symbols

Numbers and Arrays

a	A scalar (integer or real)
\mathbf{a}	A vector
\mathbf{A}	A matrix
\mathbf{I}_n	Identity matrix with n rows and n columns
\mathbf{I}	Identity matrix with dimensionality implied by context
$\text{diag}(\mathbf{a})$	A square, diagonal matrix with diagonal given by \mathbf{a}
a	A scalar random variable
\mathbf{a}	A vector-valued random variable
\mathbf{A}	A matrix-valued random variable

Sets

\mathbb{X}	A set
\mathbb{R}	The set of real numbers
$\{0, 1\}$	The set containing 0 and 1
$\{0, 1, \dots, n\}$	The set of all integers between 0 and n
$[a, b]$	The real interval including a and b
$(a, b]$	The real interval excluding a but including b

Calculus

$\frac{dy}{dx}$	Derivative of y with respect to x
$\frac{\partial y}{\partial x}$	Partial derivative of y with respect to x
$\nabla_{\mathbf{x}} y$	Gradient of y with respect to \mathbf{x}
$\nabla_{\mathbf{X}} y$	Matrix derivatives of y with respect to \mathbf{X}
$\frac{\partial f}{\partial \mathbf{x}}$	Jacobian matrix $\mathbf{J} \in \mathbb{R}^{m \times n}$ of $f : \mathbb{R}^n \rightarrow \mathbb{R}^m$
$\nabla_{\mathbf{x}}^2 f(\mathbf{x})$ or $\mathbf{H}(f)(\mathbf{x})$	The Hessian matrix of f at input point \mathbf{x}
$\int f(\mathbf{x}) d\mathbf{x}$	Definite integral over the entire domain of \mathbf{x}
$\int_{\mathbb{S}} f(\mathbf{x}) d\mathbf{x}$	Definite integral with respect to \mathbf{x} over the set \mathbb{S}

Probability and Information Theory

$a \sim P$	Random variable a has distribution P
$\mathbb{E}_{x \sim P}[f(x)]$ or $\mathbb{E}f(x)$	Expectation of $f(x)$ with respect to $P(x)$
$\text{Var}(f(x))$	Variance of $f(x)$ under $P(x)$
$\text{Cov}(f(x), g(x))$	Covariance of $f(x)$ and $g(x)$ under $P(x)$
$H(x)$	Shannon entropy of the random variable x
$D_{\text{KL}}(P \ Q)$	Kullback–Leibler divergence of P and Q
$\mathcal{N}(\mathbf{x}; \boldsymbol{\mu}, \boldsymbol{\Sigma})$	Gaussian distribution over \mathbf{x} with mean $\boldsymbol{\mu}$ and covariance $\boldsymbol{\Sigma}$

Functions

$f : \mathbb{A} \rightarrow \mathbb{B}$	The function f with domain \mathbb{A} and range \mathbb{B}
$f \circ g$	Composition of the functions f and g
$f(\mathbf{x}; \boldsymbol{\theta})$	A function of \mathbf{x} parametrized by $\boldsymbol{\theta}$. (Sometimes we write $f(\mathbf{x})$ and omit the argument $\boldsymbol{\theta}$ to lighten notation)
$\log x$	Natural logarithm of x
$\sigma(x)$	Logistic sigmoid, $\frac{1}{1 + \exp(-x)}$
$\zeta(x)$	Softplus, $\log(1 + \exp(x))$
$\ \mathbf{x}\ _p$	ℓ_p norm of \mathbf{x}
$\mathbb{1}_{\text{condition}}$	is 1 if the condition is true, 0 otherwise

Chapter 1

Introduction

Intelligent systems have revolutionized various domains, including industry, research, and our daily lives [LeCun et al., 2015, Bedi and Toshniwal, 2019, Veres and Moussa, 2019, Wang et al., 2019b]. For example, medical diagnostic systems facilitate health screening and assist doctors to diagnose diseases [Shen et al., 2017]; unmanned underwater vehicles broaden the horizons of scientists and automatically perform subsea operations and sample collections [Moniruzzaman et al., 2017]; smartphones have reinvented daily lives and made it easy to exchange information and connect with people [Abdelhamed et al., 2018, Ma et al., 2019]. Behind the success of intelligent systems, computer vision and other technology play vital roles in processing and analyzing information. Computer vision aims to design algorithms that can enhance and comprehend digital images effectively and efficiently [Krizhevsky et al., 2012, He et al., 2017, 2016]. For example, denoising and deblurring algorithms can improve the visual quality of medical images that are degraded by unknown noise and device movement [Yan et al., 2019, Amini Gougeh et al., 2019]; classification algorithms help to recognize the categories of samples of marine life [Rathi et al., 2017]; generative vision models are able to synthesize fancy objects that do not yet exist in the real world, to create engaging virtual environments [Goodfellow et al., 2014, Kingma and Welling, 2013].

In recent years, deep learning has achieved great successes in computer vision tasks [He et al., 2016, Zhao et al., 2019, Minaee et al., 2021]. For example, deep classification networks have accomplished astonishing performances of real-world image recognition on several benchmark datasets [Liu et al., 2021]; the performances are comparable to human-level recognition capability. Deep image denoising models can remove intense RGB noise and reconstruct high-quality images from extremely low-light shots [Zhang et al., 2017a, Pang et al., 2021]. Due to these impressive results, deep learning-based algorithms have been widely applied to real-world applications, such as digital cameras [Liang et al., 2021], medical imaging systems [Shen et al., 2017], facial recognition systems [Wang and Deng, 2021], and autonomous vehicles [Grigorescu et al., 2020].

Although deep learning algorithms perform very well on various benchmark datasets, they have been shown to be vulnerable and unstable when confronted with uncertainties in data. For example, Gaussian noise corruption in input images [Hendrycks and Dietterich, 2018] degrades the classification performance. Furthermore, Goodfellow [Goodfellow et al., 2015] showed that well-crafted imperceptible adversarial perturbations in input data can completely mislead a well-trained classification model and result in unreasonable predictions. Various sources of uncertainty are ubiquitous and inevitable in real-world applications, including inherent noise and observation errors. In high-stake applications like fraud detection [Raghavan and El Gayar, 2019], medical diagnosis [Shen et al., 2017], and natural disaster prediction [Kang and Choo, 2016], such high sensitivity to perturbations will lead to unacceptable economic losses and other catastrophic consequences. To build reliable and trustworthy intelligent systems, it is imperative to systematically study the robustness of deep vision algorithms.

This thesis focuses on the problem of evaluating and enhancing the robustness of deep vision algorithms against perturbations of input data. In particular, to

examine the sensitivity of deep models against any arbitrary type of input noise, we develop adversarial attack methods to compute the worst-case perturbation with a certain limited budget. The resistance against adversarial perturbations is termed *adversarial robustness*. Besides, to enhance the adversarial robustness of deep models, we devise solutions from the perspectives of network architectures, learning objectives, and training frameworks. Finally, we also explore the connection between adversarial robustness and generalization to new domains and empirically demonstrate that adversarial robustness benefits the models in terms of the ability to adapt to unseen types of data.

1.1 Background

Noise in observed signals is ubiquitous in real-world applications due to intrinsic noise, measuring errors, numerical errors induced in signal processing, etc. Reliable intelligent systems ought to exclude the interference of noise and extract salient task-related information from the noisy observations. To wit, they should not only effectively process and analyze the authentic ground truth but also maintain acceptable performances on corrupted data. The first step toward robust systems is developing methods to evaluate the robustness of deep models. In Section 1.1.1, we introduce existing works that proposed attack methods to craft adversarial noise for the robustness evaluation. We also discuss several metrics for measuring the robustness level by using the attack methods. Based on these robustness metrics, we then introduce several state-of-the-art techniques for robustness improvement in Section 1.1.2.

1.1.1 Adversarial Robustness

Consider a deep neural network (DNN) $\{f_\theta : \theta \in \Theta\}$ mapping an input \mathbf{x} to a target \mathbf{y} . The model is trained to minimize a certain loss function that is measured by particular distance measure $d(\cdot, \cdot)$ between the output $f_\theta(\mathbf{x})$ and the target \mathbf{y} . In critical applications, the DNN should resist small perturbations on the input data and map the perturbed input to a result that is close to the target. The notion of *robustness* has been proposed to measure the resistance of DNNs against slight changes of the input [Szegedy et al., 2014, Goodfellow et al., 2015]. The robustness is characterized by the distance $d(f_\theta(\mathbf{x}'), \mathbf{y})$ between the prediction $f_\theta(\mathbf{x}')$ and the target \mathbf{y} , where the perturbed input \mathbf{x}' is located within a small ρ -neighborhood of the original input \mathbf{x} .

Adversarial Examples It is possible to use various types of random perturbations, such as Gaussian noise and uniform noise, to evaluate robustness. However, we, in reality, are incognizant of the true statistics of real-world noise. DNNs that are robust against random Gaussian noise may be very vulnerable to other types of perturbations. Thus, to comprehensively examine the robustness of deep models, we consider the worst-case perturbations of input data, namely \mathbf{x}' is synthesized by maximizing the distance between its output and the target \mathbf{y} :

$$\mathbf{x}' = \arg \max_{\mathbf{x}' : \|\mathbf{x}' - \mathbf{x}\| \leq \rho} d(f_\theta(\mathbf{x}'), \mathbf{y}). \quad (1.1)$$

The distance $d(f_\theta(\mathbf{y}'), \mathbf{x})$ is an indication of the robustness of f_θ around \mathbf{y} : a small distance implies strong robustness and vice versa. In terms of image classification, the ρ -neighborhood is usually defined by the ℓ_∞ -norm and the distance $d(\cdot, \cdot)$ is measured by the cross-entropy loss [Madry et al., 2018] or a margin loss [Carlini and Wagner, 2017]. For image restoration, such as image denoising and super-resolution, the distance between images is usually measured by the ℓ_2 -norm

[Zhang et al., 2017a]. In addition to the constraint of the limited budget, there may be other constraints that are used in the optimization procedure and depend on the forms of the adversarial perturbations. For example, attackers may add the ℓ_0 -norm to restrict the number of pixels that are allowed to be changed [Croce and Hein, 2019]; attackers may multiply the perturbation with a mask of certain shapes to generate adversarial perturbations with certain semantic meanings, such as adversarial T-shirts. Anyone wearing such T-shirts can protect themselves from malicious person detectors [Xu et al., 2020].

Adversarial Attack Methods In general, the worst-case perturbation \mathbf{x}' can be approximated via backpropagation-based methods, such as Fast Gradient Signed Method (FGSM) [Goodfellow et al., 2015], Iterative-FGSM [Kurakin et al., 2017], and Projected Gradient Descent (PGD) attack [Madry et al., 2018], which approximately solve equation 1.1 via gradient descent methods. However, some deep models may involve randomization modules or non-differentiable operations [Xie et al., 2018]. In this case, backpropagation on its own may not be able to approximate the worst-case perturbations sufficiently accurately. To solve this problem, Athalye et al. [2018] demonstrated that attackers could circumvent the gradient obfuscation problem through the Expectation over Transformation (EoT) technique for randomization methods or the Backward Pass Differentiable Approximate (BPDA) technique for non-differentiable transformations. EoT updates perturbations with the average gradients that are computed by performing multiples times of forward and backward passes; BPDA approximates the gradients of non-differentiable modules by substituting them with differentiable modules.

Considering the case that attackers are not allowed to access the inner information of neural networks, researchers have proposed several black-box and transfer-based attack methods [Guo et al., 2019a, Liu et al., 2016]. Black-box methods usually iteratively update the adversarial perturbations by querying the

target models for a limited number of times; transfer-based methods, instead of diagnosing the target models, attack substitute models to craft the adversarial perturbations. In comparison, gradient-based (white-box) attack methods, if they are allowed to access the gradients of deep models, are usually much stronger than other types of attacks [Tramer et al., 2020] because they are cognizant of the whole information of deep models. To further boost the strength and the adaptivity of attacks, Croce and Hein [2020] proposed to use an ensemble of four white-box and black-box attacks, namely AutoAttack, to reliably evaluate the robustness of deep models.

Robustness Metrics Robustness is measured by the performance of deep models on perturbed input data. The metrics of the robustness of deep models depend on the tasks performed. In semantic-level classification tasks, we usually use the accuracy (or 0-1 loss), $\mathbb{1}[f_{\theta}(x) = y_j]$, to measure the performance. Thus, the robustness of classification models is quantified by the average accuracy of adversarial examples over a test set \mathbb{S} :

$$\overline{\text{Acc}} = \frac{1}{|\mathbb{S}|} \sum_{(\mathbf{x}, \mathbf{y}) \in \mathbb{S}} \mathbb{1}[f_{\theta}(\mathbf{x}') = \mathbf{y}].$$

In pixel-level vision tasks, such as image reconstruction and image segmentation, each pixel has a certain ground-truth value. The metrics are usually defined based on the norm of the difference between pixel-value vectors. For example, in image denoising and deblurring, we use the peak signal-to-noise ratio (PSNR) to quantify the reconstruction quality, where PSNR is defined as:

$$\text{PSNR}(\mathbf{x}, \mathbf{y}) = 10 \cdot \log_{10}\left(\frac{\text{MAX}^2}{\text{MSE}}\right),$$

where MAX represents the maximum possible value of pixels (e.g., 255 for 8-bit unsigned-integer images and 1 for floating-point images) and MSE represents the

mean-squared-loss between vector \mathbf{x} and \mathbf{y} . Thus, we characterize the robustness via the metric of average PSNR over a test set \mathbb{S} :

$$\overline{\text{PSNR}} = \frac{1}{|\mathbb{S}|} \sum_{(\mathbf{x}, \mathbf{y}) \in \mathbb{S}} \text{PSNR}(\mathbf{x}', \mathbf{y}).$$

1.1.2 Robustifying Deep Neural Networks

Deep learning models have been shown to be vulnerable to adversarial attacks under normal training (NT) [Tramer et al., 2020, Yan et al., 2020]. For example, a well-trained image classification model can achieve above 99% accuracy on authentic images from the MNIST test set, but the accuracy will drop to around 0% under some strong attacks like multiple-step PGD and C&W attacks [Madry et al., 2018, Carlini and Wagner, 2017]. To robustify DNNs, researchers have explored a variety of techniques from the perspectives of model training and network architecture design, among others.

Robust Training Robust training methods aim to devise novel training objectives to impose robustness regularization to the resultant models. The original idea of robust training is attributed to Goodfellow et al. [2015], where the authors propose to use the FGSM adversarial examples for model training. However, models trained with FGSM adversarial examples cannot effectively defend other attacks like iteratively-FGSM [Kurakin et al., 2017] and C&W attacks [Carlini and Wagner, 2017]. The formal statement of PGD-adversarial training (AT) is proposed in Madry et al. [2018], where AT is formulated as the following min-max optimization problem,

$$\min_{\theta \in \Theta} \max_{\mathbf{x}': \|\mathbf{x}' - \mathbf{x}\| \leq \rho} d(f_{\theta}(\mathbf{x}'), \mathbf{y}). \quad (1.2)$$

AT aims to guarantee the performance of models on the worst-case perturbed data. In practice, the PGD-AT method generates adversarial examples on the fly

for each mini-batch via PGD attacks. Then, PGD adversarial examples are used to calculate training losses for updating model parameters. The effectiveness of AT has been verified by extensive empirical and theoretical studies [Yan et al., 2021, Gao et al., 2019]. For further improvement, many variants of AT have been proposed in terms of its robustness enhancement [Cai et al., 2018, Wang et al., 2020], generalization to non-adversarial data [Zhang et al., 2019b, 2020], and computational efficiency [Shafahi et al., 2019, Wong et al., 2020]. Wang et al. [2020] proposed the misclassification-aware-adversarial-training (MART) to further robustify DNNs, where MART simultaneously applies the misclassified natural data and the adversarial data for model training. To mitigate the trade-off between the different accuracies on adversarial data and authentic non-perturbed data, Zhang et al. [2019a] proposed the TRADES method that minimizes the classification loss on authentic data and the local sensitivity of deep model around training data at the same time. Additionally, due to the high extra computational overhead incurred by generating strong adversarial examples, Shafahi et al. [2019] proposed Free-AT to accelerate AT by reusing the gradient information computed when updating model parameters. AT is a generally applicable framework that can be used in different tasks, including computer vision and natural language processing [Zhu et al., 2019, Gan et al., 2020], AT-based methods thus have become the default option for enhancing the robustness of DNNs.

In addition, some other works introduced various types of regularization for training models, such as layer-wise feature matching [Sankaranarayanan et al., 2018, Liao et al., 2018, Kannan et al., 2018], low-rank representations [Sanyal et al., 2020, Mustafa et al., 2019], attention map alignment [Xu et al., 2019], and Lipschitz regularity [Virmaux and Scaman, 2018, Cissé et al., 2017]. These types of regularization can work in conjunction with AT and benefit the models' robustness.

Robust Architecture Design Apart from robust training strategies, researchers also have explored robust network architectures. A line of works propose to utilize pre-processing modules to remove adversarial noise from images or introduce randomness to ruin the adversarial patterns [Samangouei et al., 2018, Yang et al., 2019, Xie et al., 2018], so that adversarial perturbations will not affect the pre-trained models. Although these types of methods can defend pure gradient backpropagation attacks, such as I-FGSM, they can be easily circumvented by adaptive attacks like BPDA or EoT [Athalye et al., 2018]. Another line of works attempt to modify the basic components of DNNs. For example, Guo et al. [2018] demonstrated that the robustness of DNNs can be improved by appropriately designed higher model sparsity. Xie et al. [2019] performed feature denoising at the end of convolutional layers to ameliorate the adversarial effects on feature maps. Zoran et al. [2020] used the spatial attention mechanism to highlight important regions in feature maps. Existing empirical works mostly focus on the spatial modification of feature maps in convolutional neural networks (CNNs). The channel-wise selection of convolutional layers and other families of models, such as neural ordinary differential equations [Chen et al., 2018], energy-based models [Du and Mordatch, 2019], and vision transformers [Liu et al., 2021], have been underexplored.

1.2 Thesis Focus and Main Contributions

This thesis systematically studies the adversarial robustness of deep vision algorithms, from the perspective of robustness evaluation, robustness enhancement, and the connection between robustness and the adaptation to unseen data. We solve the robustness evaluation and enhancement problems by developing a novel PGD-based optimization method to perform attacking, exploring robust network architectures, and effective adversarial training strategies.

- Since image denoising algorithms have been extensively used to enhance image quality in computer vision systems, it is necessary to examine the robustness of deep image noises against adversarial corruptions. We propose the observation-based zero-mean attack (ObsAtk), which considers the zero-mean assumption of natural noise, for robustness evaluation. By using ObsAtk, we develop a novel adversarial training strategy, hybrid adversarial training (HAT), to enhance the robustness of deep image denoisers. Besides, we reveal that deep image denoisers that are adversarially trained with only synthetic data can generalize or adapt well to unseen types of real-world noise. In this case, one can train an effective denoiser without the need to collect a large amount of real-world noisy data for training. This work will be presented at the International Joint Conference on Artificial Intelligence (IJCAI), 2022 [Yan et al., 2022].
- Neural ordinary differential equations (NODE) [Chen et al., 2018], a new family of models, approximate nonlinear mappings by using continuous-time ODEs. They have attracted much attention in various research domains recently due to their desirable properties, such as invertibility and time-continuity. We study the robustness property of NODEs and found that NODE-based image classifiers enjoy superior robustness against random noise and adversarial perturbations in comparison to CNN-based ones. To further boost the robustness of NODEs, we propose time-invariant steady neural ODE (TisODE), which regularizes the flow of neural ODEs via the time-invariant property and a steady-state constraint. We empirically demonstrate that TisODE outperforms vanilla NODEs and can work in conjunction with other robustification techniques. This work appeared at the International Conference on Learning Representations (ICLR), 2020 [Yan et al., 2020].

- In CNN classifiers, channels in deep layers can extract semantic features, and the final predictions are made by aggregating information from various channels. In this case, abnormal activations of channels in deep layers may result in incorrect predictions. To understand the effects of adversarial data on each channel, we compare the activations of channels caused by authentic and adversarial data. We find that natural data tend to over-activate positively-relevant (PR) channels and under-activate negatively-relevant (NR) channels, but adversarial data do the opposite. Here, the relevance of each channel is defined as the gradient of the prediction logit associated with the true label with respect to the activation level. To investigate the effects of adversarial training on channels, we also compare the channel activations between normally-trained and adversarially-trained models. We observe that AT robustifies CNNs by aligning the channel-wise activations of adversarial data with those of their natural counterparts. Given these observations, we hypothesize that suppressing NR channels and promoting PR ones based on their relevances can further enhance the robustness of CNNs. To examine this hypothesis, we propose the Channel-wise Importance-based Feature Selection (CIFS). The CIFS mechanism manipulates channels' activations of certain layers by generating non-negative multipliers to these channels based on their relevances. Extensive experiments on benchmark datasets clearly verify the hypothesis and CIFS's effectiveness in robustifying CNNs. This work appeared at the International Conference on Machine Learning (ICML), 2021 [[Yan et al., 2021](#)].

1.3 Organization of Thesis

In Chapter 2, we propose the ObsAtk to evaluate the robustness of deep image denoisers and develop the HAT to enhance the robustness of deep denoisers by using ObsAtk. In Chapter 3, we demonstrate that NODE-based classifiers are more robust against input perturbations in comparison to CNN-based ones and propose TisODE to further boost the robustness of NODEs. In Chapter 4, we propose the CIFS mechanism to modify CNN-based classifiers and show that CIFS clearly robustifies CNNs against adversarial corruptions. Finally, Chapter 5 concludes this thesis and suggests several promising topics for future research.

Chapter 2

Towards Adversarially Robust Deep Image Denoising

This work systematically investigates the adversarial robustness of deep image denoisers (DIDs), i.e, how well DIDs can recover the ground truth from noisy observations degraded by adversarial perturbations. Firstly, to evaluate DIDs' robustness, we propose a novel adversarial attack, namely Observation-based Zero-mean Attack (ObsAtk), to craft adversarial zero-mean perturbations on given noisy images. We find that existing DIDs are vulnerable to the adversarial noise generated by ObsAtk. Secondly, to robustify DIDs, we propose an adversarial training strategy, hybrid adversarial training (HAT), that jointly trains DIDs with adversarial and non-adversarial noisy data to ensure that the reconstruction quality is high and the denoisers around non-adversarial data are locally smooth. The resultant DIDs can effectively remove various types of synthetic and adversarial noise. We also uncover that the robustness of DIDs benefits their generalization capability on unseen real-world noise. Indeed, HAT-trained DIDs can recover high-quality clean images from real-world noise even without training on real noisy

data. Extensive experiments on benchmark datasets, including Set68, PolyU, and SIDD, corroborate the effectiveness of ObsAtk and HAT.

2.1 Introduction

Image denoising, which aims to reconstruct clean images from their noisy observations, is a vital part of the image processing systems. The noisy observations are usually modeled as the addition between ground-truth images and zero-mean noise maps [Dabov et al., 2007, Zhang et al., 2017a]. Recently, deep learning-based methods have made significant advancements in denoising tasks [Zhang et al., 2017a, Anwar and Barnes, 2019] and have been applied in many areas including medical imaging [Gondara, 2016] and photography [Abdelhamed et al., 2018]. Despite the success of deep denoisers in recovering high-quality images from a certain type of noisy images, we still lack knowledge about their robustness against adversarial perturbations, which may cause severe safety hazards in high-stake applications like medical diagnosis. To address this problem, the first step should be developing attack methods dedicated for denoising to evaluate the robustness of denoisers. In contrast to the attacks for classification [Goodfellow et al., 2015, Madry et al., 2018], attacks for denoising should consider not only the adversarial budget but also some assumptions of natural noise, such as zero-mean, because certain perturbations, such as adding a constant value, do not necessarily result in visual degradation. Although Choi et al. [2021, 2019] studied the vulnerability for various deep image processing models, they directly applied the attack from classification. To the best of our knowledge, no attacks are truly dedicated for the denoising task till now.

To this end, we propose the observation-based zero-mean attack (ObsAtk), which crafts a worst-case zero-mean perturbation for a noisy observation by maxi-

mizing the distance between the output and the ground-truth. To ensure that the perturbation satisfies the adversarial budget and the zero-mean constraints, we utilize the classical projected-gradient-descent (PGD) [Madry et al., 2018] method for optimization, and develop a two-step operation to project the perturbation back into the feasible region. Specifically, in each iteration, we first project the perturbation onto the zero-mean hyperplane. Then, we linearly rescale the perturbation to adjust its norm to be less or equal to the adversarial budget. We examine the effectiveness of ObsAtk on several benchmark datasets and find that deep image denoisers are indeed susceptible to ObsAtk: the denoisers cannot remove adversarial noise completely and even yield atypical artifacts, as shown in Figure 2.2g.

To robustify deep denoisers against adversarial perturbations, we propose an effective adversarial training strategy, namely hybrid adversarial training (HAT), to train denoisers by using adversarially noisy images and non-adversarial noisy images together. The loss function of HAT consists of two terms. The first term ensures the reconstruction performance from common non-adversarial noisy images, and the second term ensures the reconstructions between non-adversarial and adversarial images to be close to each other. Thus, we can obtain denoisers that perform well on both non-adversarial noisy images and their adversarial perturbed versions. Extensive experiments on benchmark datasets verify the effectiveness of HAT.

Moreover, we reveal that adversarial robustness benefits the generalization capability to unseen types of noise, i.e., HAT can train denoisers for real-world noise removal only with synthetic noise sampled from common distributions like Gaussians. That is because ObsAtk searches for the worst-case perturbations around different levels of noisy images, and training with adversarial data ensures the denoising performance on various types of noise. In contrast, other reasonable methods for real-world denoising [Guo et al., 2019b, Lehtinen et al., 2018]

mostly require a large number of real-world noisy data for the training, which are unfortunately not available in some applications like medical radiology. We conduct experiments on several real-world datasets. Numerical and visual results demonstrate the effectiveness of HAT for real-world noise removal.

In summary, there are three main contributions in this work: 1) We propose a novel attack, ObsAtk, to generate adversarial examples for noisy observations, which facilitates the evaluation of the robustness of deep image denoisers. 2) We propose an effective adversarial training strategy, HAT, for robustifying deep image denoisers. 3) We build a connection between adversarial robustness and the generalization to unseen noise, and show that HAT serves as a promising framework for training generalizable deep image denoisers.

2.2 Notation and Background

Deep image denoising During image capturing, unknown types of noise may be induced by physical sensors, data compression, and transmission. Noisy observations are usually modeled as the addition between the ground-truth images and certain zero-mean noise [Dabov et al., 2007, Zhang et al., 2019c], i.e., $\mathbf{y} = \mathbf{x} + \mathbf{v}$ with $\mathbb{E}_Q[\sum_{i=1}^m \mathbf{v}_{[i]}] = 0$, where $\mathbf{v}_{[i]}$ is the i^{th} element of \mathbf{v} . The random vector $\mathbf{x} \in \mathbb{R}^m$ with distribution P denotes a random clean image and the noise $\mathbf{v} \in \mathbb{R}^m$ with a distribution Q satisfies the zero-mean constraint. Denoising techniques aim to recover clean images from their noisy observations [Zhang et al., 2017a, Dabov et al., 2007]. Suppose we are given a training set $\mathbb{S} = \{(\mathbf{y}_j, \mathbf{x}_j)\}_{j=1}^N$ of noisy and clean image pairs sampled from distributions Q and P respectively, we can train a DNN to effectively remove the noise induced by distribution Q from the noisy observations. A series of DNNs have been developed for denoising in recent years, including

DnCNN [Zhang et al., 2017a], FFDNet [Zhang et al., 2018], and RIDNet [Anwar and Barnes, 2019].

In real-world applications [Abdelhamed et al., 2018, Xu et al., 2017], the noise distribution Q is usually unknown due to the complexity of the image capturing procedures; besides, collecting a large number of image pairs (clean/noisy or noisy/noisy) for training sometimes may be unrealistic in safety-critical domains such as medical radiology [Zhang et al., 2019c]. To overcome these, researchers developed denoising techniques by approximating real noise with common distributions like Gaussian or Poisson [Dabov et al., 2007, Zhang et al., 2019c]. To train denoisers that can deal with different levels of noise, where the noise level is measured by the energy-density $\|\mathbf{v}\|_2^2/m$ of noise, the training set may consist of noisy images sampled from a variety of noise distributions [Zhang et al., 2017a], whose expected energy-densities range from zero to certain budget γ^2 (the expected ℓ_2 -norms range from zero to $\gamma\sqrt{m}$). For example, $\mathbb{S}^\gamma = \{(\mathbf{y}_j, \mathbf{x}_j)\}_{j=1}^N$ where $\mathbf{y}_j = \mathbf{x}_j + \mathbf{v}_j$ and \mathbf{x}_j and \mathbf{v}_j are sampled from P and Q respectively and where Q is randomly selected from a set of Gaussian distributions $\mathbb{Q}^\gamma = \{\mathcal{N}(\mathbf{0}, \sigma^2 \mathbf{I}) | \sigma \in [0, \gamma]\}$. The denoiser $f_\theta^\gamma(\cdot)$ trained with \mathbb{S}^γ is termed as an γ -denoiser.

On robustness of deep image denoisers In practice, data storage and transmission may induce imperceptible perturbations on the original data so that the perturbed noise may be statistically slightly different from the noise sampled from the specific original distribution. Although an γ -denoiser can successfully remove noise sampled from $Q \in \mathbb{Q}^\gamma$, the performance of noise removal on the perturbed data is not guaranteed. Thus, we propose a novel attack method, ObsAtk, to assess the adversarial robustness of DIDs in Section 2.3. To robustify DIDs, we propose an adversarial training strategy, HAT, in Section 2.4. HAT-trained DIDs can effectively denoise adversarial perturbed noisy images and preserve good performance on non-adversarial data.

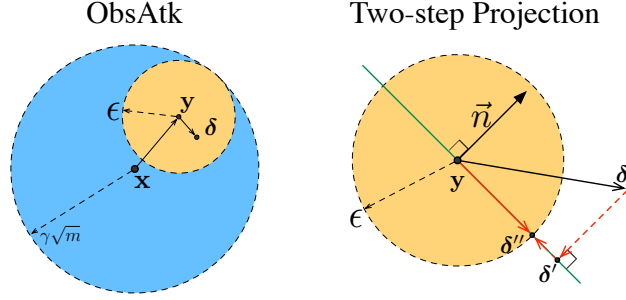


Fig. 2.1 Illustration of ObsAtk. Left: We perturb a noisy observation y of the ground-truth x with an adversarial budget ϵ in the ℓ_2 -norm. For an γ -denoiser, we choose a proper value of ϵ to ensure the norm of the total noise is bounded by $\gamma\sqrt{m}$, where m denotes the image size. Right: The perturbation δ is projected via the two-step operation onto the region defined by the zero-mean and ϵ -ball constraints.

Besides the adversarial robustness issue, it has been shown that γ -denoisers trained with \mathbb{S}^γ cannot generalize well to unseen real-world noise [Lehtinen et al., 2018, Batson and Royer, 2019]. Several methods have been proposed for real-world noise removal, but most of them require a large number of real noisy data for training, e.g., CBDNet (clean/noisy pairs) [Guo et al., 2019b] and Noise2Noise (noisy pairs) [Lehtinen et al., 2018], which is sometimes impractical. In Section 2.4.3, we show that HAT-trained DIDs can generalize well to unseen real noise without the need of utilizing real noisy images for training.

2.3 ObsAtk for Robustness Evaluation

In this section, we propose a novel adversarial attack, Observation-based Zero-mean Attack (ObsAtk), to evaluate the robustness of DIDs. We also conduct experiments on benchmark datasets to demonstrate that normally-trained DIDs are vulnerable to adversarial perturbations.

2.3.1 Observation-based Zero-mean Attack

An γ -denoiser $f_\theta^\gamma(\cdot)$ can generate a high-quality reconstruction $f_\theta^\gamma(\mathbf{y})$ close to the ground-truth \mathbf{x} from a noisy observation $\mathbf{y} = \mathbf{x} + \mathbf{v}$. To evaluate the robustness of $f_\theta^\gamma(\cdot)$ with respect to a perturbation on \mathbf{y} , we develop an attack to search for the worst perturbation $\boldsymbol{\delta}^*$ that degrades the recovered image $f_\theta^\gamma(\mathbf{y} + \boldsymbol{\delta}^*)$ as much as possible. Formally, we need to solve the problem stated in equation 2.1. The optimization problem is subject to *two* constraints: The first constraint requires the norm of $\boldsymbol{\delta}$ to be bounded by a small adversarial budget ε . The second constraint restricts the mean $M(\boldsymbol{\delta})$ of all elements in $\boldsymbol{\delta}$ to be zero. This corresponds to the zero-mean assumption of noise in real-world applications because a small mean-shift does not necessarily result in visual noise. For example, a mean-shift in gray-scale images implies a slight change of brightness. Since the zero-mean perturbation is added to a noisy observation \mathbf{y} , we term the proposed attack as Observation-based Zero-mean Attack (ObsAtk).

$$\boldsymbol{\delta}^* = \arg \max_{\boldsymbol{\delta} \in \mathbb{R}^m} \|f_\theta^\gamma(\mathbf{y} + \boldsymbol{\delta}) - \mathbf{x}\|_2^2, \quad (2.1a)$$

$$\text{s.t. } \|\boldsymbol{\delta}\|_2 \leq \varepsilon, \quad M(\boldsymbol{\delta}) = \frac{1}{m} \sum_{i=1}^m \boldsymbol{\delta}_{[i]} = 0. \quad (2.1b)$$

We solve the constrained optimization problem Eq. equation 2.1 by using the classical projected-gradient-descent (PGD) method. PGD-like methods update optimization variables iteratively via gradient descent and ensure the constraints to be satisfied by projecting parameters back to the feasible region at the end of each iteration. To deal with the ℓ_2 -norm and zero-mean constraints, we develop a two-step operation in Eq. equation 2.2, that first projects the perturbation $\boldsymbol{\delta}$ back to

Algorithm 1 ObsAtk

Input: Denoiser $f_\theta(\cdot)$, ground-truth \mathbf{x} , noisy observation \mathbf{y} , adversarial budget ε , #iterations T , step-size η , minimum pixel value p_{\min} , maximum pixel value

p_{\max}

Output: Adversarial perturbation δ

- 1: $\delta \leftarrow \mathbf{0}$
- 2: **for** $t = 1$ to T **do**
- 3: $\delta \leftarrow \delta + \eta \nabla_\delta \|f_\theta^\gamma(\mathbf{y} + \delta) - \mathbf{x}\|_2^2$;
- 4: $\delta \leftarrow \delta - (\delta^\top \mathbf{n} / \|\mathbf{n}\|_2^2) \mathbf{n}$ where \mathbf{n} is in equation 2.2a
- 5: $\delta \leftarrow \min(\varepsilon / \|\delta\|_2, 1) \delta$;
- 6: $\delta \leftarrow \text{Clip}(\mathbf{y} + \delta, p_{\min}, p_{\max}) - \mathbf{y}$

the zero-mean hyperplane and then projects the result onto the ε -neighborhood.

$$\delta' = \delta - \frac{\delta^\top \mathbf{n}}{\|\mathbf{n}\|_2^2} \mathbf{n}, \quad \text{where } \mathbf{n} = [1, 1, \dots, 1]^\top, \quad (2.2a)$$

$$\delta'' = \min\left(\frac{\varepsilon}{\|\delta'\|_2}, 1\right) \delta'. \quad (2.2b)$$

In each iteration, as shown in Figure 2.1, the first step involves projecting the perturbation δ onto the zero-mean hyperplane. The zero-mean hyperplane consists of all the vectors \mathbf{z} whose mean of all elements equals zero, i.e., $\mathbf{n}^\top \mathbf{z} = 0$, where \mathbf{n} is the length- d all ones vector. Thus, \mathbf{n} is a normal of the zero-mean plane. We can project any vector onto the zero-mean plane via equation 2.2a. The vector δ is first projected along the direction of \mathbf{n} , then its projection δ' onto the zero-mean plane equals itself minus its projection onto \mathbf{n} . The second step involves further projecting δ' back to the ε -ball via linear scaling. If δ' is already within the ε -ball, we keep δ' unchanged. Otherwise, the final projection δ'' is obtained by scaling δ' with a factor $\varepsilon / \|\delta'\|_2$. For any two sets A and B , although the projection onto $A \cap B$ is, in general, not equal to the result obtained by first projecting onto A , then onto B , surprisingly, the following holds for the two sets in equation 2.1b.

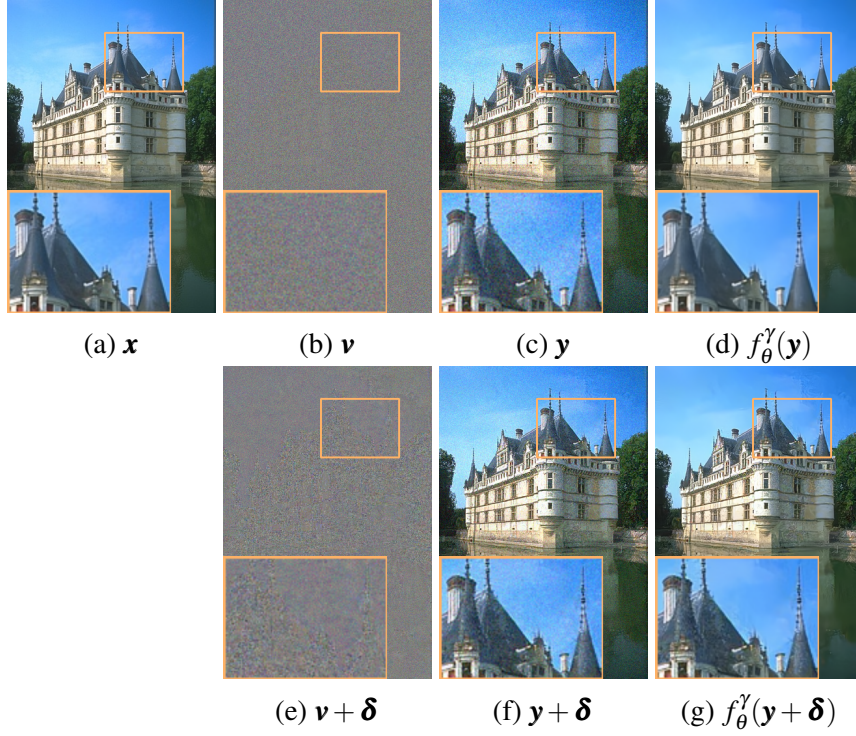


Fig. 2.2 Given a normally-trained denoiser $f_{\theta}^{\gamma}(\cdot)$, from left to right are the ground-truth image \mathbf{x} , Gaussian noise \mathbf{v} , the Gaussian noisy image $\mathbf{y} = \mathbf{x} + \mathbf{v}$, the reconstruction $f_{\theta}^{\gamma}(\mathbf{y})$ from \mathbf{y} , adversarial noise $\mathbf{v} + \boldsymbol{\delta}$, the adversarially noisy image $\mathbf{y} + \boldsymbol{\delta}$, and the reconstruction $f_{\theta}^{\gamma}(\mathbf{y} + \boldsymbol{\delta})$ from $\mathbf{y} + \boldsymbol{\delta}$. Comparing (a), (d) and (g), we observe that $f_{\theta}^{\gamma}(\cdot)$ can effectively remove Gaussian noise but its performance is degraded when dealing with the adversarial noise (noise remains on the roof and strange contours appear in the sky).

Theorem 2.3.1 (Informal) *Given any vector $\boldsymbol{\delta} \in \mathbb{R}^m$, the projection of $\boldsymbol{\delta}$ via the two-step operation in equation 2.2 satisfies the two constraints in equation 2.1b, and the two-step projection is equivalent to the exact projection onto the set defined by equation 2.1b.*

The formal statement and the proof of Theorem 2.3.1 are provided in Appendix 2.6.1. The complete procedure of ObsAtk is summarized in Algorithm 1.

2.3.2 Robustness Evaluation via ObsAtk

We use ObsAtk to evaluate the adversarial robustness of γ -denoisers on several gray-scale and RGB benchmark datasets, including Set12, Set68, BSD68, and

Kodak24. For gray-scale image denoising, we use Train400 to train a DnCNN-B [Zhang et al., 2017a] model, which consists of 20 convolutional layers. We follow the training setting in Zhang *et al.* [Zhang et al. [2017a]] and randomly crop 128×3000 patches in size of 50×50 . Noisy and clean image pairs are constructed by injecting different levels of white Gaussian noise into clean patches. The noise levels σ are uniformly randomly selected from $[0, \gamma]$ with $\gamma = 25/255$. For RGB image denoising, we use BSD432 (BSD500 excluding images in BSD68) to train a DnCNN-C model with the same number of layers as DnCNN-B and but set the input and output channels to be three. Other settings follow those of the training of DnCNN-B.

We evaluate the denoising capability of the γ -denoiser on Gaussian noisy images and their adversarially perturbed versions. The image quality of reconstruction is measured via the peak-signal-noise ratio (PSNR) metric. A large PSNR between reconstruction and ground-truth implies a good performance of denoising. We denote the energy-density of the noise in test images as $\hat{\gamma}^2$ and consider three levels of noise, i.e., $\hat{\gamma} = 25/255$, $15/255$, and $10/255$. For Gaussian noise removal, we add white Gaussian noise with $\sigma = \hat{\gamma}$ to clean images. For Uniform noise removal, we generate noise from $\mathcal{U}(-\sqrt{3}\hat{\gamma}, \sqrt{3}\hat{\gamma})$. For denoising adversarial noisy images, the norm budgets of adversarial perturbation are set to be $\epsilon = 5/255 \cdot \sqrt{m}$ and $7/255 \cdot \sqrt{m}$ respectively, where m equals the size of test images. We perturb noisy observations whose noise are generated from $\mathcal{N}(0, \hat{\gamma} - \epsilon/\sqrt{m})$, so that the ℓ_2 -norms of total noise in adversarial images are still bounded by $\hat{\gamma} \cdot \sqrt{m}$ and the energy-density thus are bounded by $\hat{\gamma}^2$. We use $\text{Atk-}\epsilon/\sqrt{m}$ to denote the adversarially perturbed noisy images in the size of m with adversarial budget ϵ . The number of iterations of PGD in ObsAtk is set to be five.

From Tables 2.1, we observe that ObsAtk clearly degrades the reconstruction performance of DIDs. In comparison to Gaussian or Uniform noisy images with the

Table 2.1 The average PSNR (in dB) results of DnCNN denoisers on the gray-scale and RGB datasets. Four types of noise are used for evaluation, viz. Gaussian \mathcal{N} and Uniform \mathcal{U} random noise, and ObsAtk with two different adversarial budgets. The energy-density of noise is bounded by $\hat{\gamma}^2$.

Dataset	$\hat{\gamma}$	\mathcal{N}	\mathcal{U}	Atk- $5/255$	Atk- $7/255$
Set68	$25/255$	29.16/0.02	29.15/0.01	24.26/0.12	23.12/0.10
	$15/255$	31.68/0.00	31.68/0/00	26.66/0.04	26.08/0.02
Set12	$25/255$	30.39/0.01	30.41/0.01	24.32/0.18	22.96/0.13
	$15/255$	32.78/0.00	32.81/0.00	26.91/0.05	26.25/0.01
BSD68	$25/255$	31.25/0.11	31.17/0.11	27.44/0.08	26.08/0.06
	$15/255$	33.98/0.11	33.93/0.12	29.31/0.08	27.84/0.04
Kodak24	$25/255$	32.20/0.13	32.13/0.14	27.87/0.08	26.37/0.07
	$15/255$	34.77/0.13	34.73/0.14	29.55/0.07	28.00/0.04

same noise levels, the recovered results from adversarial images are much worse in the sense of the PSNR. For example, when removing $\hat{\gamma} = 15/255$ noisy images in Set12, the average PSNR of reconstructions from Gaussian noise can achieve 32.78 dB, whereas the PSNR drops to 26.25 dB when dealing with Atk- $7/255$ adversarial images. We observe the consistent phenomenon that a normally-trained denoiser $f_{\theta}^{\gamma}(\cdot)$ cannot effectively remove adversarial noise from visual results in Figure 2.2.

2.4 Robust and Generalizable Denoising via HAT

The previous section shows that existing deep denoisers are vulnerable to adversarial perturbations. To improve the adversarial robustness of deep denoisers, we propose an adversarial training method, hybrid adversarial training (HAT), that uses original noisy images and their adversarial versions for training. Furthermore, we build a connection between the adversarial robustness of deep denoisers and their generalization capability to unseen types of noise. We show that HAT-trained denoisers can effectively remove real-world noise without the need to leverage the real-world noisy data.

2.4.1 Hybrid Adversarial Training

AT has been proved to be a successful and universally applicable technique for robustifying deep neural networks. Most variants of AT are developed for the classification task specifically, such as TRADES [Zhang et al., 2019b] and GAIRAT [Zhang et al., 2021]. Here, we propose an AT strategy, HAT, for robust image denoising:

$$\begin{aligned} \min_{\theta \in \Theta} \mathbb{E}_{\mathbf{x} \sim P} \mathbb{E}_{Q \sim \mathcal{U}(\mathbb{Q}^r)} \mathbb{E}_{\mathbf{v} \sim Q} \frac{1}{2} \left(\frac{1}{1 + \alpha} \|f_{\theta}^{\gamma}(\mathbf{y}) - \mathbf{x}\|_2^2 \right. \\ \left. + \frac{\alpha}{1 + \alpha} \|f_{\theta}^{\gamma}(\mathbf{y}) - f_{\theta}^{\gamma}(\mathbf{y}')\|_2^2 \right), \end{aligned} \quad (2.3)$$

where $\mathbf{y} = \mathbf{x} + \mathbf{v}$ and $\mathbf{y}' = \mathbf{y} + \boldsymbol{\delta}^*$. Note that $\boldsymbol{\delta}^*$ is the adversarial perturbation obtained by solving ObsAtk in Eq. equation 2.1.

As shown in Eq. equation 2.3, the loss function consists of two terms. The first term measures the distance between ground-truth images \mathbf{x} and reconstructions $f_{\theta}^{\gamma}(\mathbf{y})$ from non-adversarial noisy images \mathbf{y} , where \mathbf{y} contains noise \mathbf{v} sampled from a certain common distribution Q , such as Gaussian. This term encourages a good reconstruction performance of f_{θ}^{γ} from common distributions. The second term is the distance between $f_{\theta}^{\gamma}(\mathbf{y})$ and the reconstruction $f_{\theta}^{\gamma}(\mathbf{y}')$ from the adversarially perturbed version \mathbf{y}' of \mathbf{y} . This term ensures that the reconstructions from any two noisy observations within a small neighborhood of \mathbf{y} have similar image qualities. Minimizing these two terms at the same time controls the worst-case reconstruction performance $\|f_{\theta}^{\gamma}(\mathbf{y}') - \mathbf{x}\|$.

The coefficient α balances the trade-off between reconstruction from common noise and the local continuity of f_{θ}^{γ} . When α equals zero, HAT degenerates to normal training on common noise. The obtained denoisers fail to resist adversarial perturbations as shown in Section 2.3. When α is very large, the optimization gradually ignores the first term and completely aims for local smoothness. This

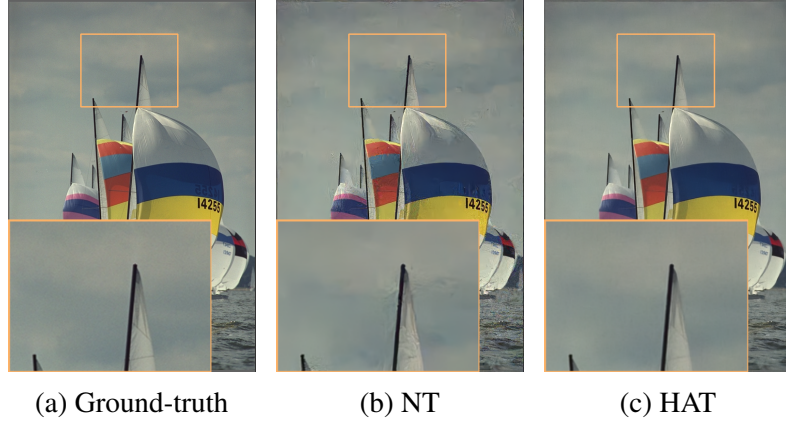


Fig. 2.3 From left to right are the ground-truth, the reconstruction of a normally-trained denoiser against attack, and the reconstruction of a HAT-trained denoiser against attack.

may yield a trivial solution that f_{θ}^{γ} always outputs a constant vector for any input. A proper value of α thus ensures a denoiser that performs well for common noise and the worst-case adversarial perturbations simultaneously. We perform an ablation study on the effect of α for the robustness enhancement and unseen noise removal in Appendix 2.6.3.

To train a denoiser applicable to different levels of noise with an energy-density bounded by γ^2 , we randomly select a noise distribution \mathcal{Q} from a family of common distributions \mathbb{Q}^{γ} . \mathbb{Q}^{γ} includes a variety of zero-mean distributions whose variance are bounded by γ^2 . For example, we define $\mathbb{Q}_{\mathcal{N}}^{\gamma} = \{\mathcal{N}(\mathbf{0}, \sigma^2 \mathbf{I}) | \sigma \sim \mathcal{U}(0, \gamma)\}$ for the experiments in the remaining of this paper.

2.4.2 Robustness Enhancement via HAT

We follow the same settings as those in Section 2.3 for training and evaluating γ -deep denoisers. The highest level of noise used for training is set to be $\gamma = 25/255$. Noise is sampled from a set of Gaussian distributions $\mathbb{Q}_{\mathcal{N}}^{\gamma}$. We train deep denoisers with the HAT strategy and set α to be 1, and use one-step $\text{Atk-}^{5/255}$ to generate adversarially noisy images for training. We compare HAT with normal training

(NT) and the vanilla adversarial training (vAT) used in Choi *et al.* Choi et al. [2021] that trains denoisers only with adversarial data. The results on Set68 and BSD68 are provided in this section. More results on Set12 and Kodak24 (in Tables 2.5 and 2.6) are provided in Appendix 2.6.2.

Table 2.2 The average PSNR (in dB) results of DnCNN-B denoisers on the gray-scale Set68 dataset. NT and HAT are compared in terms of the noise removal of Gaussian noise and adversarial noise. We repeat the training for three times and report the mean and standard deviation (mean/std).

Method	$\hat{\gamma}$	\mathcal{N}	Atk-3/255	Atk-5/255	Atk-7/255
NT	25/255	29.16 /0.02	26.20/0.07	24.26/0.12	23.12/0.10
	15/255	31.68 /0.00	27.98/0.05	26.66/0.04	26.08/0.02
vAT	25/255	29.05/0.07	27.02/0.15	25.51/0.32	24.34/0.34
	15/255	31.53/0.09	28.74/0.16	27.43/0.19	26.68/0.15
HAT	25/255	28.88/0.04	27.48 /0.10	26.40 /0.16	25.32 /0.17
	15/255	31.36/0.03	29.52 /0.01	28.34 /0.03	27.34 /0.03

From Tables 2.2 and 2.3, we observe that HAT obviously improves the reconstruction performance from adversarial noise in comparison to normal training. For example, on the Set68 dataset (Table 2.2), when dealing with 15/255-level noise, the normally-trained denoiser achieves 31.68 dB for Gaussian noise removal, but the PSNR drops to 26.08 dB against Atk-7/255. In contrast, the HAT-trained denoiser achieves a PSNR of 27.34 dB (1.26 dB higher) against Atk-7/255 and maintains a PSNR of 31.36 dB for Gaussian noise removal. In Figure 2.3, we can see that when dealing with adversarially noisy images, the HAT-trained denoiser can recover high-quality images while the normally-trained denoiser preserves noise patterns in the output. Besides, we observe that, similar to image classification tasks [Zhang et al., 2019b], AT-based methods (HAT and vAT) robustify deep denoisers at the expense of the performance on non-adversarial data (Gaussian denoising). Nevertheless, the degraded reconstructions are still reasonably good in terms of the PSNR.

Table 2.3 The average PSNR (in dB) results of DnCNN-C denoisers on the RGB BSD68 dataset.

Method	$\hat{\gamma}$	\mathcal{N}	Atk- $\frac{3}{255}$	Atk- $\frac{5}{255}$	Atk- $\frac{7}{255}$
NT	$\frac{25}{255}$	31.25 /0.11	28.93/0.08	27.44/0.08	26.08/0.06
	$\frac{15}{255}$	33.98 /0.11	31.09/0.10	29.31/0.08	27.84/0.04
vAT	$\frac{25}{255}$	30.64/0.02	28.81/0.03	27.67/0.01	26.64/0.03
	$\frac{15}{255}$	33.45/0.06	31.10/0.05	29.79/0.02	28.63/0.08
HAT	$\frac{25}{255}$	30.98/0.03	29.18 /0.03	28.02 /0.02	26.93 /0.04
	$\frac{15}{255}$	33.67/0.04	31.38 /0.04	30.03 /0.02	28.80 /0.01

Table 2.4 Comparison of different methods for denoising real-world noisy images in terms of PSNR (dB). We repeat the experiments of each denoising method for three times and report the mean/standard deviation of PSNR values.

Dataset	BM3D	DIP	N2S(1)	NT	vAT	HAT	N2C
PolyU	37.40/0.00	36.08/0.01	35.37/0.15	35.86/0.01	36.77/0.00	37.82 /0.04	– / –
CC	35.19/0.00	34.64/0.06	34.33/0.14	33.56/0.01	34.49/0.10	36.26 /0.06	– / –
SIDD	25.65/0.00	26.89/0.02	26.51/0.03	27.20/0.70	27.08/0.28	33.44 /0.02	<u>33.50</u> /0.03

2.4.3 Robustness Benefits Generalization to Unseen Noise

It has been shown that denoisers that are normally trained on common synthetic noise fail to remove real-world noise induced by standard imaging procedures [Xu et al., 2017, Abdelhamed et al., 2018]. To train denoisers that can handle real-world noise, researchers have proposed several methods which can be roughly divided into two categories, namely *dataset-based* denoising methods and *single-image-based* denoising methods. High-performance dataset-based methods require a set of real noisy data for training, e.g., CBDNet requiring pairs of clean and noisy images [Guo et al., 2019b] and Noise2Noise requiring multiple noisy observations of every single image [Lehtinen et al., 2018]. However, a large number of paired data are not available in some applications, such as medical radiology and high-speed photography. To address this, single-image-based methods are proposed to remove noise by exploiting the correlation between signals across pixels and the independence between noise. This category of methods, such as DIP [Ulyanov et al., 2018] and N2S [Batson and Royer, 2019], are adapted to various types of

signal-independent noise, but they optimize the deep denoiser on each test image. The test-time optimization is extremely time-consuming, e.g., N2S needs to update a denoiser for *thousands of iterations* to achieve good reconstruction performance.

Here, we point out that HAT is a promising framework to train a generalizable deep denoiser *only with synthetic noise*. The resultant denoiser can be directly applied to perform denoising for unseen noisy images in real-time. During training, HAT first samples noise from common distributions (Gaussian) with noise levels from low to high. ObsAtk then explores the ε -neighborhood for each noisy image to search for a particular type of noise that degrades the denoiser the most. By ensuring the denoising performance of the worst-case noise, the resultant denoiser can deal with other unknown types of noise within the ε -neighborhood as well. To train a robust denoiser that generalizes well to real-world noise, we need to choose a proper adversarial budget ε . When ε is very small and close to zero, the HAT reduces to normal training. When ε is very much larger than the norm of basic noise \mathbf{v} , the adversarially noisy image may be visually unnatural because the adversarial perturbation $\boldsymbol{\delta}$ only satisfies the zero-mean constraint and is not guaranteed to be spatially uniformly distributed as other types of natural noise being. In practice, we set the value of ε of ObsAtk to be $5/255 \cdot \sqrt{m}$, where m denotes the size of image patches. The value of α of HAT is kept unchanged as 2.

Experimental Settings We evaluate the generalization capability of HAT on several real-world noisy datasets, including PolyU [Xu et al., 2018], CC [Xu et al., 2017], and SIDD [Abdelhamed et al., 2018]. PolyU, CC, and SIDD contain RGB images of common scenes in daily life. These images are captured by different brands of digital cameras and smartphones, and they contain various levels of noise by adjusting the ISO values. For the PolyU and CC, we use the clean images in BSD500 for training an adversarially robust γ -denoiser with $\gamma = 25/255$. We sample Gaussian noise from a set of distributions $\mathbb{Q}_{\mathcal{N}}^{\gamma}$ and add the noise to clean images

to craft noisy observations. HAT trains the denoiser jointly with Gaussian noisy images and their adversarial versions. For the SIDD, we use clean images in the SIDD-small set for training and test the denoisers on the SIDD-val set. The highest level of noise used for HAT is set to be $\gamma = 50/255$. In each case, we only use clean images for training denoisers without the need of real noisy images

Results We compare HAT-trained denoisers with the NT and vAT-trained ones. From Table 2.4, we observe that HAT performs much better than both competitors. For example, on the SIDD-val dataset, the HAT-trained denoiser achieves an average PSNR value of 33.44 dB that is 6.24 dB higher than the NT-trained one. We also compare HAT-trained denoisers with single-image-based methods, including DIP, N2S, and the classical BM3D [Dabov et al., 2007]. For DIP and N2S,¹ the numbers of iterations for each image are set to be 2,000 and 1,000, respectively. N2S works in two modes, namely single-image-based denoising and dataset-based denoising. Here, we use N2S in the single-image-based mode, denoted as N2S(1), due to the assumption that no real noisy data are available for training. We observe that HAT-trained denoisers consistently outperform these baselines. Visual comparisons are provided in Appendix 2.6.4. Besides, since the SIDD-small provides a set of real noisy and ground-truth pairs, we train a denoiser, denoted as Noise2Clean (N2C), with these paired data and use the N2C denoiser as the oracle for comparison. We observe that HAT-trained denoisers are comparable to the N2C one for denoising images in SIDD-val (a PSNR of 33.44dB vs 33.50dB).

2.5 Chapter Summary

Normally-trained deep denoisers are vulnerable to adversarial attacks. HAT can effectively robustify deep denoisers and boost their generalization capability to

¹The officially released codes of DIP and N2S are used here.

unseen real-world noise. In the future, we will extend the adversarial-training framework to other image restoration tasks, such as deblurring. We aim to develop a generic AT-based robust optimization framework to train deep models that can recover clean images from unseen types of degradation.

2.6 Appendices

2.6.1 Two-step Projection

Theorem 2.6.1 *For any arbitrary vector $\boldsymbol{\delta} \in \mathbb{R}^m$, its projection onto the region defined by the intersection of the norm-bounded and zero-mean constraints is equivalent to the projection first onto the zero-mean hyperplane followed by the projection onto the ε -ball ($\varepsilon > 0$), i.e.,*

$$Proj_{A \cap B}(\boldsymbol{\delta}) = Proj_B(Proj_A(\boldsymbol{\delta})), \quad (2.4)$$

where

$$A = \{\mathbf{z} \in \mathbb{R}^m \mid \mathbf{n}^\top \mathbf{z} = 0\}, \quad (2.5a)$$

$$B = \{\mathbf{z} \in \mathbb{R}^m \mid \|\mathbf{z}\|_2^2 \leq \varepsilon^2\}, \quad (2.5b)$$

and $\mathbf{n} = [1, 1, \dots, 1]^\top$.

Proof Let us consider the RHS of Eq. equation 2.4 first. It is easy to derive the projections onto A and B separately:

$$Proj_A(\boldsymbol{\delta}) = \boldsymbol{\delta} - \frac{\mathbf{n}^\top \boldsymbol{\delta}}{\|\mathbf{n}\|_2^2} \mathbf{n}, \quad (2.6a)$$

$$Proj_B(\boldsymbol{\delta}) = \min\left(\frac{\varepsilon}{\|\boldsymbol{\delta}\|_2}, 1\right) \boldsymbol{\delta}. \quad (2.6b)$$

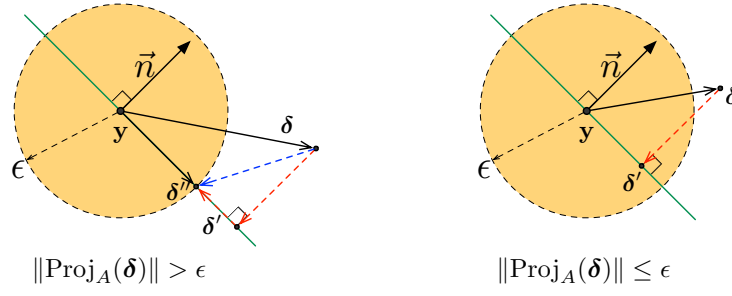


Fig. 2.4 Illustration of Theorem 2.6.1. In the case of $\|\text{Proj}_A(\boldsymbol{\delta})\| > \epsilon$, the red-dot lines show that the perturbation $\boldsymbol{\delta}$ is projected onto the region defined by the zero-mean and ϵ -ball constraints sequentially. The blue-dot line shows the exact projection of $\boldsymbol{\delta}$ on to $A \cap B$.

Thus, we have

$$\text{Proj}_B(\text{Proj}_A(\boldsymbol{\delta})) = \begin{cases} \text{Proj}_A(\boldsymbol{\delta}), & \text{if } \|\text{Proj}_A(\boldsymbol{\delta})\| \leq \epsilon; \\ \frac{\epsilon}{\|\text{Proj}_A(\boldsymbol{\delta})\|_2} \text{Proj}_A(\boldsymbol{\delta}), & \text{if } \|\text{Proj}_A(\boldsymbol{\delta})\| > \epsilon. \end{cases} \quad (2.7)$$

Now let us consider the LHS of Eq. equation 2.4. The projection onto $A \cap B$ can be formulated as the solution of the following convex optimization problem:

$$\min_{\mathbf{z}} \frac{1}{2} \|\boldsymbol{\delta} - \mathbf{z}\|_2^2, \quad \text{s.t.} \quad \mathbf{n}^\top \mathbf{z} = 0, \quad \|\mathbf{z}\|_2^2 \leq \epsilon^2, \quad (2.8)$$

where $\mathbf{z} \in \mathbb{R}^m$. We can write the Lagrangian, $L : \mathbb{R}^m \times \mathbb{R} \times \mathbb{R} \rightarrow \mathbb{R}$, associated with the problem equation 2.8 as

$$L(\mathbf{z}, \lambda, \nu) = \frac{1}{2} \|\boldsymbol{\delta} - \mathbf{z}\|_2^2 + \lambda (\|\mathbf{z}^*\|_2^2 - \epsilon^2) + \nu \mathbf{n}^\top \mathbf{z}. \quad (2.9)$$

Since there exists an $\mathbf{z} \in \mathbb{R}^m$, e.g., $\mathbf{z} = [0, \dots, 0]^\top \in \mathbb{R}^m$, such that $\mathbf{n}^\top \mathbf{z} = 0$ and $\|\mathbf{z}\|_2^2 < \epsilon^2$, the problem equation 2.8 is strictly feasible, i.e., it satisfies the Slater's condition Boyd et al. [2004]. Besides, the objective and the constraints are all differentiable, thus the KKT conditions in Eq. equation 2.10 provide necessary and

sufficient conditions for optimality.

$$\|\mathbf{z}^*\|_2^2 - \varepsilon^2 \leq 0, \quad (2.10a)$$

$$\mathbf{n}^\top \mathbf{z}^* = 0, \quad (2.10b)$$

$$\lambda \geq 0, \quad (2.10c)$$

$$\lambda (\|\mathbf{z}^*\|_2^2 - \varepsilon^2) = 0, \quad (2.10d)$$

$$\frac{\partial L}{\partial \mathbf{z}} = (1 + 2\lambda)\mathbf{z}^* - \boldsymbol{\delta} + \mathbf{v}\mathbf{n} = 0. \quad (2.10e)$$

We obtain the optimal solution by considering the following two cases separately, i.e., $\|\text{Proj}_A(\boldsymbol{\delta})\| \leq \varepsilon$ and $\|\text{Proj}_A(\boldsymbol{\delta})\| > \varepsilon$.

Case-(1): $\|\text{Proj}_A(\boldsymbol{\delta})\| > \varepsilon$.

If $\lambda > 0$, then Eq. equation 2.10 reduces to the following equation:

$$\mathbf{n}^\top \mathbf{z}^* = 0, \quad (2.11a)$$

$$\|\mathbf{z}^*\|_2^2 - \varepsilon^2 = 0, \quad (2.11b)$$

$$(1 + 2\lambda)\mathbf{z}^* - \boldsymbol{\delta} + \mathbf{v}\mathbf{n} = 0. \quad (2.11c)$$

We can easily solve these equations and obtain that

$$(1 + 2\lambda) = \|\text{Proj}_A(\boldsymbol{\delta})\| / \varepsilon, \quad (2.12a)$$

$$\mathbf{v} = \mathbf{n}^\top \boldsymbol{\delta} / m, \quad (2.12b)$$

$$\mathbf{z}^* = \frac{\varepsilon}{\|\text{Proj}_A(\boldsymbol{\delta})\|_2} \text{Proj}_A(\boldsymbol{\delta}). \quad (2.12c)$$

If $\lambda = 0$, then Eq. equation 2.10 reduces to the following set of equations:

$$\|\mathbf{z}^*\|_2^2 - \varepsilon^2 \leq 0, \quad (2.13a)$$

$$\mathbf{n}^\top \mathbf{z}^* = 0 \quad (2.13b)$$

$$\mathbf{z}^* - \boldsymbol{\delta} + \nu \mathbf{n} = 0. \quad (2.13c)$$

According to equation 2.13b and equation 2.13c, we obtain that $\mathbf{z}^* = \boldsymbol{\delta} - \frac{\mathbf{n}^\top \boldsymbol{\delta}}{m} \mathbf{n} = \text{Proj}_A(\boldsymbol{\delta})$ with a norm strictly larger than ε , which contradicts the constraint $\|\mathbf{z}^*\|_2^2 \leq \varepsilon^2$. Thus, for the case of $\|\text{Proj}_A(\boldsymbol{\delta})\| > \varepsilon$, we have that $\mathbf{z}^* = \frac{\varepsilon}{\|\text{Proj}_A(\boldsymbol{\delta})\|_2} \text{Proj}_A(\boldsymbol{\delta})$ which is equal to $\text{Proj}_B(\text{Proj}_A(\boldsymbol{\delta}))$ in Eq. equation 2.7.

Case-(2): $\|\text{Proj}_A(\boldsymbol{\delta})\| \leq \varepsilon$.

Since $\|\text{Proj}_A(\boldsymbol{\delta})\| \leq \varepsilon$ and $\|\text{Proj}_A(\boldsymbol{\delta})\| \in A$, we have $\text{Proj}_A(\boldsymbol{\delta}) \in A \cap B$. For any other point $\mathbf{z}' \in A \cap B$ and $\mathbf{z}' \neq \text{Proj}_A(\boldsymbol{\delta})$, we have $\|\boldsymbol{\delta} - \mathbf{z}'\| > \|\boldsymbol{\delta} - \text{Proj}_A(\boldsymbol{\delta})\|$, where the strict inequality holds because A is the set of points from a hyperplane. Thus, \mathbf{z}' is not the $\text{Proj}_{A \cap B}(\boldsymbol{\delta})$. Therefore, $\text{Proj}_{A \cap B}(\boldsymbol{\delta}) = \text{Proj}_A(\boldsymbol{\delta}) = \text{Proj}_B(\text{Proj}_A(\boldsymbol{\delta}))$.

In summary, we show that $\text{Proj}_{A \cap B}(\boldsymbol{\delta}) = \text{Proj}_B(\text{Proj}_A(\boldsymbol{\delta}))$ for any arbitrary $\boldsymbol{\delta} \in \mathbb{R}^m$.

2.6.2 Experiments of Robustness Enhancement on Set12 and Kodak24

We compare the robustness of deep denoisers trained via three strategies, i.e., NT, vAT and HAT. The results on Set 12 and Kodak24 are provided in Table 2.5 and Table 2.6 respectively. We observe that HAT can effectively robustify deep denoisers. The reconstruction quality of HAT-trained denoisers from adversarially noisy images is clearly better than that of the NT and vAT-trained ones.

Table 2.5 The average PSNR (in dB) results of DnCNN-B denoisers on the gray-scale Set12 dataset.

Training	$\hat{\gamma}$	\mathcal{N}	Atk-3/255	Atk-5/255	Atk-7/255
NT	25/255	30.39 /0.01	26.51/0.14	24.32/0.18	22.96/0.13
	15/255	32.78 /0.00	28.50/0.08	26.91/0.05	26.25/0.01
vAT	25/255	30.25/0.08	27.56/0.06	25.82/0.04	24.33/0.04
	15/255	32.63/0.09	29.37/0.17	27.83/0.15	26.91/0.08
HAT	25/255	30.01/0.06	27.96 /0.15	26.46 /0.20	25.13 /0.19
	15/255	32.47/0.04	29.95 /0.03	28.45 /0.04	27.20 /0.03

Table 2.6 The average PSNR (in dB) results of DnCNN-C denoisers on the RGB Kodak24 dataset.

Training	$\hat{\gamma}$	\mathcal{N}	Atk-3/255	Atk-5/255	Atk-7/255
NT	25/255	32.20 /0.13	29.57/0.09	27.87/0.08	26.37/0.07
	15/255	34.77 /0.13	31.54/0.11	29.55/0.07	28.00/0.04
vAT	25/255	31.44/0.01	29.41/0.05	28.13/0.06	26.98/0.02
	15/255	34.14/0.08	31.53/0.11	30.06/0.08	28.78/0.06
HAT	25/255	31.83/0.04	29.85 /0.02	28.56 /0.02	27.34 /0.05
	15/255	34.36/0.06	31.84 /0.05	30.37 /0.02	29.05 /0.01

2.6.3 Ablation study

Effect of α on Robustness Enhancement and Generalization to Real-world noise

Here, we evaluate the effect of α in HAT on the adversarial robustness and the generalization capability to real-world noise. We train deep denoisers on the RGB BSD500 (except 68 images for test) dataset. The obtained denoisers are tested on the BSD68 dataset for Gaussian and adversarial noise removal. The generalization capability is evaluated on two datasets of real-world noisy images, i.e., PolyU and CC. Experimental settings follow those in Section 2.4.2.

Figure 2.5 corroborates the analysis in Section 2.4.1 that the coefficient α balances the trade-off between reconstruction from common noise and the adversarial robustness. We also find that the generalization capability to real-world noise is correlated to the adversarial robustness. Specifically, good adversarial robustness

usually implies good generalization to real-world noise. In Figure 2.5, the best robustness and the best performance on real-world noise appear around $\alpha = 1$ or 2. When α is too large or too small, the robustness and generalization worsen. For the noise sampled from Gaussian distributions, increasing α degrades the denoising performance. In summary, we set α to 1 or 2 to achieve a good balance between the denoising performance on common noise and the adversarial robustness as well as real-world generalization.

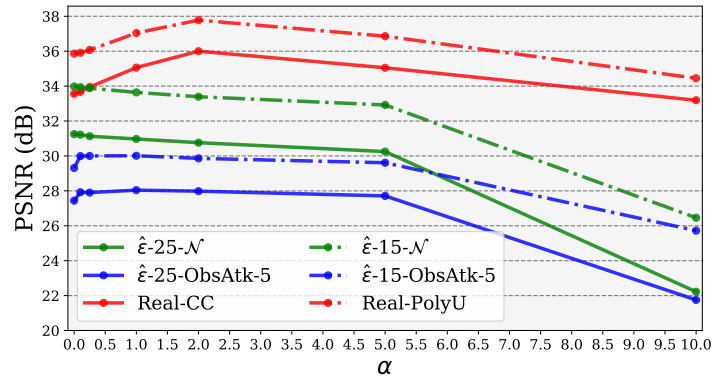


Fig. 2.5 Ablation study on the effect of α in HAT. **Green lines** show the denoising results on non-adversarial noise sampled from common distributions. The legend $\hat{\gamma}\text{-w-}\mathcal{N}$ denotes the Gaussian noise ($\sigma = w/255$) with a energy-density bounded by $\hat{\gamma}^2 = w^2/255^2$. **Blue lines** show that denoising results on adversarially perturbed noisy images. $\hat{\gamma}\text{-w-ObsAtk-5}$ denotes the adversarial noise crafted by ObsAtk-5 with a energy-density bounded by $\hat{\gamma}^2$. **Red lines** show the denoising results on real-world noisy images.

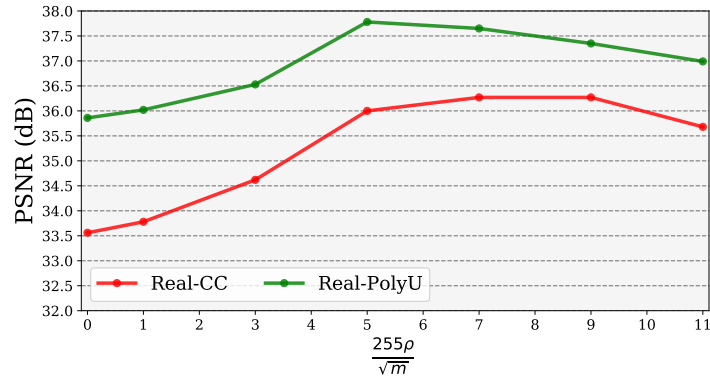


Fig. 2.6 Ablation study on the effect of ϵ in HAT.

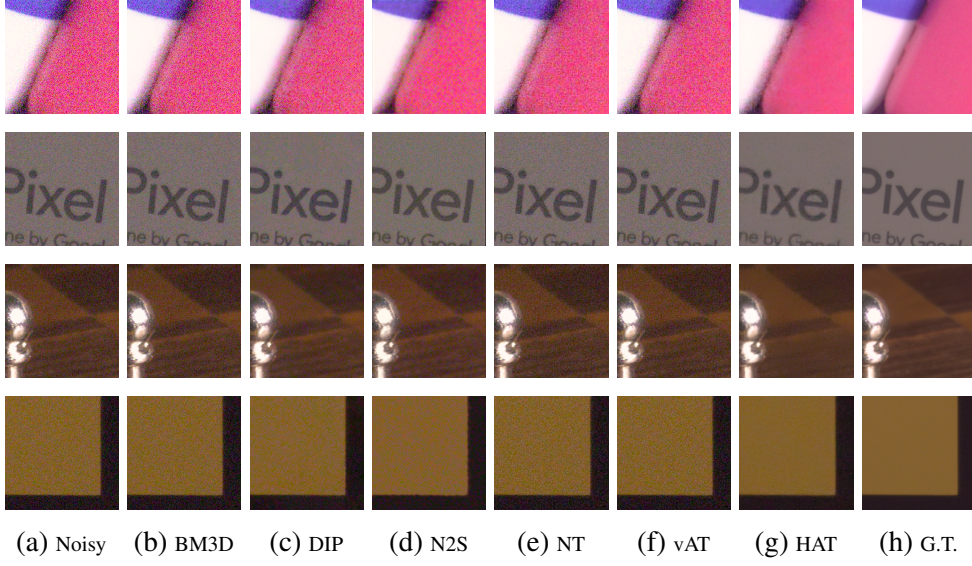


Fig. 2.7 Comparison of different denoisers for denoising SIDD-val set. From left to right are the input noisy images, reconstructions of different denoisers, and the ground-truth (G.T.) images. We can see that the HAT-trained denoiser performs the best in comparison to other baseline methods.

Effect of ε on Generalization to Real-world Noise

Here, we evaluate the effect of ε used in HAT on the generalization capability to real-world noise. We train deep denoisers on the RGB BSD500 (except 68 images for test) dataset and evaluate the generalization capability on two real-world datasets, namely PolyU and CC. The α is set to be 2. The adversarial budget ε of ObsAtk- ε/\sqrt{m} , that generates adversarially noisy images for HAT, is set to be values from $[0, \sqrt{m}, 3\sqrt{m}, \dots, 11\sqrt{m}]$ for comparison, where m denotes the size of images. Other experimental settings follow those in Section 2.4.2.

Figure 2.6 corroborates the analysis in Section 2.4.3. When ε is very small and close to zero, the HAT reduces to normal training. The resultant denoisers cannot effectively remove real-world noise. When ε is very much larger than the norm of basic noise \mathbf{v} , the statistics of adversarial noise may be very unnatural because the adversarial perturbation $\boldsymbol{\delta}$ might concentrate on a certain region, like edges or texture, and not be spatially uniformly distributed as other types of natural

noise being. We can see that, when $\varepsilon > 7/255\sqrt{m}$, the denoising performance on real-world datasets starts to decrease. In practice, we set the value of ε of ObsAtk to be $5/255 \cdot \sqrt{m}$ to train generalizable denoisers.

2.6.4 Visual results of real-world noise removal

We show the denoising results on SIDD-val set in Figure 2.7. We observe that HAT-trained denoiser can effectively remove the real-world noise while the normally-trained one retains much noise in the reconstructions. Besides, the HAT-trained denoiser outperforms other baseline methods and produces much cleaner results.

Chapter 3

On Robustness of Neural Ordinary Differential Equations

Neural ordinary differential equations (ODEs) have been attracting increasing attention in various research domains recently. There have been some works studying optimization issues and approximation capabilities of neural ODEs, but their robustness is still yet unclear. In this work, we fill this important gap by exploring robustness properties of neural ODEs both empirically and theoretically. We first present an empirical study on the robustness of the neural ODE-based networks (ODEnets) by exposing them to inputs with various types of perturbations and subsequently investigating the changes of the corresponding outputs. In contrast to conventional convolutional neural networks (CNNs), we find that the ODEnets are more robust against both random Gaussian perturbations and adversarial attack examples. We then provide an insightful understanding of this phenomenon by exploiting a certain desirable property of the flow of a continuous-time ODE, namely that integral curves are non-intersecting. Our work suggests that, due to their intrinsic robustness, it is promising to use neural ODEs as a basic block for building robust deep network models. To further enhance the robustness of

vanilla neural ODEs, we propose the time-invariant steady neural ODE (TisODE), which regularizes the flow on perturbed data via the time-invariant property and the imposition of a steady-state constraint. We show that the TisODE method outperforms vanilla neural ODEs and also can work in conjunction with other state-of-the-art architectural methods to build more robust deep networks.

3.1 Introduction

Neural ordinary differential equations [Chen et al., 2018] form a family of models that approximate nonlinear mappings by using continuous-time ODEs. Due to their desirable properties, such as invertibility and parameter efficiency, neural ODEs have attracted increasing attention recently [Dupont et al., 2019, Liu et al., 2019]. For example, Grathwohl et al. [2018] proposed a neural ODE-based generative model—the FFJORD—to solve inverse problems; Quaglino et al. [2019] used a higher-order approximation of the states in a neural ODE, and proposed the SNet to accelerate computation. Along with the wider deployment of neural ODEs, robustness issues come to the fore. However, the robustness of neural ODEs is still yet unclear. In particular, it is unclear how robust neural ODEs are in comparison to the widely-used CNNs. Robustness properties of CNNs have been studied extensively. In this work, we present the first systematic study on exploring the robustness properties of neural ODEs.

To do so, we consider the task of image classification. We expect that results would be similar for other machine learning tasks such as regression. Neural ODEs are dimension-preserving mappings, but a classification model transforms a high-dimensional input—such as an image—into an output whose dimension is equal to the number of classes. Thus, we consider the neural ODE-based classification network (ODEnet) whose architecture is shown in Figure 3.1. An ODEnet consists

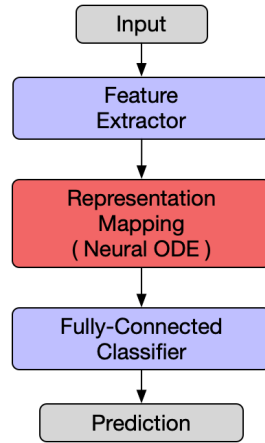


Fig. 3.1 The architecture of an ODEnet. The neural ODE block serves as a dimension-preserving nonlinear mapping.

of three components: the feature extractor (FE) consists of convolutional layers which maps an input datum to a multi-channel feature map, a neural ODE that serves as the nonlinear representation mapping (RM), and the fully-connected classifier (FCC) that generates a prediction vector based on the output of the RM.

The robustness of a classification model can be evaluated through the lens of its performance on perturbed images. To comprehensively investigate the robustness of neural ODEs, we perturb original images with commonly-used perturbations, namely, random Gaussian noise [Szegedy et al., 2013] and harmful adversarial examples [Goodfellow et al., 2015, Madry et al., 2018]. We conduct experiments in two common settings—training the model only on authentic non-perturbed images and training the model on authentic images as well as the Gaussian perturbed ones. We observe that ODEnets are more robust compared to CNN models against all types of perturbations in both settings. We then provide an insightful understanding of such intriguing robustness of neural ODEs by exploiting a certain property of the flow [Dupont et al., 2019], namely that integral curves that start at distinct initial states are non-intersecting. The flow of a continuous-time ODE is defined as the family of solutions/paths traversed by the state, starting from different initial points, and an integral curve is a specific solution for a given initial point. The

non-intersecting property indicates that an integral curve starting from some point is constrained by the integral curves starting from that point’s neighborhood. Thus, in an ODEnet, if a correctly classified datum is slightly perturbed, the integral curve associated to its perturbed version would not change too much from the original one. Consequently, the perturbed datum could still be correctly classified. Thus, there exists intrinsic robustness regularization in ODEnets, which is absent from CNNs.

Motivated by this property of the neural ODE flow, we attempt to explore a more robust neural ODE architecture by introducing stronger regularization on the flow. We thus propose a *Time-Invariant Steady neural ODE* (TisODE). The TisODE removes the time dependence of the dynamics in an ODE and imposes a steady-state constraint on the integral curves. Removing the time dependence of the derivative results in the time-invariant property of the ODE. To wit, given a solution $\mathbf{z}_1(t)$, another solution $\tilde{\mathbf{z}}_1(t)$, with an initial state $\tilde{\mathbf{z}}_1(0) = \mathbf{z}_1(T')$ for some $T' > 0$, can be regarded as the $-T'$ - shift version of $\mathbf{z}_1(t)$. Such a time-invariant property would make bounding the difference between output states convenient. To elaborate, let the output of a neural ODE correspond to states at time $T > 0$. By the time-invariant property, the difference between outputs, $\|\tilde{\mathbf{z}}_1(T) - \mathbf{z}_1(T)\|$, equals to $\|\mathbf{z}_1(T + T') - \mathbf{z}_1(T)\|$. To control this distance, a steady-state regularization term is introduced to the overall objective to constrain the change of a state after time exceeds T . With the time-invariant property and the steady-state term, we show that TisODE even is more robust. We do so by evaluating the robustness of TisODE-based classifiers against various types of perturbations and observe that such models are more robust than vanilla ODE-based models.

In addition, some other effective architectural solutions have also been recently proposed to improve the robustness of CNNs. For example, [Xie et al. \[2018\]](#) randomly resizes or pads zeros into test images to destroy the specific structure

of adversarial perturbations. Besides, the model proposed by Xie et al. [2019] contains feature denoising filters to remove the feature-level patterns of adversarial examples. We conduct experiments to show that our proposed TisODE can work seamlessly and in conjunction with these methods to further boost the robustness of deep models. Thus, the proposed TisODE can be used as a generally applicable and effective component for improving the robustness of deep models.

In summary, our contributions are as follows. Firstly, we are the first to provide a systematic empirical study on the robustness of neural ODEs and find that the neural ODE-based models are more robust compared to conventional CNN models. This finding inspires new applications of neural ODEs in improving robustness of deep models, a problem that concerns many deep learning theorists and practitioners alike. Secondly, we propose the TisODE method, which is simple yet effective in significantly boosting the robustness of neural ODEs. Moreover, the proposed TisODE can also be used in conjunction with other state-of-the-art robust architectures. Thus, TisODE can serve as a drop-in module to improve the robustness of deep models effectively.

3.2 Preliminaries on neural ODE

It has been shown that a residual block [He et al., 2016] can be interpreted as the discrete approximation of an ODE by setting the discretization step to be one. When the discretization step approaches zero, it yields a family of neural networks, which are called neural ODEs [Chen et al., 2018]. Formally, in a neural ODE, the relation between input and output is characterized by the following set of equations:

$$\frac{dz(t)}{dt} = f_{\theta}(z(t), t), \quad z(0) = z_{\text{in}}, \quad z_{\text{out}} = z(T), \quad (3.1)$$

where $f_\theta : \mathbb{R}^d \times [0, \infty) \rightarrow \mathbb{R}^d$ denotes the trainable layers that are parameterized by weights θ and $\mathbf{z} : [0, \infty) \rightarrow \mathbb{R}^d$ represents the d -dimensional state of the neural ODE. We assume that f_θ is continuous in t and globally Lipschitz continuous in \mathbf{z} . In this case, the input \mathbf{z}_{in} of the neural ODE corresponds to the state at $t = 0$, and the output \mathbf{z}_{out} is associated to the state at some $T \in (0, \infty)$. Because f_θ governs how the state changes with respect to time t , we also use f_θ to denote the *dynamics* of the neural ODE.

Given input \mathbf{z}_{in} , the output \mathbf{z}_{out} can be computed by solving the ODE in (3.1). If T is fixed, the output \mathbf{z}_{out} only depends on the input \mathbf{z}_{in} and the dynamics f_θ , which also corresponds to the weighted layers in the neural ODE. Therefore, the neural ODE can be represented as the d -dimensional function $\phi_T(\cdot, \cdot)$ of the input \mathbf{z}_{in} and the dynamics f_θ , i.e.,

$$\mathbf{z}_{\text{out}} = \mathbf{z}(T) = \mathbf{z}(0) + \int_0^T f_\theta(\mathbf{z}(t), t) dt = \phi_T(\mathbf{z}_{\text{in}}, f_\theta).$$

The terminal time T of the output state $\mathbf{z}(T)$ is set to be 1 in practice. Several methods have been proposed for training neural ODEs, such as the adjoint sensitivity method [Chen et al., 2018], SNet [Quaglino et al., 2019], and the auto-differentiation technique [Paszke et al., 2017]. In this work, we use the most straightforward technique, i.e., updating the weights θ with the auto-differentiation technique in the PyTorch framework.

3.3 An empirical study on the robustness of ODEnets

Robustness of deep models has gained increased attention, as it is imperative that deep models employed in critical applications, such as healthcare, are robust. The robustness of a model is measured by the sensitivity of the prediction with respect to small perturbations on the inputs. In this study, we consider three commonly-used

perturbation schemes, namely random Gaussian perturbations, FGSM [Goodfellow et al., 2015] adversarial examples, and PGD [Madry et al., 2018] adversarial examples. These perturbation schemes reflect noise and adversarial robustness properties of the investigated models respectively. We evaluate the robustness via the classification accuracies on perturbed images, in which the original non-perturbed versions of these images are all correctly classified.

For a fair comparison with conventional CNN models, we made sure that the number of parameters of an ODEnet is close to that of its counterpart CNN model. Specifically, the ODEnet shares the same network architecture with the CNN model for the FE and FCC parts. The only difference is that, for the RM part, the input of the ODE-based RM is concatenated with one more channel which represents the time t , while the RM in a CNN model has a skip connection and serves as a residual block. During the training phase, all the hyperparameters are kept the same, including training epochs, learning rate schedules, and weight decay coefficients. Each model is trained *three* times with different random seeds, and we report the average performance (classification accuracy) together with the standard deviation.

3.3.1 Experimental settings

Dataset: We conduct experiments to compare the robustness of ODEnets with CNN models on three datasets, i.e., the MNIST [LeCun et al., 1998], the SVHN [Netzer et al., 2011], and a subset of the ImageNet dataset [Deng et al., 2009]. We call the subset ImgNet10 since it is collected from 10 synsets of ImageNet: dog, bird, car, fish, monkey, turtle, lizard, bridge, cow, and crab. We selected 3,000 training images and 300 test images from each synset and resized all images to 128×128 .

Architectures: On the MNIST dataset, both the ODEnet and the CNN model consists of four convolutional layers and one fully-connected layer. The total

number of parameters of the two models is around 140k. On the SVHN dataset, the networks are similar to those for the MNIST; we only changed the input channels of the first convolutional layer to three. On the ImgNet10 dataset, there are nine convolutional layers and one fully-connected layer for both the ODEnet and the CNN model. The numbers of parameters is approximately 280k. In practice, the neural ODE can be solved with different numerical solvers such as the Euler method and the Runge-Kutta methods [Chen et al., 2018]. Here, we use the easily-implemented Euler method in the experiments. To balance the computation and the continuity of the flow, we solve the ODE initial value problem in equation (3.1) by the Euler method with step size 0.1. Our implementation builds on the open-source neural ODE codes.¹ Details on the network architectures are included in the Appendix.

Training: The experiments are conducted using two settings on each dataset—training models only with original non-perturbed images and training models on original images together with their perturbed versions. In both settings, we added a weight decay term into the training objective to regularize the norm of the weights, since this can help control the model’s representation capacity and improve the robustness of a neural network [Sokolić et al., 2017]. In the second setting, images perturbed with random Gaussian noise are used to fine-tune the models, because augmenting the dataset with small perturbations can possibly improve the robustness of models and synthesizing Gaussian noise does not incur excessive computation time.

¹<https://github.com/rtqichen/torchdiffeq>.

3.3.2 Robustness of ODEnets trained only on non-perturbed images

The first question we are interested in is how robust ODEnets are against perturbations if the model is only trained on original non-perturbed images. We train CNNs and ODEnets to perform classification on three datasets and set the weight decay parameters for all models to be 0.0005. We make sure that both the well-trained ODEnets and CNN models have satisfactory performances on original non-perturbed images, i.e., around 99.5% for MNIST, 95.0% for the SVHN, and 80.0% for ImgNet10. Here, to calculate the robust accuracy, we first identify and select the samples whose clean versions are correctly classified by the obtained classifiers. Then, we compute the classification accuracy of the adversarial examples on the set of the selected samples.

Since Gaussian noise is ubiquitous in modeling image degradation, we first evaluated the robustness of the models in the presence of zero-mean random Gaussian perturbations. It has also been shown that a deep model is vulnerable to harmful adversarial examples, such as the FGSM [Goodfellow et al., 2015]. We are also interested in how robust ODEnets are in the presence of adversarial examples. The standard deviation σ of Gaussian noise and the l_∞ -norm ϵ of the FGSM attack for each dataset are shown in Table 3.1.

From the results in Table 3.1, we observe that the ODEnets demonstrate superior robustness compared to CNNs for all types of perturbations. On the MNIST dataset, in the presence of Gaussian perturbations with a large σ of $100/255$, the ODEnet produces much higher accuracy on perturbed images compared to the CNN model (73.2% vs. 56.4%). For the FGSM-0.3 adversarial examples, the accuracy of ODEnet is around twice as high as that of the CNN model. On the SVHN dataset, ODEnets significantly outperform CNN models, e.g., for the FGSM-5/255 examples, the accuracy of the ODEnet is 43.0%, which is much higher than that

Table 3.1 Robustness comparison of different models. We report their mean classification accuracies (%) and standard deviations (mean / std) on perturbed images from the MNIST, the SVHN, and the ImgNet10 datasets. Two types of perturbations are used—zero-mean Gaussian noise and FGSM adversarial attack. The results show that ODEnets are much more robust in comparison to CNN models.

	Gaussian noise			Adversarial attack		
MNIST	$\sigma = 50/255$	$\sigma = 75/255$	$\sigma = 100/255$	FGSM-0.15	FGSM-0.3	FGSM-0.5
CNN	98.1/0.7	85.8/4.3	56.4/5.6	63.4/2.3	24.0/8.9	8.3/3.2
ODEnet	98.7 /0.6	90.6 /5.4	73.2 /8.6	83.5 /0.9	42.1 /2.4	14.3 /2.1
SVHN	$\sigma = 15/255$	$\sigma = 25/255$	$\sigma = 35/255$	FGSM-3/255	FGSM-5/255	FGSM-8/255
CNN	90.0/1.2	76.3/2.7	60.9/3.9	29.2/2.9	13.7/1.9	5.4/1.5
ODEnet	95.7 /0.7	88.1 /1.5	78.2 /2.1	58.2 /2.3	43.0 /1.3	30.9 /1.4
ImgNet10	$\sigma = 10/255$	$\sigma = 15/255$	$\sigma = 25/255$	FGSM-5/255	FGSM-8/255	FGSM-16/255
CNN	80.1/1.8	63.3/2.0	40.8/2.7	28.5/0.5	18.1/0.7	9.4/1.2
ODEnet	81.9 /2.0	67.5 /2.0	48.7 /2.6	36.2 /1.0	27.2 /1.1	14.4 /1.7

of the CNN model (13.7%). On the ImgNet10, for both cases of $\sigma = 25/255$ and FGSM-8/255, ODEnet outperforms CNNs by a large margin of around 9%.

3.3.3 Robustness of ODEnets trained on original images together with Gaussian perturbations

Training a model on original images together with their perturbed versions can improve the robustness of the model. As mentioned previously, Gaussian noise is commonly assumed to be present in real-world images. Synthesizing Gaussian noise is also fast and easy. Thus, we add random Gaussian noise into the original images to generate their perturbed versions. ODEnets and CNN models are both trained on original images together with their perturbed versions. The standard deviation of the added Gaussian noise is randomly chosen from $\{50/255, 75/255, 100/255\}$ on the MNIST dataset, $\{15/255, 25/255, 35/255\}$ on the SVHN dataset, and $\{10/255, 15/255, 25/255\}$ on the ImgNet10. All other hyperparameters are kept the same as above.

Table 3.2 Robustness comparison of different models. We report their mean classification accuracies (%) and standard deviations (mean / std) on perturbed images from the MNIST, the SVHN, and the ImgNet10 datasets. Three types of perturbations are used—zero-mean Gaussian noise, FGSM adversarial attack, and PGD adversarial attack. The results show that ODEnets are more robust compared to CNN models.

	Gaussian noise	Adversarial attack			
MNIST	$\sigma = 100/255$	FGSM-0.3	FGSM-0.5	PGD-0.2	PGD-0.3
CNN	98.7/0.1	54.2/1.1	15.8/1.3	32.9/3.7	0.0/0.0
ODEnet	99.4/0.1	71.5/1.1	19.9/1.2	64.7/1.8	13.0/0.2
SVHN	$\sigma = 35/255$	FGSM-5/255	FGSM-8/255	PGD-3/255	PGD-5/255
CNN	90.6/0.2	25.3/0.6	12.3/0.7	32.4/0.4	14.0/0.5
ODEnet	95.1/0.1	49.4/1.0	34.7/0.5	50.9/1.3	27.2/1.4
ImgNet10	$\sigma = 25/255$	FGSM-5/255	FGSM-8/255	PGD-3/255	PGD-5/255
CNN	92.6/0.6	40.9/1.8	26.7/1.7	28.6/1.5	11.2/1.2
ODEnet	92.6/0.5	42.0/0.4	29.0/1.0	29.8/0.4	12.3/0.6

The robustness of the models is evaluated under Gaussian perturbations, FGSM adversarial examples, and PGD [Madry et al., 2018] adversarial examples. The latter is a stronger attacker compared to the FGSM. The l_∞ -norm ϵ of the PGD attack for each dataset is shown in Table 3.2. Based on the results, we observe that ODEnets consistently outperform CNN models on both two datasets. On the MNIST dataset, the ODEnet outperforms the CNN against all types of perturbations. In particular, for the PGD-0.2 adversarial examples, the accuracy of the ODEnet (64.7%) is much higher than that of the CNN (32.9%). Besides, for the PGD-0.3 attack, the CNN is completely misled by the adversarial examples, but the ODEnet can still classify perturbed images with an accuracy of 13.0%. On the SVHN dataset, ODEnets also show superior robustness in comparison to CNN models. For all the adversarial examples, ODEnets outperform CNN models by a margin of at least 10 percentage points. On the ImgNet10 dataset, the ODEnet also performs better than CNN models against all forms of adversarial examples.

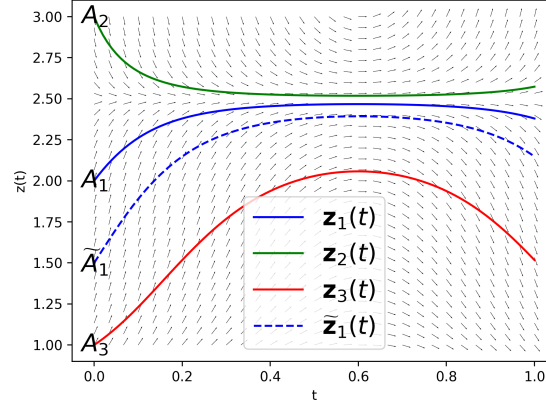


Fig. 3.2 No integral curves intersect. The integral curve starting from \widetilde{A}_1 is always sandwiched between two integral curves starting from A_1 and A_3 .

3.3.4 Insights on the robustness of ODEnets

From the results in Sections 3.3.2 and 3.3.3, we find ODEnets are more robust compared to CNN models. Here, we attempt to provide an intuitive understanding of the robustness of the neural ODE. In an ODEnet, given some datum, the FE extracts an informative feature map from the datum. The neural ODE, serving as the RM, takes as input the feature map and performs a nonlinear mapping. In practice, we use the weight decay technique during training which regularizes the norm of weights in the FE part, so that the change of feature map in terms of a small perturbation on the input can be controlled. We aim to show that, in the neural ODE, a small change on the feature map will not lead to a large deviation from the original output associated with the feature map.

Theorem 3.3.1 (ODE integral curves never intersect.) *Let $\mathbf{z}_1(t)$ and $\mathbf{z}_2(t)$ be two solutions of the ODE in (3.1) with different initial conditions, i.e. $\mathbf{z}_1(0) \neq \mathbf{z}_2(0)$. In (3.1), f_θ is continuous in t and globally Lipschitz continuous in \mathbf{z} . Then, it holds that $\mathbf{z}_1(t) \neq \mathbf{z}_2(t)$ for all $t \in [0, \infty)$.*

To illustrate Theorem 3.3.1 [Coddington and Levinson, 1955, Edwards et al., 1993], considering a simple 1-dimensional system in which the state is a scalar. As

shown in Figure 3.2, equation (3.1) has a solution $z_1(t)$ starting from $A_1 = (0, z_1(0))$, where $z_1(0)$ is the feature of some datum. Equation (3.1) also has another two solutions $z_2(t)$ and $z_3(t)$, whose starting points $A_2 = (0, z_2(0))$ and $A_3 = (0, z_3(0))$, both of which are close to A_1 . Suppose A_1 is between A_2 and A_3 . By Theorem 3.3.1, we know that the integral curve $z_1(t)$ is always sandwiched between the integral curves $z_2(t)$ and $z_3(t)$.

Now, let $\varepsilon < \min\{|z_2(0) - z_1(0)|, |z_3(0) - z_1(0)|\}$. Consider a solution $\tilde{z}_1(t)$ of equation (3.1). The integral curve $\tilde{z}_1(t)$ starts from a point $\tilde{A}_1 = (0, \tilde{z}_1(0))$. The point \tilde{A}_1 is in the ε -neighborhood of A_1 with $|\tilde{z}_1(0) - z_1(0)| < \varepsilon$. By Theorem 3.3.1, we know that $|\tilde{z}_1(T) - z_1(T)| \leq |z_3(T) - z_2(T)|$. In other words, if any perturbation smaller than ε is added to the scalar $z_1(0)$ in A_1 , the deviation from the original output $z_1(T)$ is bounded by the distance between $z_2(T)$ and $z_3(T)$. In contrast, in a CNN model, there is no such bound on the deviation from the original output. Thus, we opine that due to this non-intersecting property, ODEnets are intrinsically robust.

3.4 TisODE: boosting the robustness of neural ODEs

In the previous section, we presented an empirical study on the robustness of ODEnets and observed that ODEnets are more robust compared to CNN models. In this section, we explore how to boost the robustness of the vanilla neural ODE model further. This motivates the proposal of *time-invariant steady neural ODEs* (TisODEs).

3.4.1 Time-invariant steady neural ODEs

From the discussion in Section 3.3.4, the key to improving the robustness of neural ODEs is to control the difference between neighboring integral curves. By

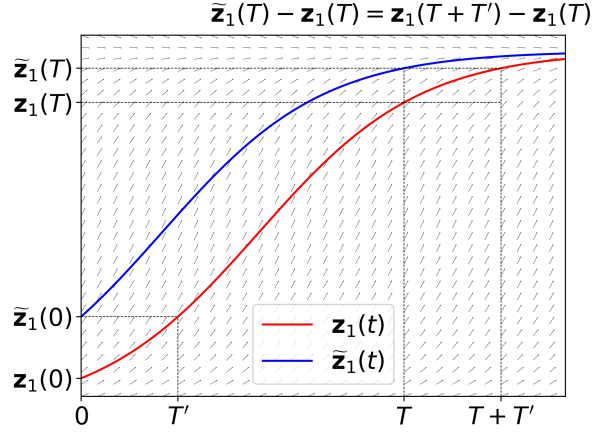


Fig. 3.3 An illustration of the time-invariant property of ODEs. We can see that the curve $\tilde{z}_1(t)$ is exactly the horizontal translation of $z_1(t)$ on the interval $[T', \infty)$.

Grownall's inequality [Coddington, 2012] (see Theorem 3.7.1 in the Appendix), we know that the difference between two terminal states is bounded by the difference between initial states multiplied by the exponential of the dynamics' Lipschitz constant. However, it is very difficult to bound the Lipschitz constant of the dynamics directly. Alternatively, we propose to achieve the goal of controlling the output deviation by following two steps: (i) removing the time dependence of the dynamics and (ii) imposing a certain steady-state constraint.

In the neural ODE characterized by equation (3.1), the dynamics $f_\theta(z(t), t)$ depends on both the state $z(t)$ at time t and the time t itself. In contrast, if the neural ODE is modified to be time-invariant, the time dependence of the dynamics is removed. Consequently, the dynamics depends *only* on the state z . So, we can rewrite the dynamics function as $f_\theta(z)$, and the neural ODE is characterized as

$$\begin{cases} \frac{dz(t)}{dt} = f_\theta(z(t)); \\ z(0) = z_{\text{in}}; \\ z_{\text{out}} = z(T). \end{cases} \quad (3.2)$$

Let $\mathbf{z}_1(t)$ be a solution of (3.2) on $[0, \infty)$ and $\varepsilon > 0$ be a small positive value. We define the set $\mathbb{M}_1 = \{(\mathbf{z}_1(t), t) | t \in [0, T], \|\mathbf{z}_1(t) - \mathbf{z}_1(0)\| \leq \varepsilon\}$. This set contains all points on the curve of $\mathbf{z}_1(t)$ during $[0, T]$ that are also inside the ε -neighborhood of $\mathbf{z}_1(0)$. For some element $(\mathbf{z}_1(T'), T') \in \mathbb{M}_1$, let $\tilde{\mathbf{z}}_1(t)$ be the solution of (3.2) which starts from $\tilde{\mathbf{z}}_1(0) = \mathbf{z}_1(T')$. Then we have

$$\tilde{\mathbf{z}}_1(t) = \mathbf{z}_1(t + T') \quad (3.3)$$

for all t in $[0, \infty)$. The property shown in equation (3.3) is known as the *time-invariant property*. It indicates that the integral curve $\tilde{\mathbf{z}}_1(t)$ is the $-T'$ shift of $\mathbf{z}_1(t)$ (Figure 3.3).

We can regard $\tilde{\mathbf{z}}_1(0)$ as a slightly perturbed version of $\mathbf{z}_1(0)$, and we are interested in how large the difference between $\tilde{\mathbf{z}}_1(T)$ and $\mathbf{z}_1(T)$ is. In a robust model, the difference should be small. By equation (3.3), we have $\|\tilde{\mathbf{z}}_1(T) - \mathbf{z}_1(T)\| = \|\mathbf{z}_1(T + T') - \mathbf{z}_1(T)\|$. Since $T' \in [0, T]$, the difference between $\mathbf{z}_1(T)$ and $\tilde{\mathbf{z}}_1(T)$ can be bounded as follows,

$$\begin{aligned} \|\tilde{\mathbf{z}}_1(T) - \mathbf{z}_1(T)\| &= \left\| \int_T^{T+T'} f_\theta(\mathbf{z}_1(t)) dt \right\| \\ &\leq \left\| \int_T^{T+T'} |f_\theta(\mathbf{z}_1(t))| dt \right\| \\ &\leq \left\| \int_T^{2T} |f_\theta(\mathbf{z}_1(t))| dt \right\|, \end{aligned} \quad (3.4)$$

where all norms are ℓ_2 norms and $|f_\theta|$ denotes the element-wise absolute operation of a vector-valued function f_θ . That is to say, the difference between $\tilde{\mathbf{z}}_1(T)$ and $\mathbf{z}_1(T)$ can be bounded by only using the information of the curve $\mathbf{z}_1(t)$. For any $t' \in [0, T]$ and element $(\mathbf{z}_1(t'), t') \in \mathbb{M}_1$, consider the integral curve that starts from $\mathbf{z}_1(t')$. The difference between the output state of this curve and $\mathbf{z}_1(T)$ satisfies inequality (3.4).

Therefore, we propose to add an additional term L_{ss} to the loss function when training the time-invariant neural ODE:

$$L_{ss} = \sum_{i=1}^N \left\| \int_T^{2T} |f_{\theta}(\mathbf{z}_i(t))| dt \right\|, \quad (3.5)$$

where N is the number of samples in the training set and $\mathbf{z}_i(t)$ is the solution whose initial state equals to the feature of the i^{th} sample. The regularization term L_{ss} is termed as the steady-state loss. This terminology “steady state” is borrowed from the dynamical systems literature. In a stable dynamical system, the states stabilize around a fixed point, known as the *steady-state*, as time tends to infinity. If we can ensure that L_{ss} is small, for each sample, the outputs of all the points in \mathbb{M}_i will stabilize around $\mathbf{z}_i(T)$. Consequently, the model is robust. This modification of the neural ODE is dubbed *Time-invariant steady neural ODE*.

3.4.2 Evaluating robustness of TisODE-based classifiers

Table 3.3 Classification accuracy (mean / std in %) on perturbed images from MNIST, SVHN and ImgNet10. To evaluate the robustness of classifiers, we use three types of perturbations, namely zero-mean Gaussian noise with standard deviation σ , FGSM attack and PGD attack. From the results, the proposed TisODE effectively improve the robustness of the vanilla neural ODE.

	Gaussian noise	Adversarial attack			
MNIST	$\sigma = 100/255$	FGSM-0.3	FGSM-0.5	PGD-0.2	PGD-0.3
CNN	98.7/0.1	54.2/1.1	15.8/1.3	32.9/3.7	0.0/0.0
ODEnet	99.4/0.1	71.5/1.1	19.9/1.2	64.7/1.8	13.0/0.2
TisODE	99.6/0.0	75.7/1.4	26.5/3.8	67.4/1.5	13.2/1.0
SVHN	$\sigma = 35/255$	FGSM-5/255	FGSM-8/255	PGD-3/255	PGD-5/255
CNN	90.6/0.2	25.3/0.6	12.3/0.7	32.4/0.4	14.0/0.5
ODEnet	95.1/0.1	49.4/1.0	34.7/0.5	50.9/1.3	27.2/1.4
TisODE	94.9/0.1	51.6/1.2	38.2/1.9	52.0/0.9	28.2/0.3
ImgNet10	$\sigma = 25/255$	FGSM-5/255	FGSM-8/255	PGD-3/255	PGD-5/255
CNN	92.6/0.6	40.9/1.8	26.7/1.7	28.6/1.5	11.2/1.2
ODEnet	92.6/0.5	42.0/0.4	29.0/1.0	29.8/0.4	12.3/0.6
TisODE	92.8/0.4	44.3/0.7	31.4/1.1	31.1/1.2	14.5/1.1

Here, we conduct experiments to evaluate the robustness of our proposed TisODE, and compare TisODE-based models with the vanilla ODEnets. We train all models with original non-perturbed images together with their Gaussian perturbed versions. The regularization parameter for the steady-state loss L_{ss} is set to be 0.1. All other hyperparameters are exactly the same as those in Section 3.3.3. We ensure that the well-trained CNNs, ODEnets, and the TisODE-based classifiers all have similar performances on the original non-perturbed images, i.e., around 99.5% for MNIST, 95.0% for SVHN, and 80.0% for ImgNet10.

From the results in Table 3.3, we can see that our proposed TisODE-based models are clearly more robust compared to vanilla ODEnets. On the MNIST dataset, when combating FGSM-0.3 attacks, the TisODE-based models outperform vanilla ODEnets by more than 4 percentage points. For the FGSM-0.5 adversarial examples, the accuracy of the TisODE-based model is 6 percentage points better. On the SVHN dataset, the TisODE-based models perform better in terms of all forms of adversarial examples. On the ImgNet10 dataset, the TisODE-based models also outperform vanilla ODE-based models on all types of perturbations. In the presence of FGSM and PGD-5/255 examples, the accuracies are enhanced by more than 2 percentage points.

3.4.3 TisODE - A generally applicable drop-in technique for improving the robustness of deep networks

In view of the excellent robustness of the TisODE, we claim that the proposed TisODE can be used as a general drop-in module for improving the robustness of deep networks. We support this claim by showing the TisODE can work in conjunction with other state-of-the-art techniques and further boost the models' robustness. These techniques include the feature denoising (FDn) method [Xie et al., 2019] and the input randomization (IR) method [Xie et al., 2018]. We

conduct experiments on the MNIST and SVHN datasets. All models are trained with original non-perturbed images together with their Gaussian perturbed versions. We show that models using the FDn/IRd technique becomes much more robust when equipped with the TisODE. In the FDn experiments, the dot-product non-local denoising layer [Xie et al., 2019] is added to the head of the fully-connected classifier.

Table 3.4 Classification accuracy (mean / std in %) on perturbed images from MNIST and SVHN. We evaluate against three types of perturbations, namely zero-mean Gaussian noise with standard deviation σ , FGSM attack and PGD attack. From the results, upon the CNNs modified with FDn and IRd, using TisODE can further improve the robustness.

	Gaussian noise	Adversarial attack			
MNIST	$\sigma = 100/255$	FGSM-0.3	FGSM-0.5	PGD-0.2	PGD-0.3
CNN	98.7/0.1	54.2/1.1	15.8/1.3	32.9/3.7	0.0/0.0
CNN-FDn	99.0/0.1	74.0/4.1	32.6/5.3	58.9/4.0	8.2/2.6
TisODE-FDn	99.4 /0.0	80.6/2.3	40.4/5.7	72.6/2.4	28.2/3.6
CNN-IRd	95.3/0.9	78.1/2.2	36.7/2.1	79.6/1.9	55.5/2.9
TisODE-IRd	97.6/0.1	86.8 /2.3	49.1 /0.2	88.8 /0.9	66.0 /0.9
SVHN	$\sigma = 35/255$	FGSM-5/255	FGSM-8/255	PGD-3/255	PGD-5/255
CNN	90.6/0.2	25.3/0.6	12.3/0.7	32.4/0.4	14.0/0.5
CNN-FDn	92.4/0.1	43.8/1.4	31.5/3.0	40.0/2.6	19.6/3.4
TisODE-FDn	95.2 /0.1	57.8/1.7	48.2/2.0	53.4/2.9	32.3/1.0
CNN-IRd	84.9/1.2	65.8/0.4	54.7/1.2	74.0/0.5	64.5/0.8
TisODE-IRd	91.7/0.5	74.4 /1.2	61.9 /1.8	81.6 /0.8	71.0 /0.5

From Table 3.4, we observe that both FDn and IRd can effectively improve the adversarial robustness of vanilla CNN models (CNN-FDn, CNN-IRd). Furthermore, combining our proposed TisODE with FDn or IRd (TisODE-FDn, TisODE-IRd), the adversarial robustness of the resultant model is significantly enhanced. For example, on the MNIST dataset, the additional use of our TisODE increases the accuracies on the PGD-0.3 examples by at least 10 percentage points for both FDn (8.2% to 28.2%) and IRd (55.5% to 66.0%). However, on both MNIST and SVHN datasets, the IRd technique improves the robustness against adversarial examples, but its performance is worse on random Gaussian noise. With the help of the

TisODE, the degradation in the robustness against random Gaussian noise can be effectively ameliorated.

3.5 Related works

In this section, we briefly review related works on the neural ODE and works concerning improving the robustness of deep neural networks.

Neural ODE: The neural ODE [Chen et al., 2018] method models the input and output as two states of a continuous-time dynamical system by approximating the dynamics of this system with trainable layers. Before the proposal of neural ODE, the idea of modeling nonlinear mappings using continuous-time dynamical systems was proposed in Weinan [2017]. Lu et al. [2017] also showed that several popular network architectures could be interpreted as the discretization of a continuous-time ODE. For example, the ResNet [He et al., 2016] and PolyNet [Zhang et al., 2017b] are associated with the Euler scheme and the FractalNet [Larsson et al., 2016] is related to the Runge-Kutta scheme. In contrast to these discretization models, neural ODEs are endowed with an intrinsic invertibility property, which yields a family of invertible models for solving inverse problems [Ardizzone et al., 2018], such as the FFJORD [Grathwohl et al., 2018].

Recently, many researchers have conducted studies on neural ODEs from the perspectives of optimization techniques, approximation capabilities, and generalization. Concerning the optimization of neural ODEs, the auto-differentiation techniques can effectively train ODEnets, but the training procedure is computationally and memory inefficient. To address this problem, Chen et al. [2018] proposed to compute gradients using the adjoint sensitivity method [Pontryagin, 2018], in which there is no need to store any intermediate quantities of the forward pass. Also in Quaglino et al. [2019], the authors proposed the SNet which

accelerates the neural ODEs by expressing their dynamics as truncated series of Legendre polynomials. Concerning the approximation capability, [Dupont et al. \[2019\]](#) pointed out the limitations in approximation capabilities of neural ODEs because of the preserving of input topology. The authors proposed an augmented neural ODE which increases the dimension of states by concatenating zeros so that complex mappings can be learned with simple flow. The most relevant work to ours concerns strategies to improve the generalization of neural ODEs. In [Liu et al. \[2019\]](#), the authors proposed the neural stochastic differential equation (SDE) by injecting random noise to the dynamics function and showed that the generalization and robustness of vanilla neural ODEs could be improved. However, our improvement on the neural ODEs is explored from a different perspective by introducing constraints on the flow. We empirically found that our proposal and the neural SDE can work in tandem to further boost the robustness of neural ODEs.

Robust Improvement: A straightforward way of improving the robustness of a model is to smooth the loss surface by controlling the spectral norm of the Jacobian matrix of the loss function [[Sokolić et al., 2017](#)]. In terms of adversarial examples [[Chen et al., 2017](#), [Carlini and Wagner, 2017](#)], researchers have proposed adversarial training strategies [[Elsayed et al., 2018](#), [Tramèr et al., 2017](#), [Madry et al., 2018](#)] in which the model is fine-tuned with adversarial examples generated in real-time. However, generating adversarial examples is not computationally efficient, and there exists a trade-off between the adversarial robustness and the performance on original non-perturbed images [[Yan et al., 2018](#), [Tsipras et al., 2019](#)]. In [Wang et al. \[2019a\]](#), the authors model the ResNet as a transport equation, in which the adversarial vulnerability can be interpreted as the irregularity of the decision boundary. Consequently, a diffusion term is introduced to enhance the robustness of the neural nets. Besides, there are also some works that propose novel architectural defense mechanisms against adversarial examples. For example, [Xie](#)

et al. [2018] utilized random resizing and random padding to destroy the specific structure of adversarial perturbations; Wang et al. [2018a] and Wang et al. [2018b] improved the robustness of neural networks by replacing the output layers with novel interpolating functions; In Xie et al. [2019], the authors designed a feature denoising filter that can remove the perturbation’s pattern from feature maps. In this work, we explore the intrinsic robustness of a specific novel architecture (neural ODE), and show that the proposed TisODE can improve the robustness of deep networks and can also work in tandem with these state-of-the-art methods to achieve further improvements.

3.6 Chapter Summary

In this chapter, we first empirically study the robustness of neural ODEs. Our studies reveal that neural ODE-based models are superior in terms of robustness compared to CNN models. We then explore how to further boost the robustness of vanilla neural ODEs and propose the TisODE. Finally, we show that the proposed TisODE outperforms the vanilla neural ODE and also can work in conjunction with other state-of-the-art techniques to further improve the robustness of deep networks. Thus, the TisODE method is an effective drop-in module for building robust deep models.

3.7 Appendices

3.7.1 Networks used on the MNIST, the SVHN, and the ImgNet10 datasets

In Table 3.5, the four arguments of the Conv layer represent the input channel, output channel, kernel size, and the stride. The two arguments of the Linear layer

Table 3.5 The architectures of the ODEnets on different datasets.

MNIST	Repetition	Layer
FE	$\times 1$	Conv(1, 64, 3, 1) + GroupNorm + ReLU
	$\times 1$	Conv(64, 64, 4, 2) + GroupNorm + ReLU
RM	$\times 2$	Conv(64, 64, 3, 1) + GroupNorm + ReLU
FCC	$\times 1$	AdaptiveAvgPool2d + Linear(64,10)
SVHN	Repetition	Layer
FE	$\times 1$	Conv(3, 64, 3, 1) + GroupNorm + ReLU
	$\times 1$	Conv(64, 64, 4, 2) + GroupNorm + ReLU
RM	$\times 2$	Conv(64, 64, 3, 1) + GroupNorm + ReLU
FCC	$\times 1$	AdaptiveAvgPool2d + Linear(64,10)
ImgNet10	Repetition	Layer
FE	$\times 1$	Conv(3, 32, 5, 2) + GroupNorm
	$\times 1$	MaxPooling(2)
	$\times 1$	BasicBlock(32, 64, 2)
	$\times 1$	MaxPooling(2)
RM	$\times 3$	BasicBlock(64, 64, 1)
FCC	$\times 1$	AdaptiveAvgPool2d + Linear(64,10)

represents the input dimension and the output dimension of this fully-connected layer. In the network on the ImgNet10, the BasicBlock refers to the standard architecture in [He et al., 2016], the three arguments of the BasicBlock represent the input channel, output channel and the stride of the Conv layers inside the block. Note that we replace the BatchNorm layers in BasicBlocks as the GroupNorm to guarantee that the dynamics of each datum is independent of other data in the same mini-batch.

3.7.2 The Construction of ImgNet10 dataset

3.7.3 Gronwall's Inequality

We formally state the Gronwall's Inequality here, following the version in [Coddington, 2012].

Table 3.6 The corresponding indexes to each class in the original ImageNet dataset

Class	Indexing		
dog	n02090721,	n02091032,	n02088094
bird	n01532829,	n01558993,	n01534433
car	n02814533,	n03930630,	n03100240
fish	n01484850,	n01491361,	n01494475
monkey	n02483708,	n02484975,	n02486261
turtle	n01664065,	n01665541,	n01667114
lizard	n01677366,	n01682714,	n01685808
bridge	n03933933,	n04366367,	n04311004
cow	n02403003,	n02408429,	n02410509
crab	n01980166,	n01978455,	n01981276

Theorem 3.7.1 *Let $U \subset \mathbb{R}^d$ be an open set. Let $f : U \times [0, T] \rightarrow \mathbb{R}^d$ be a continuous function and let $\mathbf{z}_1, \mathbf{z}_2 : [0, T] \rightarrow U$ satisfy the initial value problems:*

$$\begin{aligned}\frac{d\mathbf{z}_1(t)}{dt} &= f(\mathbf{z}_1(t), t), & \mathbf{z}_1(t) &= \mathbf{x}_1 \\ \frac{d\mathbf{z}_2(t)}{dt} &= f(\mathbf{z}_2(t), t), & \mathbf{z}_2(t) &= \mathbf{x}_2\end{aligned}$$

Assume there is a constant $C \geq 0$ such that, for all $t \in [0, T]$,

$$\|f(\mathbf{z}_2(t), t) - f(\mathbf{z}_1(t), t)\| \leq C\|\mathbf{z}_2(t) - \mathbf{z}_1(t)\|$$

Then, for any $t \in [0, T]$,

$$\|\mathbf{z}_1(t) - \mathbf{z}_2(t)\| \leq \|\mathbf{x}_2 - \mathbf{x}_1\| \cdot e^{Ct}.$$

3.7.4 More experimental results

Comparison in the setting of Adversarial training

We implement the adversarial training of the models on the MNIST dataset, and the adversarial examples for training are generated in real-time via the FGSM method (epsilon=0.3) during each epoch [Madry et al., 2018]. The results of the

adversarially trained models are shown in Table 3.7. We can observe that the neural ODE-based models are consistently more robust than CNN models. The proposed TisODE also outperforms the vanilla neural ODE.

Table 3.7 Classification accuracy (%) on perturbed images from MNIST. To evaluate the robustness of classifiers, we use three types of perturbations, namely zero-mean Gaussian noise with standard deviation σ , FGSM attack and PGD attack.

	Gaussian noise	Adversarial attack		
MNIST	$\sigma = 100/255$	FGSM-0.3	FGSM-0.5	PGD-0.3
CNN	58.0	98.4	21.1	5.3
ODEnet	84.2	99.1	36.0	12.3
TisODE	87.9	99.1	66.5	78.9

Experiments on the CIFAR10 dataset

We conduct experiments on CIFAR10 to compare the robustness of CNN and neural ODE-based models. We train all the models only with original non-perturbed images and evaluate the robustness of models against random Gaussian noise and FGSM adversarial attacks. The results are shown in Table 3.8. We can observe that the ONENet is more robust than the CNN model in terms of both the random noise and the FGSM attack. Besides, our proposal, TisODE, can improve the robustness of the vanilla neural ODE.

Table 3.8 Classification accuracy (%) on perturbed images from CIFAR10. To evaluate the robustness of classifiers, we use two types of perturbations, namely zero-mean Gaussian noise with standard deviation σ and FGSM attack.

	Gaussian noise		Adversarial attack	
CIFAR10	$\sigma = 15/255$	$\sigma = 20/255$	FGSM-8/255	FGSM-10/255
CNN	70.2	57.6	24.3	18.4
ODEnet	72.6	60.6	31.2	26.0
TisODE	74.3	62.0	33.6	26.8

Here, we control the number of parameters to be the same for all kinds of models. We use a small network, which consists of five convolutional layers and one linear layer.

Table 3.9 The architecture of the ODENet on CIFAR10.

	Repetition	Layer
FE	$\times 1$	Conv(3, 16, 3, 1) + GroupNorm + ReLU
	$\times 1$	Conv(16, 32, 3, 2) + GroupNorm + ReLU
	$\times 1$	Conv(32, 64, 3, 2) + GroupNorm + ReLU
RM	$\times 2$	Conv(64, 64, 3, 1) + GroupNorm + ReLU
FCC	$\times 1$	AdaptiveAvgPool2d + Linear(64,10)

An extension on the comparison between CNNs and ODENets

Here, we compare CNN and neural ODE-based models by controlling both the number of parameters and the number of function evaluations. We conduct experiments on the MNIST dataset, and all the models are trained only with original non-perturbed images.

For the neural ODE-based models, the time range is set from 0 to 1. We use the Euler method, and the step size is set to be 0.05. Thus the number of evaluations is $1/0.05 = 20$. For the CNN models (specifically ResNet), we repeatedly concatenate the residual block for 20 times, and these 20 blocks share the same weights. Our experiments show that, in this condition, the neural ODE-based models still outperform the CNN models (FGSM-0.15: 87.5% vs. 81.9%, FGSM-0.3: 53.4% vs. 49.7%, PGD-0.2: 11.8% vs. 4.8%).

Chapter 4

Improving Adversarial Robustness of CNNs via Channel-wise Importance-based Feature Selection

We investigate the adversarial robustness of CNNs from the perspective of channel-wise activations. By comparing normally trained and adversarially trained models, we observe that adversarial training (AT) robustifies CNNs by aligning the channel-wise activations of adversarial data with those of their natural counterparts. However, the channels that are *negatively-relevant* (NR) to predictions are still over-activated when processing adversarial data. Besides, we also observe that AT does not result in similar robustness for all classes. For the robust classes, channels with larger activation magnitudes are usually more *positively-relevant* (PR) to predictions, but this alignment does not hold for the non-robust classes. Given these observations, we hypothesize that suppressing NR channels and aligning PR ones with their relevances further enhances the robustness of CNNs under AT. To examine this hypothesis, we introduce a novel mechanism, *i.e.*, Channel-wise Importance-based Feature Selection (CIFS). The CIFS manipulates channels' acti-

variations of certain layers by generating non-negative multipliers to these channels based on their relevances to predictions. Extensive experiments on benchmark datasets including CIFAR10 and SVHN clearly verify the hypothesis and CIFS's effectiveness of robustifying CNNs.

4.1 Introduction

Convolutional neural networks (CNNs) have achieved tremendous successes in real-world applications, such as autonomous vehicles [Grigorescu et al., 2020, Hu et al., 2020] and computer-aided medical diagnoses [Trebeschi et al., 2017, Shu et al., 2020]. However, CNNs have been shown vulnerable to well-crafted (and even minute) adversarial perturbations to inputs [Szegedy et al., 2014, Goodfellow et al., 2015, Ilyas et al., 2019]. This has become hazardous in high-stakes applications such as medical diagnoses and autonomous vehicles.

Recently, many empirical defense methods have been proposed to secure CNNs against these adversarial perturbations, such as adversarial training (AT) [Madry et al., 2018], input/feature denoising [Xie et al., 2019, Du et al., 2020] and defensive distillation [Papernot et al., 2016]. AT [Madry et al., 2018], which generates adversarial data on the fly for training CNNs, has emerged as one of the most successful methods. AT effectively robustifies CNNs but leads to a clear drop in the accuracies for natural data [Tsipras et al., 2019] and suffers from the problem of overfitting to adversarial data used for training [Rice et al., 2020, Zhang et al., 2021, Chen et al., 2021]. To ameliorate these problems, researchers have proposed variants of AT, including TRADES [Zhang et al., 2019b] and Friendly-Adversarial-Training (FAT) [Zhang et al., 2020]. To further robustify CNNs under AT, many works attempt to propose novel defense mechanism to mitigate the effects of adversarial data on features [Xie et al., 2019, Du et al., 2020, Xu et al., 2019]. For

example, Xie et al. [2019] found that adversarial data result in abnormal activations in the feature maps and performed feature denoising to remove the adversarial effects. Most of these works improved robustness by identifying and suppressing abnormalities *at certain positions* across channels (commonly referred to as feature maps in CNNs), whereas the other direction, namely, the connection between robustness and irregular activations of certain *entire channels*, has received scant attention.

Since channels of CNNs’ deeper layers are capable of extracting semantic characteristic features [Zeiler and Fergus, 2014], the process of making predictions usually relies heavily on aggregating information from various channels [Bach et al., 2015]. As such, anomalous activations of certain channels may result in incorrect predictions. Thus, it is imperative to explore which channels are *entirely* irregularly activated by adversarial data and which channels’ activations benefit or degrade robustness. By utilizing this connection, we will be able to further enhance the robustness of CNNs via suppressing or promoting certain vulnerable or reliable channels respectively.

In this work, we attempt to build such a connection by comparing the channel-wise activations of non-robust (normally trained) and robustified (adversarially trained) CNNs. The *channel-wise activations* are defined as the average activation magnitudes of all features within channels [Bai et al., 2021]. To identify what types of channels appear to be abnormal under attacks, we regard *channels’ relevances* to prediction results (formally defined in Equation (4.1) as \mathbf{g}^l) as the gradients of the corresponding logits *w.r.t* channel-wise activations. The channels, whose relevances to prediction results are positive or negative ($\mathbf{g}_{[i]}^l > 0$ or $\mathbf{g}_{[i]}^l \leq 0$), are called *positively-relevant* (PR) or *negatively-relevant* (NR) channels.

On the one hand, we observe that, AT robustifies CNNs by aligning adversarial data’s channel-wise activations with those of natural data. However, we find that the

NR channels of adversarially trained CNNs are still over-activated by adversarial data (see Figure 4.1c). Thus, we wonder: *If we suppress NR channels during AT to facilitate the alignment of channels' activations, will it benefit CNNs' robustness?* On the other hand, we find that adversarially trained classification models do not enjoy similar robustness across all the classes (see Figure 4.1c and 4.1d). For classes with relatively good robustness, channels' activations usually align well with their relevances, i.e., channels with larger activations are more PR to labels. Given this phenomenon, a natural question arises: *If we align channels' activations with their relevances during AT, will it improve the robustness of CNNs?* Regarding these two questions, we propose a unified hypothesis on robustness enhancement, denoted as \mathcal{H} : Suppressing NR channels and aligning channels' activations with their relevances to prediction results benefit the robustness of CNNs.

To examine this hypothesis, we propose a novel mechanism, called Channel-wise Importance-based Feature Selection (CIFS), which adjusts channels' activations with an *importance mask* generated from channels' relevances. For a certain layer, CIFS first takes as input the representation of a data point at this layer and makes a *raw prediction* for the data point by a *probe network*. The probe serves as the surrogate for the subsequent classifier (the composition of subsequent layers) in the backbone and is jointly trained with the backbone under supervision of true labels. Then, CIFS computes the gradients of the sum of the top- k logits *w.r.t.* the channels' activations. We can obtain the *relevance* of each channel to the top- k prediction results by accumulating the gradients within the channel. Finally, CIFS generates a mask of importance scores for each channel by mapping channels' relevances monotonically to non-negative values. Through extensive experiments, we answer the two questions in the affirmative and confirm hypothesis \mathcal{H} . Indeed, our results show that CIFS clearly enhances the adversarial robustness of CNNs.

We comprehensively evaluate the robustness of CIFS-modified CNNs on benchmark datasets against various attacks. On the CIFAR10 dataset, CIFS improves the robustness of the ResNet-18 by 4 percentage points against the PGD-100 attack. We also observe that CIFS ameliorates the overfitting during AT. In particular, the robustness at the last epoch is close to that at the best epoch. Finally, we conduct an ablation study to further understand how various elements of CIFS affect the robustness enhancement, such as the top- k feedback and architectures of the probe network.

4.2 Related Works

This section briefly reviews relevant adversarial defense methods from two perspectives: adversarial training (AT)-based defense and robust network architecture design.

AT-based Defense Adversarial training (AT) defends against adversarial attacks by utilizing adversarially generated data in model training [Goodfellow et al., 2015], formulated as a minimax optimization problem. Recently variants of AT [Cai et al., 2018, Wang et al., 2019c, 2020, Wu et al., 2020, Zhang et al., 2021] have been proposed. For example, the Misclassification-Aware-AdveRsarial-Training [Wang et al., 2020] modifies the process of generating adversarial data by simultaneously applying the misclassified natural data, together with the adversarial data for model training. Recent works have shown AT robustifies CNNs but degrades the natural accuracy [Tsipras et al., 2019, Zhang et al., 2019b, Lamb et al., 2019]. To achieve a better trade-off, Zhang et al. [2019b] decomposed the adversarial prediction error into the natural error and boundary error and proposed TRADES to control both terms at the same time. Besides, inspired by curriculum learning [Cai et al., 2018, Bengio et al., 2009], Zhang et al. [2020] proposed FAT to train models with

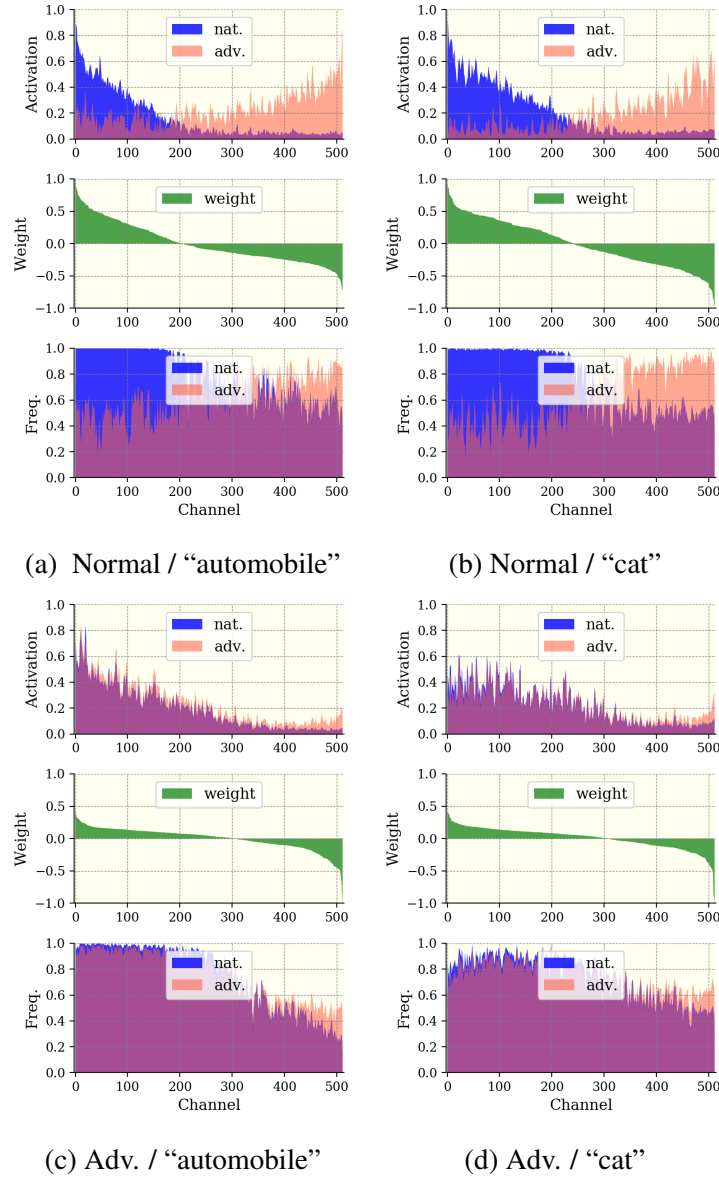


Fig. 4.1 The magnitudes of channel-wise activations (top) at the penultimate layer, their activated frequencies (bottom), and the weights of the last linear layer (middle) vs. channel indices. #/* means the CNN is trained in the # way and we plot the average activations of data from the class *. The weights corresponding to class * are sorted in the descending order and can indicate channels’ relevances to class *. The activation magnitudes and the activated frequencies of natural and adversarial (PGD-20) data are plotted according to the indices of the sorted weights. The robust accuracies on the whole CIFAR10 are 0% for the normally trained ResNet-18 model and 46.6% for the adversarially trained one (69.0% for the “automobile” class and 16.7% for the “cat” class).

increasingly adversarial data, which enhances generalization without sacrificing robustness.

Robust Network Design Other than robust training strategies, some works explored robust network architectures [Yan et al., 2020, Hsieh et al., 2019]. For instance, the work by Yan et al. [2020] showed neural ODE-based models are inherently more robust than conventional CNN models; Guo et al. [2018] demonstrated that appropriately designed higher model sparsity implies better robustness of nonlinear networks. Another line of works defended against adversarial attacks via gradient obfuscation, such as random or non-differentiable image/feature transformations [Xie et al., 2018, Du et al., 2020, Dhillon et al., 2018, Xiao et al., 2020]. However, they have been shown to be insecure to adaptive attacks [Athalye et al., 2018, Tramer et al., 2020]. Recently, many researchers have attempted to develop novel mechanisms for robustness enhancement. Xie et al. [2019] performed feature denoising to remove the adversarial effects on feature maps. Zoran et al. [2020] utilized the spatial attention mechanism to identify highlight important regions of feature maps. Most of these works manipulated CNNs’ intermediate representations in the *spatial domain*, whereas our work studies the adversarial robustness from the channel-wise activation perspective.

Channel-wise Activation Suppressing (CAS) [Bai et al., 2021], the most relevant work to ours, also studied the channel-wise activations of adversarial data. It showed channels are activated more uniformly by adversarial data compared to the natural ones, and AT improves the robustness by attempting to align the distributions of channels’ activations of natural and adversarial data. However, there are still some channels that are over-activated by adversarial data. To suppress these channels, the authors proposed CAS to adjust channels’ activations based on their importance. Although CAS empirically suppresses certain channels, the authors did not show that the suppressed channels correspond to the target ones; this means

the primary objective of CAS may not have been met. Thus, there is no guarantee CAS can enhance the robustness of CNNs (see Section 4.4.1 for further evidence on this). *In contrast*, our work first builds a connection between robustness and channels’ activations via their relevances to predictions. Then, the proposed CIFS can explicitly control channels’ activations based on their relevances. Finally, experiments demonstrate the effectiveness of CIFS on robustness enhancement.

4.3 Channel-wise Importance-based Feature Selection

In this section, we first study the adversarial robustness by comparing channels’ activations of non-robust (normally trained) and robustified (adversarially trained) CNNs. Based on our observations of AT’s effects, we propose a hypothesis on robustness enhancement via the adjustment of channels’ activations (Section 4.3.1). To examine this hypothesis, we then develop a novel mechanism, CIFS (Section 4.3.2), to manipulate channels’ activation levels according to their relevances to predictions. Finally, we verify the proposed hypothesis through extensive experiments (Section 4.3.3).

4.3.1 Non-robust CNNs vs. Robustified CNNs: A Channel-wise Activation Perspective

We compare a non-robust ResNet-18 [He et al., 2016] model with an AT-robustified one on the CIFAR10 dataset [Krizhevsky, 2009]. In ResNet-18, the representations of penultimate layer are spatially averaged for each channel, then fed into the last linear layer for making predictions. Thus, the weights of the last linear layer indicate channels’ relevances to predictions (according to the definition of channels’

relevances in Introduction). We visualize the channel-wise activation magnitudes, the activated frequencies (counted via a threshold of 1% of the largest magnitude among all channels) in the penultimate layer for both natural and adversarial data, as well as the weights of the last linear layer in Figure 4.1. The details of implementation are provided in Appendix 4.6.1.

From Figures 4.1a and 4.1b, we observe, for a non-robust ResNet-18, the activation distribution of the adversarial data is obviously mismatched with that of the natural data: natural data activate channels that are PR to predictions with high values and high frequency, while adversarial data tend to amplify the NR ones. From Figures 4.1c and 4.1d, we observe that AT robustifies the model by aligning the activation distribution of adversarial data with that of natural data. Specifically, when dealing with adversarial data, AT boosts the activation magnitudes of PR channels while suppressing the activations of NR ones. However, we observe that, for many NR channels (e.g., around 150 channels from 350th to 512th), the activations of adversarial data are much higher than those of natural data. These over-activations decrease the prediction scores corresponding to their true categories. Given this observation, we wonder (Q1): *if we suppress these NR channels to regularize the freedom of adversarial perturbations, will it further improve the model’s robustness upon AT?*

Besides, an adversarially trained model does not enjoy similar robustness for all classes, i.e., the robust accuracy of a certain class may be much higher than another (e.g., “automobile” with 69.0% vs. “cat” with 16.7% against PGD-20). Comparing the activations of these two classes (Figures 4.1c and 4.1d), we observe that, for the class with strong robustness (e.g., “automobile”), channels’ activations align better with their relevances to labels, i.e., the channel with a greater extent of activation usually corresponds to a larger weight in the linear layer. In contrast, this alignment does not hold for the class with relatively poor robustness (e.g., for class

“cat”, the most activated channels, lying between the 26th and 125th, are sub-PR to predictions). Given this phenomenon, we may ask another question (Q2): *If we scale channels’ activations based on their relevances to predictions, will it improve the model’s robustness?*

Considering the two questions above, we propose the unified hypothesis \mathcal{H} , as stated in the Introduction.

4.3.2 Importance-based Channel Adjustment

To examine the hypothesis \mathcal{H} , one needs a systematic approach to manipulate the channels, viz. selecting channels via suppressing NR ones but promoting PR ones. To this end, we introduce a mechanism, dubbed as Channel-wise Importance-based Feature Selection (CIFS). CIFS modifies layers of CNNs by adjusting channels’ activations with importance scores that are generated from the channels’ relevances to predictions.

For clearly state CIFS, we first introduce some notations: For a K -category classification problem, let $(\mathbf{x}, \mathbf{y}) \sim P_{\mathbf{xy}}$ denote the pair of the random input and its label, where $\mathbf{x} \in \mathbb{X} \subset \mathbb{R}^{n_x}$ and $\mathbf{y} \in \mathbb{Y} = \{0, 1, \dots, K-1\}$. We design an L -layer CNN-based classification model to make accurate predictions for data sampled from $P_{\mathbf{xy}}$. The l^{th} layer is denoted by $f^l(\cdot)$ and parametrized by $\theta^l \in \Theta^l$; the mapping from the input to the l^{th} layer’s output is denoted by $f^{[l]} = f^l \circ f^{l-1} \circ \dots \circ f^1$ and the combination of all the first l layers’ parameters is denoted by $\theta^{[l]}$, i.e., $\theta^{[l]} = (\theta^1, \dots, \theta^l)$. Let us examine the l^{th} layer where an input \mathbf{x} is transformed into a high-dimensional representation $\mathbf{z}^l = f^{[l]}(\mathbf{x}) \in \mathbb{R}^{n_C^l \times n_F^l}$; \mathbf{z}^l has n_C^l channels and each channel is a feature vector of length n_F^l . With these notations, we elaborate the details of CIFS in *three* steps (as shown in Figure 4.2).

1) **Surrogate Raw Prediction:** To assess channels’ relevances to predictions, a naive strategy is to compute the gradients of the final prediction with respect to

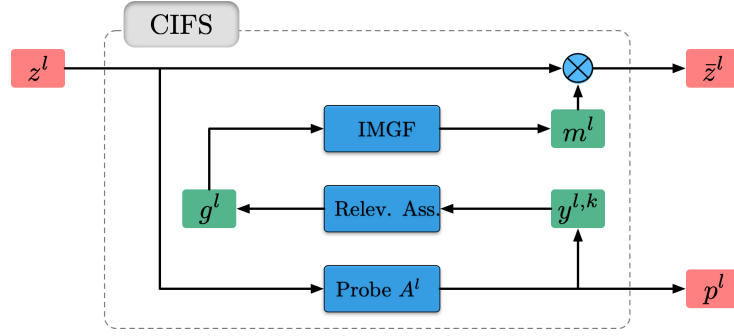


Fig. 4.2 CIFS: 1) Probe Network A^l first makes a raw prediction \mathbf{p}^l for \mathbf{z}^l . 2) Channels' relevances \mathbf{g}^l are assessed (Relev. Ass.) based on the gradients of the top- k prediction results $y^{l,k}$. 3) The IMGF generates an importance mask \mathbf{m}^l from \mathbf{g}^l for channel adjustment.

\mathbf{z}^l , i.e., $\nabla_{\mathbf{z}^l} f^{[l+1:L]}(\mathbf{z}^l)$, where $f^{[l+1:L]} = f^L \circ \dots \circ f^{l+1}$. Since we need to adjust \mathbf{z}^l with importance scores generated from $\nabla_{\mathbf{z}^l} f^{[l+1:L]}(\mathbf{z}^l)$ and send the adjusted feature $\bar{\mathbf{z}}^l$ to $f^{[l+1:L]}$ again for making the final prediction, it will result in computing the second-order derivatives during the training phase. Moreover, in practice, we may apply CIFS into multiple layers, the forward pass will involve at least the second-order gradients (the latter CIFS-modified layer is recursively called). Thus, the back-propagation has to deal with at least the third-order gradients during training. This will aggravate the problem of training instability.

Instead, inspired by the design of auxiliary classifiers in CAS [Bai et al., 2021], CIFS builds a probe network A^l as the surrogate of $f^{[l+1:L]}$ for a making raw prediction $\mathbf{p}^l = A^l(\mathbf{z}^l)$, so that we can use the gradients of \mathbf{p}^l to approximately assess the channels' relevances to the final prediction. The assessment does not involve other CIFS-modified layers. Thus, we can avoid the problem of back-propagation through high-order derivatives. The probe network A^l is parameterized by θ_A^l and $\mathbf{p}^l \in \mathbb{R}^K$ represents the vector of prediction scores/logits. We can jointly optimize A^l with the backbone network during the training phase under the supervision of true labels.

2) Relevance Assessment: With the prediction \mathbf{p}^l , we can compute the gradients of logits in \mathbf{p}^l w.r.t. \mathbf{z}^l to assess the feature’s relevances to each class. We consider the top- k prediction results ($k \geq 2$) for the assessment of channels’ relevances. As data from two semantically similar classes (e.g., “dog” and “cat”) usually share common features, the prediction for an input often assigns large scores to the classes similar to the true one and the top- k results may include several of these similar classes [Jia et al., 2020]. In case the top-1 prediction is wrong, considering the top- k results may help us reliably extract some common relevant features (see Section 4.4.2 for more evidence).

Let $y^{l,k}$ denote indices of the k largest logits of prediction \mathbf{p}^l . Let $\boldsymbol{\delta} \in \mathbb{R}^{n_C^l}$ be the channel-wise perturbation added to \mathbf{z}^l , giving the perturbed representation $\mathbf{z}_{\boldsymbol{\delta}}^l = \mathbf{z}^l + \boldsymbol{\delta} \cdot \mathbf{1}^\top$. Here $\mathbf{1} \in \mathbb{R}^{n_F^l}$ is the column vector with all elements as one, i.e., the features in the same channel are perturbed by a common value. We calculate the gradients of the sum of the top- k logits w.r.t. the channel-wise perturbation $\boldsymbol{\delta}$:

$$\mathbf{g}^l = \nabla_{\boldsymbol{\delta}} \sum_{i \in y^{l,k}} \mathbf{p}^l(\boldsymbol{\delta})_{[i]} \bigg|_{\boldsymbol{\delta}=\mathbf{0}} = \nabla_{\mathbf{z}_{\boldsymbol{\delta}}^l} \sum_{i \in y^{l,k}} A^l(\mathbf{z}_{\boldsymbol{\delta}}^l)_{[i]} \bigg|_{\mathbf{z}_{\boldsymbol{\delta}}^l=\mathbf{z}^l} \cdot \mathbf{1}, \quad (4.1)$$

where $\mathbf{g}^l = (\mathbf{g}_{[0]}^l, \dots, \mathbf{g}_{[n_C^l-1]}^l)$ represents the vector of channels’ relevances to the top- k logits. During the training phase, since the true label of \mathbf{z}^l is given, we replace the top-1 prediction in $y^{l,k}$ with the true label y and keep other prediction results untouched.

3) Importance Mask Generation: As we want to suppress or promote channels based on their relevances, we need to design proper Importance Mask Generating Functions (IMGFs), which monotonically map relevances to *non-negative* importance scores; of particular importance is to map negative relevances to values close to zero.

Here, we provide several feasible options: To answer the first question on whether suppressing NR channels enhances robustness, one can use the sigmoid function as the IMGF. With a large value of α , the sigmoid function serves as a

switch by mapping negative relevances to importance scores close to zero and the positive close to one. To answer the second question concerning aligning channel activations with their relevances, we can use the softplus or softmax function as the IMGf. Both of them can map negative relevances to values close zero and map positive relevances monotonically to positive values. These three functions are stated here for ease of reference:

- sigmoid: $\mathbf{m}_{[i]}^l = \frac{1}{1 + \exp(-\alpha \cdot \mathbf{g}_{[i]}^l)}, \quad \alpha > 0.$
- softplus: $\mathbf{m}_{[i]}^l = \frac{1}{\alpha} \cdot \log(1 + \exp(\alpha \cdot \mathbf{g}_{[i]}^l)), \quad \alpha > 0.$
- softmax: $\mathbf{m}_{[i]}^l = \frac{\exp(\mathbf{g}_{[i]}^l/T)}{\sum_j \exp(\mathbf{g}_{[j]}^l/T)}, \quad T > 0.$

The usage of these functions will be discussed in detail in Section 4.3.3. CIFS selects channels by multiplying the importance mask \mathbf{m}^l with \mathbf{z}^l as follows:

$$\bar{\mathbf{z}}^l = \mathbf{z}^l \otimes \text{repmat}(\mathbf{m}^l, 1, n_L^l), \quad (4.2)$$

where the “repmat” operation replicates the column vector \mathbf{m}^l along the second axis n_L^l times.

Training of CIFS In practice, we may apply the CIFS mechanism into several layers of a CNN. Let I denote the set of indices of these layers, and θ_A^I denote the parameters of all the probes in the CIFS-modified layers. For each input \mathbf{x} , the modified model $\tilde{f}^{[L]}$ outputs $|I|$ raw predictions and one final prediction $\mathbf{p} = \tilde{f}^{[L]}(\mathbf{x})$. Given this, we use an adaptive loss function [Bai et al., 2021] for training the model:

$$\ell_\beta(\mathbf{x}, \mathbf{y}) = \frac{1}{1 + \beta} \cdot \ell_{\text{ce}}(\mathbf{p}, \mathbf{y}) + \frac{\beta}{(1 + \beta)|I|} \cdot \sum_{l \in I} \ell_{\text{ce}}(\mathbf{p}^l, \mathbf{y}), \quad (4.3)$$

where $\ell_{\text{ce}}(\cdot, \cdot)$ denotes the cross-entropy loss and the coefficient $\beta > 0$ balances the accuracy of raw predictions by CIFS and the final prediction. Since the subsequent decisions closely depend on the channels of features selected by the previous CIFS-modified layers, we should choose a proper value of β to make sure that the raw

predictions made by CIFS are reliable. In practice, we set β to be $|I|$, and the effect of β is discussed in the ablation study (see Appendix 4.6.5). To robustify the CNN model against malicious attacks, we can train $\tilde{f}^{[L]}$ in an adversarial manner with a perturbation budget ε . Namely, we solve the following optimization problem:

$$\min_{\theta^{[L]}, \theta_A^l} \mathbb{E}_{(\mathbf{x}, \mathbf{y}) \sim P_{\mathbf{xy}}} \left[\max_{\mathbf{x}' \in \mathcal{B}(\mathbf{x}, \varepsilon, l_\infty)} \ell_\beta(\mathbf{x}', \mathbf{y}) \right], \quad (4.4)$$

where $\mathcal{B}(\mathbf{x}, \varepsilon, l_\infty) = \{\mathbf{x}' \mid \|\mathbf{x}' - \mathbf{x}\|_{l_\infty} \leq \varepsilon\}$.

4.3.3 Verification of Hypothesis \mathcal{H} on Robustness Enhancement

We verify the hypothesis \mathcal{H} by answering the two questions, **Q1** and **Q2**, in Section 4.3.1 respectively.

To answer **Q1**, we applied the sigmoid function to generate the mask \mathbf{m}^l from \mathbf{g}^l . Setting α to be large enough (here, $\alpha = 10$), we can generate importance scores close to zeros for NR channels and scores close to one for the PR ones, so that we approximately annihilate the NR channels but leave the PR ones as unchanged. We adversarially trained a ResNet-18 model and its CIFS-modified version. As shown in Figure 4.3a, the NR channels (Channel 300-512) of the vanilla ResNet-18 model are clearly activated (the average activation magnitudes of these channels are larger than 0.1; the activation frequencies are over 0.4). In contrast, the ResNet-18 with CIFS-sigmoid effectively suppresses the activation of NR channels (Channel 100th–512th in Figure 4.3b). Most of their mean activation magnitudes are smaller than 0.05, and their activation frequencies have clearly decreased. The experimental results show that, under AT, the vanilla ResNet-18 model results in a 46.64% defense rate against the PGD-20 attack while its CIFS-sigmoid modified version achieves 49.87%. More results can be found in Appendix 4.6.1. Thus, we conclude that suppressing NR channels enhances the robustness of CNNs.

To answer **Q2**, we applied the softplus and softmax functions as IMGFs to generate the mask \mathbf{m}^l from \mathbf{g}^l respectively. Here the coefficient α in the softplus is

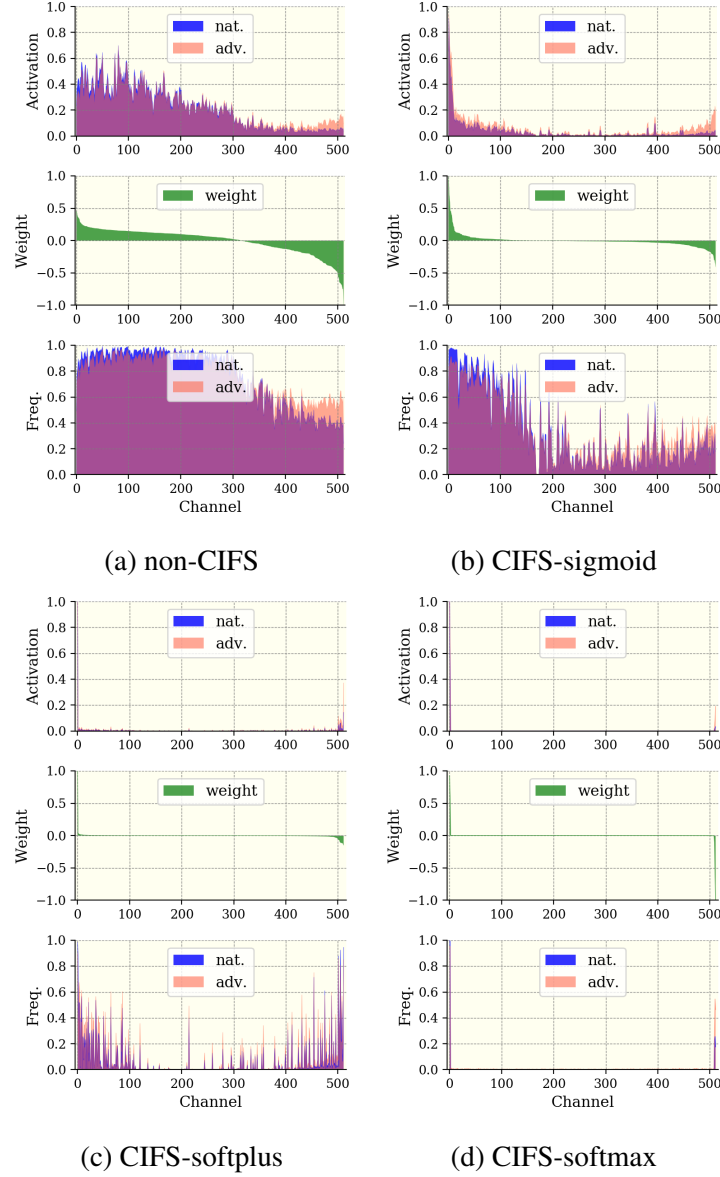


Fig. 4.3 The magnitudes of channel-wise activations (top) at the penultimate layer, their activated frequency (bottom), and the weights of the last linear layer (middle) vs. channel indices. The activations of natural data and their PGD-20 examples are averaged over all test samples in the “airplane” category. The robust accuracies against PGD-20 (on the whole dataset) are 46.64% for non-CIFS, 49.87% for the CIFS-sigmoid, 50.38% for the CIFS-softplus, and 51.23% for the CIFS-softmax respectively

set to be 5 and the temperature T in the softmax is set to be 1. From Figures 4.3c and 4.3d, we observe that, by generating importance scores positively correlated with the relevances, the model tends to completely focus on few relevant (positive

and negative) channels. The channel of the greatest weight (most PR to predictions) is activated with the highest magnitude. Most channels become irrelevant (small absolute values of weights) to the predictions and are activated at a low level. Using softplus as the IMGF (Figure 4.3c), the irrelevant channels are sparsely activated, and the activation magnitudes are smaller than 5% of the most important channel. In Figure 4.3d, this phenomenon is enhanced by using softmax as IMGF: most channels become irrelevant to predictions and are usually deactivated. We evaluated the robustness of these two CIFS-modified CNNs against PGD-20 attack. Both of them outperformed the CIFS-sigmoid and the vanilla ResNet-18 classifiers (robust accuracies of CIFS-softplus and CIFS-softmax are 50.38% and 51.23% respectively, *vs.*, 49.87% for CIFS-sigmoid and 46.64% for the vanilla ResNet-18). We also found CIFS can ameliorate the class-wise imbalance of adversarial robustness (*e.g.*, CIFS-softmax increases the PGD-20 accuracy from 16.7% to 22.3% for class “cat”). More details are provided in Appendix 4.6.1. Thus, we conclude that aligning channels activations with their relevances to predictions can further robustify CNNs upon suppressing NR ones.

Given these empirical results, we verified the hypothesis \mathcal{H} and justified that CIFS is an effective mechanism to improve the adversarial robustness of CNNs. In the following section, we conduct extensive experiments to evaluate the robustness enhancement through CIFS and study CIFS in an ablation manner.

4.4 Experiments

4.4.1 Robustness Evaluation

We utilize the CIFS to modify CNNs in different architectures to perform classification tasks on benchmark datasets, namely a ResNet-18 and a WideResNet-28-10 on the CIFAR10 [Krizhevsky, 2009] dataset, a ResNet-18 on the SVHN [Netzer et al.,

2011] dataset and a ResNet-10 on the Fashion-MNIST [Xiao et al., 2017] dataset. We train the models with the standard PGD adversarial training (AT) [Madry et al., 2018] and its variants, such as FAT [Zhang et al., 2020], to show that CIFS can work under various AT-strategies. We compare CIFS-modified CNNs with the vanilla versions as well as the CAS-modifications, where CAS [Bai et al., 2021] also modifies CNNs by adjusting channels’ activations. Here, we report the results on CIFAR10 and SVHN. Results on FMNIST are presented in Appendix 4.6.4.

Adaptive Attacks As mentioned in Section 4.3.2, each CIFS-modified layer of CNNs outputs a raw prediction. To generate adversarial examples that are as strong as possible, we follow the strategy used in CAS and attack CNNs via the adaptive loss function ℓ_β in Equation (4.3) that considers all the raw and final predictions. We let the value of β be chosen by the attacker, i.e., the attacker can try various values of β_{atk} and select one that results in the most harmful perturbations. Our setting is more challenging for defense than CAS where the *same* value of β is used for training and attack. Here, for each adversarial attack, we evaluate the robustness by choosing β_{atk} from $\{0, 0.1, 1, 2, 10, 100, \infty\}$ and report the worst robust accuracy¹. Setting $\beta_{\text{atk}} = \infty$ means the attacks completely focus on the CIFS-modified layers² and only consider the second term in Equation (4.3).

Robustness Enhancement of CIFS under AT

We adversarially train ResNet-18 and WRN-28-10 models with PGD-10 ($\epsilon = 8/255$) adversarial data. CIFS is applied to the last two residual blocks of each model. The probes for the last and penultimate blocks are a linear layer and a multi-layer perceptron (MLP) respectively. Channels’ relevances are assessed based on top-2

¹Results of various values of β are present in Appendix 4.6.2. We observe that CAS can improve the robustness of CNNs in most cases but *fail* when attackers completely focus on CAS modules.

²For $\beta_{\text{atk}} = \infty$, we consider the cases of attacking both CIFS-modified layers simultaneously and attacking each separately.

results and we use the softmax function with $T = 1$ as the IMGF. Other training details are provided in Appendix 4.6.2 and 4.6.3.

Defense Results We evaluate the robustness of CNNs against four types of white-box attacks: FGSM [Szegedy et al., 2014], PGD-20 [Madry et al., 2018], C&W [Carlini and Wagner, 2017], and PGD-100. The l_∞ -norm of the perturbations are bounded by the value of $\epsilon = 8/255$. Here, we report the robustness evaluated at the last epoch for each model. Detailed attack settings and more defense results (AutoAttack³ [Croce and Hein, 2020] and the best epochs’ results), are present in Appendix 4.6.2 and 4.6.3.

The defense results on CIFAR10 are reported in Table 4.1. We observe that, for both of the ResNet-18 and WRN-28-10 architectures, CIFS consistently outperforms the counterparts against various types of adversarial attacks. For example, the CIFS-modified WRN-28-10 can defend the PGD100 attack with a success rate of 48.74%, which exceeds the second best by more than 4 percentage points. In contrast, under the strong adaptive attack, we see that the baseline CAS cannot improve and even worsens the robustness of CNNs. The defense results on SVHN are reported in Table 4.2. The results also verify the effectiveness of CIFS on improving robustness.

Table 4.1 Robustness comparison of defense methods on CIFAR10. We report the accuracies (%) for adversarial and natural data. For each model, the results of the strongest attack are marked with an underline.

<i>ResNet-18</i>	Natural	FGSM	PGD-20	C&W	PGD-100
Vanilla	84.56	55.11	46.62	45.95	<u>44.72</u>
CAS	86.73	55.99	45.29	44.18	<u>43.22</u>
CIFS	83.86	58.86	51.23	50.16	<u>48.70</u>
<i>WRN-28-10</i>	Natural	FGSM	PGD-20	C&W	PGD-100
Vanilla	87.29	58.50	49.17	48.68	<u>47.08</u>
CAS	88.05	57.94	49.03	47.97	<u>47.25</u>
CIFS	85.56	61.34	53.74	53.20	<u>51.51</u>

³AutoAttack consists of both white and black-box attacks.

Table 4.2 Robustness comparison of defense methods on SVHN. The accuracies (%) for natural and adversarial data are reported.

ResNet-18	Natural	FGSM	PGD-20	C&W	PGD-100
Vanilla	93.72	65.87	50.35	47.89	<u>45.81</u>
CAS	94.08	65.24	48.47	46.15	<u>43.75</u>
CIFS	93.94	66.24	52.02	50.13	<u>47.49</u>

Training Procedure We train CNN classifiers in an adversarial manner for 120 epochs and adjust the learning rate with a multiplier 0.1 at epoch 75 and epoch 90. We summarize the training procedure by plotting the curves of training losses and the PGD-20 accuracies *w.r.t.* epochs in Figure 4.4. We observe the best adversarial robustness of the vanilla ResNet-18 (50.64% defense rate) appears around the 75th epoch. After epoch 75, the model starts to overfit to training data, i.e., the training loss continues decreasing, but the robust accuracy drops as well. In contrast, the overfitting problem is ameliorated by the application of CIFS. We can see that the best robust accuracy appears around the 90th epoch; After the best epoch, the training loss continues decreasing, but the robustness is maintained around the peak. This phenomenon may result from the fact that CIFS suppresses redundant channels. The model redundancy can be controlled by selecting few highly relevant channels and deactivating others. In this way, the overfitting in training is ameliorated.

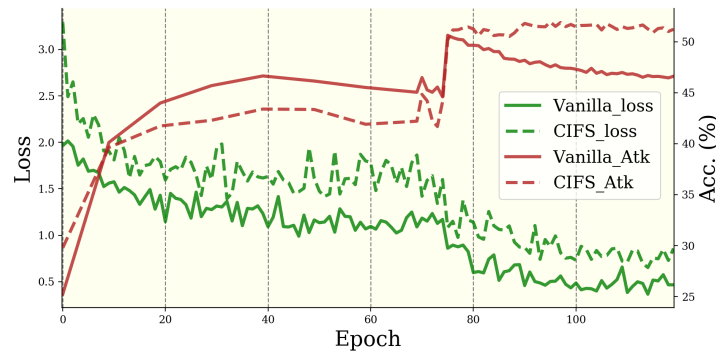


Fig. 4.4 Comparison on the training of a vanilla ResNet-18 and its CIFS-modified version. Training losses and accuracies against PGD-20 attack are plotted.

On the computation overhead, we report the training time and the evaluation time of a ResNet-18 classifier on the CIFAR10 dataset for reference. For PGD-10 adversarial training, the vanilla CNN takes 166s for each epoch while the CIFS-modified model takes 172s. For the PGD-20 evaluation, the vanilla CNN takes 53s for the CIFAR10 test set; the CIFS-modified model takes 56s instead. In short, the proposed CIFS does not result in too much extra computation.

CIFS Working in Conjunction with Variants of AT

CIFS improves the adversarial robustness by adjusting channels’ activations, which is orthogonal to defense training strategies. Here, we train the CIFS-modified CNNs with variants of AT to examine whether CIFS can work in conjunction with other state-of-the-art training-based defense techniques. We consider the FAT [Zhang et al., 2020] and TRADES [Zhang et al., 2019b] strategies. We report the defense results of FAT in Table 4.3 and provide the results of TRADES in Appendix 4.6.2. We observe that FAT training strategy improves the natural accuracy and robustness of CNNs (compared to the results in Table 4.1). Under the FAT strategy, CIFS also improves the adversarial robustness of the vanilla CNNs in both ResNet-18 and WRN-28-10 architectures.

Table 4.3 Robustness comparison of defense methods trained with FAT on CIFAR10. Comparing the accuracies (%) against the strongest attacks, we observe that CIFS clearly robustifies CNNs.

<i>ResNet-18</i>	Natural	FGSM	PGD-20	C&W	PGD-100
Vanilla	87.16	56.43	47.64	46.01	<u>45.35</u>
CIFS	86.35	59.47	51.68	51.84	49.52
<i>WRN-28-10</i>	Natural	FGSM	PGD-20	C&W	PGD-100
Vanilla	88.37	58.81	49.62	48.49	<u>47.58</u>
CIFS	86.74	60.67	51.99	52.34	49.87

4.4.2 Ablation Study

Here, we conduct an ablation study to further understand the robustness properties of CIFS. Specifically, we investigate the effects of the feedback from the top- k predictions. The ablation experiments are conducted on CIFAR10 based on the ResNet-18 model. Besides, in Appendix 4.6.5, we also study cases in which the CIFS is applied to different layers, the probe networks are in different architectures, various values of β are used for training.

Feedback from Top- k Prediction Results As is well-known, the top- k classification accuracy for $k > 1$ is always not worse than the top-1. For example, in Table 4.4, we can see that the top-2 accuracy of an adversarially trained ResNet-18 against the PGD-20 attack exceeds the top-1 accuracy by 25 percentage points. This implies that, although adversarial data can usually fool the classifier (i.e., low top-1 accuracy), the prediction confidence of the true class is still high and the corresponding score highly likely lies among the top-2 or 3 logits.

Table 4.4 Top- k accuracies (%) against adversarial attacks on CIFAR10 of an adversarially trained ResNet-18.

<i>ResNet-18</i>	top-1	top-2	top-3
FGSM	55.11	76.22	85.20
PGD-20	46.62	71.71	81.60

CIFS generates the importance mask from the raw prediction and uses it to suppress or promote channels at the current layer. The final prediction made by subsequent layers strongly depends on the channels selected by CIFS. To ensure the accuracy of final predictions, the logits used for generating importance scores should include the true label’s logit for each input so that the truly important channels will be highlighted. According to Table 4.4, if we use the top-1 logit to assess the importance of channels for PGD-20 adversarial data, the probability of incorrect assessment is over 50%. Instead, if we use the feedback from top-2 or 3

logits, the truly important channels can highly likely be promoted. The following table presents more experiments that justify this argument.

Table 4.5 Robustness comparison (%) of importance assessment based on top- k results against the PGD-20 attack. The column header $*/\#$ represents the attack point and the output prediction. For example, CIFS/Final means the model outputs the final prediction and the attacker solely focuses on the CIFS’s raw prediction.

<i>ResNet-18</i>	Natural/Final	CIFS/CIFS	CFIS/Final	Adap/Final
Vanilla	84.56	-	-	46.62
top-1	87.63	47.24	47.24	47.24
top-2	83.86	48.72	54.96	51.23
top-3	83.49	47.59	55.39	49.91

From Table 4.5, we observe that, for the top-1 case, the defense rate of ‘CIFS/CIFS’ is the same as that of ‘CIFS/Final’ and that of ‘Adap/Final.’ This implies that, once an adversarial example successfully fools the raw prediction of CIFS, the final prediction also will be incorrect. Thus, the attacker only needs to focus on the CIFS’s raw predictions to break the model. In contrast, for the top-2 case, the defense rate of ‘CIFS/Final’ exceeds the ‘CIFS/CIFS’ by 6 percentage points. This means that nearly 6% adversarial data mislead the CIFS’s raw predictions. However, through the channel adjustment via CIFS, these adversarial data are “purified”, and more relevant characteristic features are thus transmitted to subsequent layers of CNNs. As such, these adversarial data are finally classified correctly. In this case, the attacker has to exhaustively search for an adaptive loss function to generate attacks, and the CIFS-modified CNNs are safer and more reliable. More discussion on why the top- k assessment performs better and how to choose k is provided in Appendix 4.6.5.

4.5 Chapter Summary

We developed the CIFS mechanism to verify the hypothesis that suppressing NR channels and aligning PR ones with their relevances to predictions benefits

adversarial robustness. Empirical results demonstrate the effectiveness of CIFS on enhancing CNNs’ robustness.

There are two limitations of our current work: 1) We empirically verify the hypothesis \mathcal{H} , but it is still difficult to explicitly, not intuitively, explain why the adjustment of channels improves robustness. 2) Although CIFS ameliorates the overfitting during AT and improves the robustness, it sometimes leads to a bit drop in natural accuracies on certain datasets. In the future, we will attempt to address these two limitations.

4.6 Appendices

4.6.1 Details on Visualizing Channel-wise Activations

Non-robust CNNs vs. Robustified CNNs

We train ResNet-18 models to perform the classification task on the CIFAR10 dataset. The models are trained normally and adversarially. We use adversarial data generated by PGD-10 attack ($\epsilon = 8/255$, step size $\epsilon/4$, and random initialization) for adversarial training.

The ResNet-18 network consists of one convolutional layer, eight residual blocks, and one linear fully-connected (FC) layer connected successively. Each residual block contains two convolutional layers for the residual mapping. We visualize the features of the penultimate layer (the output of the eighth residual block) and the weights of the last linear layer in Figure 1. Specifically, the weights of the last FC layer for a certain class are sorted and plotted in descending order. We process the penultimate layer’s features with the global average pooling operation to obtain the channel-wise activations. For a certain class, we calculate each channel’s mean activation magnitude over all the test samples in this category. We normalize the mean channel-wise activations by dividing them by their absolute maximum.

The mean channel-wise activations are plotted according to the indices of the sorted weights. We also record the activated frequency of each channel. Here, the channel is regarded to be activated if its activation magnitude is larger than a threshold (1% of the maximum of all channels' activations).

Channel-wise Activations of CIFS-modified CNNs

We train CIFS-modified CNNs normally and adversarially by using the adaptive loss in Equation (3). We use the PGD-10 attack to generate adversarial data. We illustrate the channels' activations of CIFS-modified CNNs in Figure 3. The implementation details are same as those in Appendix 4.6.1.

In Figure 3, we show the channels' activations of data in class "airplane". Here, we plot the channels activations of data in other classes. From Figure 4.5, we see that CIFS indeed suppresses negatively-relevant (NR) channels and promotes the positively-relevant (PR) ones.

Besides, we also observe that CIFS ameliorates the class-wise imbalance of robustness under AT. In Figure 4.6, we can see that, for the data in class "cat" and class "deer", the robust accuracies of the vanilla ResNet-18 model are 16.70% and 25.50%. Modifying the vanilla model with CIFS-softmax, we can improve the robust accuracies by 5.6 and 3.3 percentage points, respectively.

4.6.2 Robustness Evaluation on CIFAR10

Robustness Enhancement of CIFS under AT

Training and Evaluation details: On the CIFAR10 dataset, we train ResNet-18 and WRN-28-10 models with PGD-10 adversarial examples ($\epsilon = 8/255$, step size $\epsilon/4$ with random initialization). The β in CIFS is set to be 2. For the ResNet-18 and its CIFS-modified version, we train models for 120 epochs with the SGD optimizer (momentum 0.9 and weight decay 0.0002). The learning rate starts from 0.1 and is

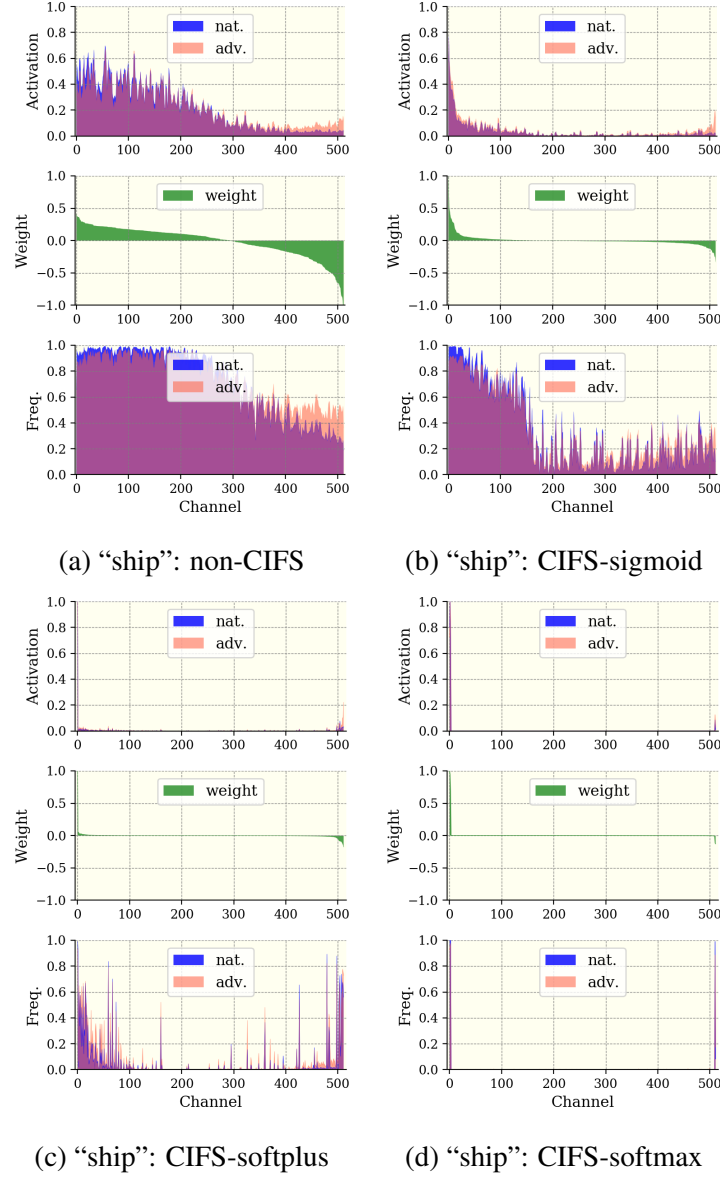


Fig. 4.5 The magnitudes of channel-wise activations (top) at the penultimate layer, their activated frequency (bottom), and the weights of the last linear layer (middle) vs. channel indices. Data from class “ship” (a-d), “automobile”(e-h), and “frog”(i-l) , are used here. The robust accuracies against PGD-20 (on the whole dataset) are 46.64% for non-CIFS, 49.87% for the CIFS-sigmoid, 50.38% for the CIFS-softplus, and 51.23% for the CIFS-softmax respectively.

multiplied with 0.1 at epoch 75 and epoch 90. For the WRN-28-10, we train model for 110 epochs with weight decay 0.0005.

In Section 4.1, we evaluate the robustness of CNNs against four white-box attacks with a perturbation budget $\epsilon = 8/255$ in l_∞ norm — FGSM, PGD-20 (step

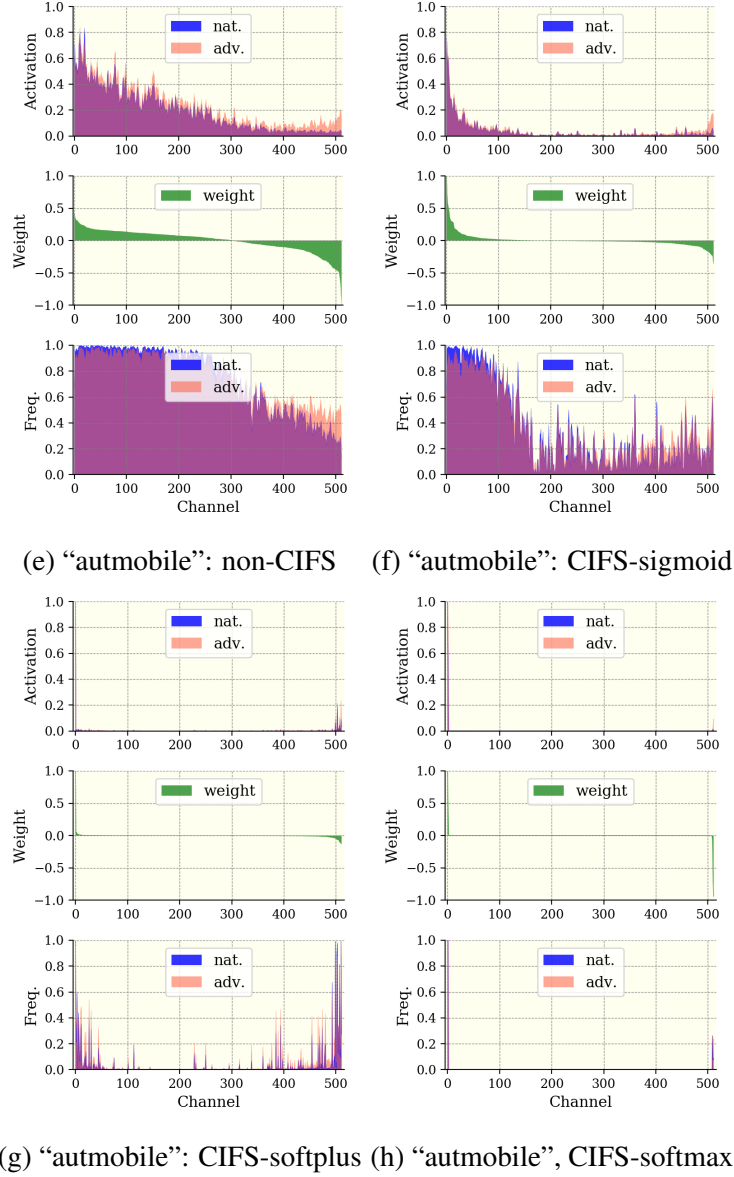


Fig. 4.5 The magnitudes of channel-wise activations (top) at the penultimate layer, their activated frequency (bottom), and the weights of the last linear layer (middle) vs. channel indices. Data from class “ship” (a-d), “automobile”(e-h), and “frog”(i-l) , are used here. The robust accuracies against PGD-20 (on the whole dataset) are 46.64% for non-CIFS, 49.87% for the CIFS-sigmoid, 50.38% for the CIFS-softplus, and 51.23% for the CIFS-softmax respectively.

size $\epsilon/10$), C&W (optimized by PGD for 30 steps with a step size $\epsilon/10$) and PGD-100 (step size $\epsilon/10$).

Robustness Evaluation with AutoAttack: Here, we also report the robust accuracies of defense methods against AutoAttack [Croce and Hein, 2020], which

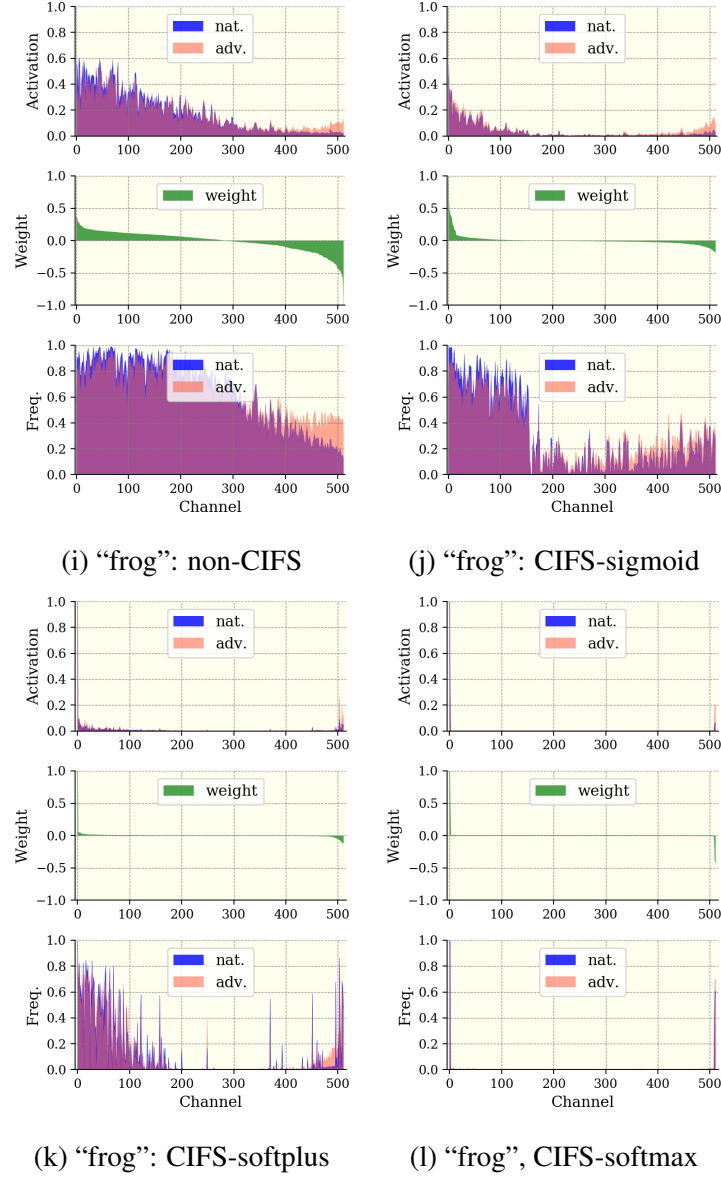


Fig. 4.5 The magnitudes of channel-wise activations (top) at the penultimate layer, their activated frequency (bottom), and the weights of the last linear layer (middle) vs. channel indices. Data from class “ship” (a-d), “automobile”(e-h), and “frog”(i-l) , are used here. The robust accuracies against PGD-20 (on the whole dataset) are 46.64% for non-CIFS, 49.87% for the CIFS-sigmoid, 50.38% for the CIFS-softplus, and 51.23% for the CIFS-softmax respectively.

consists of both white-box and black-box attacks. AutoAttack regards models to be robust at a certain data point only if the models correctly classify all types of adversarial examples generated by AutoAttack of that data point. We consider the AutoAttack including one strong white-box attack (Auto-PGD [Croce and Hein,

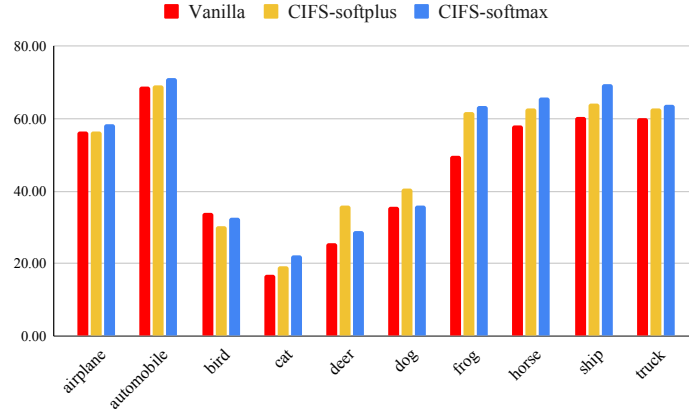


Fig. 4.6 Robust accuracies (%) of PGD-20 adversarial data for various classes of the CIFAR10 dataset.

Table 4.6 Robustness comparison of defense methods on CIFAR10. We report the last-epoch robust accuracies (%) against AutoAttack.

Model	Vanilla	CAS	CIFS
ResNet-18	44.00	42.70	46.20
WRN-28-10	47.20	46.55	49.75

2020]) and one black-box attack (Square-Attack [Andriushchenko et al., 2020]). Since the Square Attack requires many queries, we sample 2,000 images (200 per class) from the CIFAR10 for evaluation. The attack parameters are set according to the officially released AutoAttack⁴. From Table 4.6, we observe that CIFS enjoys better robustness against AutoAttack in comparison to the vanilla ResNet-18 model and its CAS-modified version.

Best-epoch robustness during training: Due to the susceptibility of over-trained models to overfitting [Rice et al., 2020], it seems reasonable to compare the results at the end of the training (and not for the best epochs) [Madry et al., 2018, Zhang et al., 2020, Rice et al., 2020]. In Section 4.1, we report the robust accuracies of ResNet-18 and WRN-28-10 models at the last epochs. Here, we also provide the results at the **best** epochs for reference.

⁴<https://github.com/fra31/auto-attack>

From Table 4.7, we see that, for the ResNet-18 architecture, the CIFS-modified model results in the similar best-epoch robustness (PGD-100) to that of the vanilla ResNet-18. For the WRN-28-10, the vanilla model has the better best-epoch robustness compared to the CIFS-modified version. This may be due to the fact that CIFS suppresses redundant channels and reduces the model capacity.

By comparing results in Table 4.7 with those in Table 1, we observe that CIFS indeed ameliorates the overfitting of AT. Specifically, the best-epoch robust accuracy of the vanilla WRN-28-10 (resp. ResNet-18) against PGD-100 attack is 54.17% (resp. 49.47%), but the last-epoch accuracy drops to 47.08% (resp. 44.72%). In contrast, for the CIFS-modified versions, the last-epoch robust accuracies against PGD-100 attack are maintained around the best-epoch ones (for WRN-28-10, from 52.03% to 51.51%; for ResNet-18, from 49.76% to 48.74%).

Table 4.7 Robustness comparison of defense methods on CIFAR10. We report the best robust accuracies (%) during training. For each model, the results of the strongest attacks are marked with an underline.

<i>ResNet-18</i>	Natural	FGSM	PGD-20	C&W	PGD-100
Vanilla	83.63	56.73	50.64	49.51	<u>49.47</u>
CAS	85.66	56.25	47.69	46.52	<u>45.69</u>
CIFS	82.46	58.98	51.94	51.25	<u>49.76</u>
<i>WRN-28-10</i>	Natural	FGSM	PGD-20	C&W	PGD-100
Vanilla	86.53	61.43	55.69	54.45	<u>54.17</u>
CAS	87.51	58.54	52.06	51.27	<u>50.69</u>
CIFS	84.67	61.03	54.09	53.76	<u>52.03</u>

Robust accuracies for various values of β_{atk} : In Section 4.1, we evaluate the robustness of CIFS-modified models by using the adaptive loss in Equation (3). For each type of attack, we assign various values to β_{atk} and report the worst robust accuracies. Here, for reference, we provide the defense results of the ResNet-18 model on CIFAR10 for different values of β_{atk} that are used in Section 4.1. The results in Table 1 (ResNet-18) are collected from Table 4.8.

Table 4.8 Robust accuracies (%) for values of β_{atk} on CIFAR10. The value “ ∞ ” means the attack only considers the second term in Equation (3). The value “ $\infty-1$ ” (resp. “ $\infty-2$ ”) means the attacker completely focuses on the first (resp. second) CIFS-modified layer. The bracketed numbers are those reported in Table 1 (ResNet-18).

<i>ResNet-18</i>	β_{atk}	Natural	FGSM	PGD-20	C&W	PGD-100
Vanilla	-	[84.56]	[55.11]	[46.62]	[45.95]	[44.72]
CAS	0	[86.73]	83.17	88.45	88.52	88.24
	0.1	-	58.61	61.36	85.51	62.40
	1	-	56.36	52.86	62.34	56.02
	2	-	56.06	49.76	54.94	50.62
	10	-	56.03	47.47	49.35	47.70
	100	-	56.02	47.04	48.36	46.74
	∞	-	56.02	47.06	48.31	46.55
	$\infty-1$	-	[55.99]	[45.29]	[44.18]	[43.22]
	$\infty-2$	-	82.68	87.87	87.79	87.72
CIFS	0	[83.86]	60.58	52.64	51.32	49.94
	0.1	-	[58.86]	51.40	50.88	49.42
	1	-	59.20	51.28	[50.16]	48.74
	2	-	59.24	[51.23]	50.28	48.79
	10	-	59.35	51.27	50.70	[48.70]
	100	-	59.38	51.41	51.04	48.80
	∞	-	59.43	51.45	51.08	48.82
	$\infty-1$	-	61.06	54.96	53.83	52.82
	$\infty-2$	-	60.03	52.30	50.92	50.03

Robustness Enhancement under TRADES

To improve the robustness of CNNs, various training-based strategies have been proposed, including vanilla adversarial training (AT) [Madry et al., 2018], friendly-adversarial training (FAT) [Zhang et al., 2020], and TRADES [Zhang et al., 2019b]. In Section 4.1, we show that CIFS can further enhance the robustness of CNNs under the vanilla AT and FAT. Here, we conduct more experiments to check whether TRADES is also suitable for CIFS.

From Table 4.9, we observe that, for the vanilla ResNet-18 model, TRADES effectively robustifies the network and outperforms its counterparts by a large margin (e.g., 48.83% of TRADES vs. 44.72% of AT against PGD-100 attack). However, for the CIFS-modified models, TRADES performs worse than AT and

Table 4.9 Robustness comparison of vanilla CNNs and their CIFS-modified version under various AT-based strategies. We report the robust accuracies (%) on various types of adversarial data.

<i>ResNet-18</i>	Natural	FGSM	PGD-20	PGD-100
Vanilla-AT	84.56	55.11	46.62	<u>44.72</u>
Vanilla-TRADES	83.96	57.09	50.27	<u>48.83</u>
Vanilla-FAT	87.16	56.43	47.64	<u>45.35</u>
CIFS-AT	83.86	58.86	51.23	<u>48.74</u>
CIFS-TRADES	85.20	54.76	46.13	<u>43.65</u>
CIFS-FAT	86.35	59.47	51.68	<u>49.52</u>

FAT. In general, CIFS-modification in combination with the FAT training strategy achieves the best robustness against various attacks.

4.6.3 Robustness Evaluation on SVHN

Training and Evaluation details: On the SVHN dataset, we train the ResNet-18 model and its CIFS-modified version with PGD-10 adversarial examples ($\epsilon = 8/255$, step size $\epsilon/4$ with random initialization). We train models for 120 epochs with the SGD optimizer (momentum 0.9 and weight decay 0.0005). The learning rate starts from 0.01 and is multiplied with 0.1 at epoch 75 and epoch 90.

In Section 4.1, we evaluate the robustness of CNNs against four white-box attacks with a perturbation budget $\epsilon = 8/255$ in l_∞ norm — FGSM, PGD-20 (step size $\epsilon/10$), C&W (optimized by PGD for 30 steps with a step size $\epsilon/10$) and PGD-100 (step size $\epsilon/10$).

Robustness Evaluation with AutoAttack: Here, we also report the robust accuracies of defense methods against AutoAttack on SVHN (Table 4.10). The evaluation settings of AutoAttack follows those in Appendix 4.6.2.

Table 4.10 Robustness comparison of defense methods on SVHN. We report the robust accuracies (%) at the last epochs.

<i>ResNet-18</i>	Vanilla	CAS	CIFS
AutoAttack	40.60	39.30	42.10

Best-epoch robustness during training: In Section 4.1, we report the robust accuracies of ResNet-18 models at the last epochs during training. Here, we report the best-epoch robustness for reference (Table 4.11). We see that CIFS modified version enjoys the better best-epoch robustness in comparison to the vanilla ResNet-18 model.

Table 4.11 Robustness comparison of defense methods on SVHN. We report the best robust accuracies (%) during training. For each model, the results of the strongest attack are marked with an underline.

<i>ResNet-18</i>	Natural	FGSM	PGD-20	C&W	PGD-100
Vanilla	93.88	66.02	51.71	48.87	<u>47.59</u>
CAS	93.90	65.53	50.52	48.39	<u>46.39</u>
CIFS	93.27	67.36	52.67	50.20	<u>48.36</u>

4.6.4 More Results on FMNIST

Training and Evaluation details: On the FMNIST dataset, we train ResNet-10 with PGD-20 adversarial examples ($\epsilon = 0.3$, step size 0.02 with random initialization). The β in CIFS is set to be 2. We train models for 120 epochs with the SGD optimizer (momentum 0.9 and weight decay 0.0002). The learning rate starts with 0.1 and is multiplied with 0.1 at epochs 45, 75 and 90.

We evaluate the robustness of the ResNet-10 models against FGSM, PGD-20, and PGD-100 white-box attacks. The perturbation is bounded by $\epsilon = 0.3$ in l_∞ norm. The step size of PGD-20 is set to be 0.01, and that of PGD-100 is set to be 0.02. Here, we report both the last-epoch robust accuracies and the best-epoch robust accuracies in Table 4.12.

Table 4.12 Robustness comparison of defense methods on FMNIST. For each model, the robust accuracies (%) of the strongest attack are remarked with an underline. For each type of attack, the best defense results are highlighted in bold. Comparing the defense rates of the strongest attacks, we observe that CIFS outperforms other defenses by a large margin.

<i>Last</i>	Natural	FGSM	PGD-40	PGD-100
Vanilla	85.19	80.52	66.47	<u>60.99</u>
CAS	86.59	82.45	65.58	<u>59.51</u>
CIFS	83.35	77.48	66.59	<u>65.50</u>
<i>Best</i>	Natural	FGSM	PGD-40	PGD-100
Vanilla	85.19	81.21	67.63	<u>63.36</u>
CAS	86.63	83.59	68.73	<u>62.65</u>
CIFS	83.32	78.55	69.05	<u>67.21</u>

4.6.5 More Results on Ablation Study

Effects of β in CIFS:

Here, we train CIFS-modified ResNet-18 models on CIFAR10 with various values of β in Equation (3). The coefficient β balances the accuracies of raw predictions and the final prediction. From Table 4.13, we observe that β values that are too small or too large values lead to drops in the accuracies of natural data and adversarial data. On the one hand, if the value of β is too small, the raw predictions made by CIFS are not reliable. Thus, the channels selected by CIFS may not be the truly relevant ones with respect to the ground-truth class. On the other hand, if the value of β is too large, the optimization procedure mostly considers the raw predictions, the final prediction (output) becomes unreliable. When $\beta = 2$, we achieve the best robustness against various types of attack.

Effects of the top- k feature assessment

In general, k should be larger than 1 but not too large.

If we use the top-1, once adv. data fool probe nets, the channels relevant to true labels will be missed, and this will lead to wrong predictions (Table 5, line top-1).

Table 4.13 Robustness accuracies (%) on CIFAR10 for CIFS with various values of β .

<i>ResNet-18</i>	Natural	FGSM	PGD-20	PGD-100
Vanilla	84.56	55.11	46.62	<u>44.72</u>
$\beta = 0.1$	75.22	53.41	48.10	<u>46.28</u>
$\beta = 1$	82.34	58.15	50.50	<u>48.35</u>
$\beta = 2$	83.86	58.86	51.23	<u>48.74</u>
$\beta = 10$	82.97	57.62	49.34	<u>47.10</u>
$\beta = 100$	75.41	52.90	45.00	<u>43.12</u>

Instead, we use top-2 for reliable channel selection. The efficacy is attributed to *two* aspects: Firstly, the top-2 accuracies of adv. data are usually high (see Table 4), thus channels relevant to top-2 logits *include those relevant to the true class*. Secondly, [Tian et al. \[2021\]](#) reports that CNNs’ predictions of adv. data usually belong to the superclass that contains true labels. Classes (e.g., cat, dog) in the same superclass (e.g., animals) usually share similar semantic features. Thus, most of the top-2 selected channels are useful for predicting the true class.

Although the top-2 selected channels may contain info about the other wrong class, the following layers (after CIFS) are capable of “purifying” features and make better predictions. This is verified by Table 5, the results in the line top-2 (CIFS/CIFS 48.72% vs. CIFS/Final 54.96%) mean that around 6% adv. data, which successfully fool probes, are still finally correctly classified. However, too large k may degrade the relevance assessment due to too much noisy info (e.g., the effect of top-3 is worse than top-2 in Table 5).

Layers to be modified

Positions of CIFS modules: Here, we try different combinations of the layers to be modified by CIFS. In CNNs, the features of deep layers are usually more characteristic in comparison to those in the shallower layers [[Zeiler and Fergus, 2014](#)], and each channel of the features captures a distinct view of the input. The predictions often depend only on the information of a few essential views

of the inputs. CIFS improves adversarial robustness by adjusting channel-wise activations. Thus, we apply CIFS to the deeper layers instead of the shallower ones. Specifically, we modify the ResNet-18 by applying CIFS at the last (P1) and/or the second last (P2) residual blocks. The experimental results are reported in Table 4.14. We observe that simultaneously applying CIFS into P1 and P2 performs the best against various attacks. Intuitively, because the features can be progressively refined, applying CIFS at P1&P2 better purifies the channels compared to applying it only at P1 or P2.

Table 4.14 Robustness (%) comparison of the positions where CIFS modules are placed.

<i>ResNet-18</i>	Natural	FGSM	PGD-20	PGD-100
Vanilla	84.56	55.11	46.62	<u>44.72</u>
P1	84.02	57.60	48.45	<u>45.95</u>
P2	82.62	56.55	47.22	<u>44.81</u>
P1-P2	83.86	58.86	51.23	48.74

Table 4.15 Robustness comparison (%) of the probe architectures in CIFS modules (at P1-P2).

<i>ResNet-18</i>	Natural	FGSM	PGD-20	PGD-100
Vanilla	84.56	55.11	46.62	<u>44.72</u>
Linear-Linear	81.52	58.33	51.32	49.07
MLP-Linear	83.86	58.86	51.23	<u>48.74</u>

Architecture of Probe Networks

Linear vs. Non-linear Probe: For a certain layer modified by CIFS, the probe network in CIFS serves as the surrogate classifier of the subsequent layers in the backbone model. Thus, the probe networks should be powerful enough to make correct predictions based on the features of this layer. For the CIFS in the last residual block, we use a linear layer network as the probe, while for the CIFS in the second last residual block, we compare the cases of using a linear layer versus using a two-layer MLP network. From Table 4.15, we observe that the MLP-Linear

combination shows a similar performance compared to the combination of two linear layers against adversarial attacks, but enjoys a clear advantage on the natural data (83.86% vs. 81.52%). This is because the features in the second last residual block are not as characteristic as those in the last block and cannot be linearly separated. The MLP can thus classify the features better than a pure linear layer.

Chapter 5

Conclusion

5.1 Summary of Contributions

The overarching theme of this thesis is building adversarially robust deep vision systems, of which three aspects were studied, i.e., evaluating adversarial robustness, enhancing robustness, and the connection between adversarial robustness and adaptivity to unseen data.

In Chapter 2, we systematically investigate the robustness of deep image denoising models. In particular, we first propose a novel PGD-based adversarial attack method, ObsAtk, to evaluate the robustness of deep image denoisers. ObsAtk is the first attack method for image denoising that considers the zero-mean assumption of natural noise. Then, we develop an adversarial training strategy, HAT, that can effectively robustify deep image denoisers. Finally, we reveal that adversarial robustness benefits the generalization to unseen types of noise, i.e., deep denoisers trained with HAT by using only Gaussian synthetic data can effectively remove various types of real-world noise that are unseen during training.

In Chapter 3 and 4, we explore new families of models that can be used to construct more robust image classifiers in comparison to vanilla convolutional layers.

Specifically, in Chapter 3, we, for the first time, study the robustness property of neural ordinary differential equations (NODEs). We empirically demonstrate that NODE-based classifiers outperform CNN-based ones against input perturbations. We further boost the robustness of NODEs by introducing the time-invariant property and imposing a steady-state constraint on the flow of ODEs. The resultant variant, TisODE, enjoys superior robustness compared to the vanilla version and can work in conjunction with other robustification techniques.

In Chapter 4, we improve the robustness of vanilla CNNs by introducing a novel channel-wise feature selection mechanism, CIFS. Inspired by the observations that adversarial training robustifies CNNs by aligning the channels' activations with their relevances to true labels, we propose CIFS to modify vanilla convolutional layers by adjusting channels' activations with multipliers generated based on their relevances. Extensive results verify the effectiveness of CIFS on robustification.

5.2 Recommendations for Future Research

The works introduced in the previous chapters naturally lead to various avenues for further research. We mention several possible extensions in this section.

Robustness of Image Restoration Algorithms Existing research papers mainly focus on the robustness of semantic-level tasks, such as classification and detection. The robustness of image restoration models, including denoising, deblurring, super-resolution, and compressive sensing, is still under-explored. Image restoration lies at the heart of intelligent vision systems. The performance of downstream image understanding tasks highly depends on the quality of the reconstruction from degraded images. Thus, it is essential to design robust image restoration models that can reliably reconstruct high-quality images against malicious degradation.

At first, we need to develop effective and efficient attack methods to evaluate the robustness of image restoration algorithms. These are open problems to solve because such attack methods have to consider the constraint about the intrinsic properties of noise/perturbations in the natural world. For example, the noise in images is usually assumed to be zero-mean; blurring kernels, which smoothen images, usually contain all non-negative elements and satisfy certain types of symmetry. Then, we can use the developed attack methods to generate adversarial examples for adversarial training. When designing adversarial training strategies, one should consider the performance on authentic data, the robustness issue, as well as the generalization to unseen types of degradation sources.

Robustifying Deep Models without Adversarial Training Adversarial training (AT) is a generally applicable framework for training robust models. However, training a large, robust model with PGD-AT consumes a massive amount of computational resources, around ten or even twenty times of those required by normal training. That is because AT needs to perform multiple times of back-propagation to generate adversarial examples for each batch of data on the fly. Although some research works attempt to accelerate AT, the computational overhead is still very high. This situation motivates us to explore novel architectures that can build robust models without adversarial training.

In Chapter 3, we study the robustness property of NODEs. Although the proposed TisODE enjoys superior robustness compared to convolutional layers, the prediction performances on adversarial data are still suboptimal. TisODE introduces a steady-state constraint on the flow of ODEs, but this constraint is not sufficient for the stability of states. For future research, one may consider a stronger regularization of the flow, i.e., the Lyapunov stability condition, to encourage the models to learn stable equilibrium points in feature spaces. The challenges here are how to ensure the Jacobian of the dynamics function to be symmetric and negative-

definite. In practice, the other challenge is how to perform backpropagation through the eigenvalue decomposition of the Jacobian if one proposes to regularize the largest eigenvalue in the loss function.

References

- Abdelrahman Abdelhamed, Stephen Lin, and Michael S. Brown. A High-Quality Denoising Dataset for Smartphone Cameras. In *IEEE/CVF Conference on Computer Vision and Pattern Recognition (CVPR)*, 2018.
- Reza Amini Gougeh, Tohid Yousefi Rezaei, and Ali Farzamnia. Medical image enhancement and deblurring. In *National Technical Seminar on Unmanned System Technology*, 2019.
- Maksym Andriushchenko, Francesco Croce, Nicolas Flammarion, and Matthias Hein. Square attack: a query-efficient black-box adversarial attack via random search. In *European Conference on Computer Vision (ECCV)*, 2020.
- Saeed Anwar and Nick Barnes. Real Image Denoising with Feature Attention. In *IEEE/CVF International Conference on Computer Vision (ICCV)*, 2019.
- Lynton Ardizzone, Jakob Kruse, Sebastian Wirkert, Daniel Rahner, Eric W Pellegrini, Ralf S Klessen, Lena Maier-Hein, Carsten Rother, and Ullrich Köthe. Analyzing inverse problems with invertible neural networks. *arXiv*, 2018.
- Anish Athalye, Nicholas Carlini, and David A. Wagner. Obfuscated gradients give a false sense of security: Circumventing defenses to adversarial examples. In *International Conference on Machine Learning (ICML)*, 2018.
- Sebastian Bach, Alexander Binder, Grégoire Montavon, Frederick Klauschen, Klaus-Robert Müller, and Wojciech Samek. On pixel-wise explanations for non-linear classifier decisions by layer-wise relevance propagation. *PloS one*, 2015.
- Yang Bai, Yuyuan Zeng, Yong Jiang, Shu-Tao Xia, Xingjun Ma, and Yisen Wang. Improving Adversarial Robustness via Channel-wise Activation Suppressing. In *International Conference on Learning Representations (ICLR)*, 2021.
- Joshua Batson and Loic Royer. Noise2Self: Blind Denoising by Self-Supervision. In *International Conference on Machine Learning (ICML)*, 2019.
- Jatin Bedi and Durga Toshniwal. Deep learning framework to forecast electricity demand. *Applied energy*, 2019.

- Yoshua Bengio, Jérôme Louradour, Ronan Collobert, and Jason Weston. Curriculum learning. In *International Conference on Machine Learning (ICML)*, 2009.
- Stephen Boyd, Stephen P Boyd, and Lieven Vandenberghe. *Convex optimization*. Cambridge university press, 2004.
- Qi-Zhi Cai, Chang Liu, and Dawn Song. Curriculum adversarial training. In *International Joint Conferences on Artificial Intelligence (IJCAI)*, 2018.
- Nicholas Carlini and David Wagner. Towards evaluating the robustness of neural networks. In *IEEE Symposium on Security and Privacy*, 2017.
- Pin-Yu Chen, Huan Zhang, Yash Sharma, Jinfeng Yi, and Cho-Jui Hsieh. Zoo: Zeroth order optimization based black-box attacks to deep neural networks without training substitute models. In *ACM Workshop on Artificial Intelligence and Security*, 2017.
- Tian Qi Chen, Yulia Rubanova, Jesse Bettencourt, and David K Duvenaud. Neural ordinary differential equations. In *Advances in Neural Information Processing Systems (NeurIPS)*, 2018.
- Tianlong Chen, Zhenyu Zhang, Sijia Liu, Shiyu Chang, and Zhangyang Wang. Robust overfitting may be mitigated by properly learned smoothening. In *International Conference on Learning Representations (ICLR)*, 2021.
- Jun-Ho Choi, Huan Zhang, Jun-Hyuk Kim, Cho-Jui Hsieh, and Jong-Seok Lee. Evaluating Robustness of Deep Image Super-Resolution against Adversarial Attacks. In *IEEE/CVF International Conference on Computer Vision (ICCV)*, 2019.
- Jun-Ho Choi, Huan Zhang, Jun-Hyuk Kim, Cho-Jui Hsieh, and Jong-Seok Lee. Deep Image Destruction: A Comprehensive Study on Vulnerability of Deep Image-to-Image Models against Adversarial Attacks. *arXiv*, 2021.
- Moustapha Cissé, Piotr Bojanowski, Edouard Grave, Yann N. Dauphin, and Nicolas Usunier. Parseval networks: Improving robustness to adversarial examples. In *International Conference on Machine Learning (ICML)*, 2017.
- Earl A Coddington. *An introduction to ordinary differential equations*. Courier Corporation, 2012.
- Earl A Coddington and Norman Levinson. *Theory of ordinary differential equations*. Tata McGraw-Hill Education, 1955.
- Francesco Croce and Matthias Hein. Sparse and imperceivable adversarial attacks. In *IEEE/CVF International Conference on Computer Vision (ICCV)*, 2019.

- Francesco Croce and Matthias Hein. Reliable evaluation of adversarial robustness with an ensemble of diverse parameter-free attacks. In *International Conference on Machine Learning (ICML)*, 2020.
- Kostadin Dabov, Alessandro Foi, Vladimir Katkovnik, and Karen Egiazarian. Image Denoising by Sparse 3-D Transform-Domain Collaborative Filtering. *IEEE Transactions on Image Processing*, 2007.
- Jia Deng, Wei Dong, Richard Socher, Li-Jia Li, Kai Li, and Li Fei-Fei. Imagenet: A large-scale hierarchical image database. In *IEEE/CVF Conference on Computer Vision and Pattern Recognition (CVPR)*, 2009.
- Guneet S. Dhillon, Kamyar Azizzadenesheli, Zachary C. Lipton, Jeremy Bernstein, Jean Kossaifi, Aran Khanna, and Animashree Anandkumar. Stochastic activation pruning for robust adversarial defense. In *International Conference on Learning Representations (ICLR)*, 2018.
- Jiawei Du, Hanshu Yan, Vincent Y. F. Tan, Joey Tianyi Zhou, Rick Siow Mong Goh, and Jiashi Feng. RAIN: A Simple Approach for Robust and Accurate Image Classification Networks. *arXiv*, 2020.
- Yilun Du and Igor Mordatch. Implicit generation and modeling with energy based models. *Advances in Neural Information Processing Systems (NeurIPS)*, 2019.
- Emilien Dupont, Arnaud Doucet, and Yee Whye Teh. Augmented neural odes. *arXiv*, 2019.
- Charles Henry Edwards, David E Penney, and David Calvis. *Elementary differential equations with boundary value problems*. Prentice Hall Englewood Cliffs, NJ, 1993.
- Gamaleldin F Elsayed, Shreya Shankar, Brian Cheung, Nicolas Papernot, Alex Kurakin, Ian Goodfellow, and Jascha Sohl-Dickstein. Adversarial examples that fool both human and computer vision. *arXiv*, 2018.
- Zhe Gan, Yen-Chun Chen, Linjie Li, Chen Zhu, Yu Cheng, and Jingjing Liu. Large-scale adversarial training for vision-and-language representation learning. *Advances in Neural Information Processing Systems (NeurIPS)*, 2020.
- Ruiqi Gao, Tianle Cai, Haochuan Li, Cho-Jui Hsieh, Liwei Wang, and Jason D. Lee. Convergence of Adversarial Training in Overparametrized Neural Networks. In *Advances in Neural Information Processing Systems (NeurIPS)*, 2019.
- Lovedeep Gondara. Medical image denoising using convolutional denoising autoencoders. In *International Conference on Data Mining Workshops*, 2016.
- Ian Goodfellow, Jean Pouget-Abadie, Mehdi Mirza, Bing Xu, David Warde-Farley, Sherjil Ozair, Aaron Courville, and Yoshua Bengio. Generative adversarial nets. *Advances in Neural Information Processing Systems (NeurIPS)*, 2014.

- Ian J. Goodfellow, Jonathon Shlens, and Christian Szegedy. Explaining and harnessing adversarial examples. In *International Conference on Learning Representations (ICLR)*, 2015.
- Will Grathwohl, Ricky TQ Chen, Jesse Betterncourt, Ilya Sutskever, and David Duvenaud. Ffjord: Free-form continuous dynamics for scalable reversible generative models. *arXiv*, 2018.
- Sorin Grigorescu, Bogdan Trasnea, Tiberiu Cocias, and Gigel Macesanu. A survey of deep learning techniques for autonomous driving. *Journal of Field Robotics*, 2020.
- Chuan Guo, Jacob Gardner, Yurong You, Andrew Gordon Wilson, and Kilian Weinberger. Simple black-box adversarial attacks. In *International Conference on Machine Learning (ICML)*, 2019a.
- Shi Guo, Zifei Yan, Kai Zhang, Wangmeng Zuo, and Lei Zhang. Toward Convolutional Blind Denoising of Real Photographs. In *IEEE/CVF Conference on Computer Vision and Pattern Recognition (CVPR)*, 2019b.
- Yiwen Guo, Chao Zhang, Changshui Zhang, and Yurong Chen. Sparse dnns with improved adversarial robustness. In *Advances in Neural Information Processing Systems (NeurIPS)*, 2018.
- Kaiming He, Xiangyu Zhang, Shaoqing Ren, and Jian Sun. Deep Residual Learning for Image Recognition. In *IEEE/CVF Conference on Computer Vision and Pattern Recognition (CVPR)*, 2016.
- Kaiming He, Georgia Gkioxari, Piotr Dollár, and Ross Girshick. Mask r-cnn. In *IEEE/CVF International Conference on Computer Vision (ICCV)*, 2017.
- Dan Hendrycks and Thomas G Dietterich. Benchmarking neural network robustness to common corruptions and surface variations. *arXiv*, 2018.
- Yu-Lun Hsieh, Minhao Cheng, Da-Cheng Juan, Wei Wei, Wen-Lian Hsu, and Cho-Jui Hsieh. On the robustness of self-attentive models. In *Annual Meeting of the Association for Computational Linguistics*, 2019.
- Dapeng Hu, Jian Liang, Qibin Hou, Hanshu Yan, Yunpeng Chen, Shuicheng Yan, and Jiashi Feng. Panda: Prototypical unsupervised domain adaptation. *arXiv*, 2020.
- Andrew Ilyas, Shibani Santurkar, Dimitris Tsipras, Logan Engstrom, Brandon Tran, and Aleksander Madry. Adversarial examples are not bugs, they are features. In *Advances in Neural Information Processing Systems (NeurIPS)*, 2019.
- Jinyuan Jia, Xiaoyu Cao, Binghui Wang, and Neil Zhenqiang Gong. Certified robustness for top-k predictions against adversarial perturbations via randomized smoothing. In *International Conference on Learning Representations (ICLR)*, 2020.

- Byungseok Kang and Hyunseung Choo. A deep-learning-based emergency alert system. *ICT Express*, 2016.
- Harini Kannan, Alexey Kurakin, and Ian Goodfellow. Adversarial Logit Pairing. *arXiv*, 2018.
- Diederik P Kingma and Max Welling. Auto-encoding variational bayes. *arXiv*, 2013.
- Alex Krizhevsky. Learning multiple layers of features from tiny images. *Master's thesis, University of Toronto*, 2009.
- Alex Krizhevsky, Ilya Sutskever, and Geoffrey E Hinton. Imagenet classification with deep convolutional neural networks. In *Advances in Neural Information Processing Systems (NeurIPS)*, 2012.
- Alexey Kurakin, Ian Goodfellow, and Samy Bengio. Adversarial examples in the physical world. *arXiv*, 2017.
- Alex Lamb, Vikas Verma, Juho Kannala, and Yoshua Bengio. Interpolated Adversarial Training: Achieving Robust Neural Networks without Sacrificing Too Much Accuracy. *arXiv*, 2019.
- Gustav Larsson, Michael Maire, and Gregory Shakhnarovich. Fractalnet: Ultra-deep neural networks without residuals. *arXiv*, 2016.
- Yann LeCun, Léon Bottou, Yoshua Bengio, and Patrick Haffner. Gradient-based learning applied to document recognition. *Proceedings of IEEE*, 1998.
- Yann LeCun, Yoshua Bengio, and Geoffrey Hinton. Deep learning. *Nature*, 2015.
- Jaakko Lehtinen, Jacob Munkberg, Jon Hasselgren, Samuli Laine, Tero Karras, Miika Aittala, and Timo Aila. Noise2Noise: Learning Image Restoration without Clean Data. In *International Conference on Machine Learning (ICML)*, 2018.
- Zhetong Liang, Jianrui Cai, Zisheng Cao, and Lei Zhang. Cameranet: A two-stage framework for effective camera isp learning. *IEEE Transactions on Image Processing*, 2021.
- Fangzhou Liao, Ming Liang, Yinpeng Dong, Tianyu Pang, Xiaolin Hu, and Jun Zhu. Defense against adversarial attacks using high-level representation guided denoiser. In *IEEE/CVF Conference on Computer Vision and Pattern Recognition (CVPR)*, 2018.
- Xuanqing Liu, Si Si, Qin Cao, Sanjiv Kumar, and Cho-Jui Hsieh. Neural sde: Stabilizing neural ode networks with stochastic noise. *arXiv*, 2019.
- Yanpei Liu, Xinyun Chen, Chang Liu, and Dawn Song. Delving into transferable adversarial examples and black-box attacks. *arXiv*, 2016.

- Ze Liu, Yutong Lin, Yue Cao, Han Hu, Yixuan Wei, Zheng Zhang, Stephen Lin, and Baining Guo. Swin transformer: Hierarchical vision transformer using shifted windows. In *IEEE/CVF International Conference on Computer Vision (ICCV)*, 2021.
- Yiping Lu, Aoxiao Zhong, Quanzheng Li, and Bin Dong. Beyond finite layer neural networks: Bridging deep architectures and numerical differential equations. *arXiv*, 2017.
- Siwei Ma, Xinfeng Zhang, Chuanmin Jia, Zhenghui Zhao, Shiqi Wang, and Shanshe Wang. Image and video compression with neural networks: A review. *IEEE Transactions on Circuits and Systems for Video Technology*, 2019.
- Aleksander Madry, Aleksandar Makelov, Ludwig Schmidt, Dimitris Tsipras, and Adrian Vladu. Towards Deep Learning Models Resistant to Adversarial Attacks. In *International Conference on Learning Representations (ICLR)*, 2018.
- Shervin Minaee, Yuri Y Boykov, Fatih Porikli, Antonio J Plaza, Nasser Kehtarnavaz, and Demetri Terzopoulos. Image segmentation using deep learning: A survey. *IEEE Transactions on Pattern Analysis and Machine Intelligence*, 2021.
- Md Moniruzzaman, Syed Mohammed Shamsul Islam, Mohammed Bennamoun, and Paul Lavery. Deep learning on underwater marine object detection: A survey. In *International Conference on Advanced Concepts for Intelligent Vision Systems*, 2017.
- Aamir Mustafa, Salman H. Khan, Munawar Hayat, Roland Goecke, Jianbing Shen, and Ling Shao. Adversarial defense by restricting the hidden space of deep neural networks. In *IEEE/CVF International Conference on Computer Vision (ICCV)*, 2019.
- Yuval Netzer, Tao Wang, Adam Coates, Alessandro Bissacco, Bo Wu, and Andrew Y Ng. Reading digits in natural images with unsupervised feature learning. In *NeurIPS Workshop on Deep Learning and Unsupervised Feature Learning*, 2011.
- Tongyao Pang, Huan Zheng, Yuhui Quan, and Hui Ji. Recorrupted-to-Recorrupted: Unsupervised Deep Learning for Image Denoising. In *IEEE/CVF Conference on Computer Vision and Pattern Recognition (CVPR)*, 2021.
- Nicolas Papernot, Patrick McDaniel, Xi Wu, Somesh Jha, and Ananthram Swami. Distillation as a Defense to Adversarial Perturbations against Deep Neural Networks. *arXiv*, 2016.
- Adam Paszke, Sam Gross, Soumith Chintala, Gregory Chanan, Edward Yang, Zachary DeVito, Zeming Lin, Alban Desmaison, Luca Antiga, and Adam Lerer. Automatic differentiation in pytorch. In *NeurIPS 2017 Workshop Autodiff*, 2017.

- Lev Semenovich Pontryagin. *Mathematical theory of optimal processes*. Routledge, 2018.
- Alessio Quaglino, Marco Gallieri, Jonathan Masci, and Jan Koutník. Accelerating neural odes with spectral elements. *arXiv*, 2019.
- Pradheepan Raghavan and Neamat El Gayar. Fraud detection using machine learning and deep learning. In *International Conference on Computational Intelligence and Knowledge Economy (ICCIKE)*, 2019.
- Dhruv Rathi, Sushant Jain, and S Indu. Underwater fish species classification using convolutional neural network and deep learning. In *International Conference on Advances in Pattern Recognition (ICAPR)*, 2017.
- Leslie Rice, Eric Wong, and J. Zico Kolter. Overfitting in adversarially robust deep learning. In *International Conference on Machine Learning (ICML)*, 2020.
- Pouya Samangouei, Maya Kabkab, and Rama Chellappa. Defense-gan: Protecting classifiers against adversarial attacks using generative models. *arXiv*, 2018.
- Swami Sankaranarayanan, Arpit Jain, Rama Chellappa, and Ser-Nam Lim. Regularizing deep networks using efficient layerwise adversarial training. In *Association for the Advancement of Artificial Intelligence (AAAI)*, 2018.
- Amartya Sanyal, Varun Kanade, Philip H. S. Torr, and Puneet K. Dokania. Robustness via Deep Low-Rank Representations. *arXiv*, 2020.
- Ali Shafahi, Mahyar Najibi, Amin Ghiasi, Zheng Xu, John Dickerson, Christoph Studer, Larry S. Davis, Gavin Taylor, and Tom Goldstein. Adversarial Training for Free! In *Advances in Neural Information Processing Systems (NeurIPS)*, 2019.
- Dinggang Shen, Guorong Wu, and Heung-Il Suk. Deep learning in medical image analysis. *Annual review of biomedical engineering*, 2017.
- Chi Shu, Hanshu Yan, Kan Lin, Chwee Ming Lim, Wei Zheng, Jiashi Feng, and Zhiwei Huang. Enhancing in vivo nose cancer detection with rapid fiberoptic raman and deep learning techniques. In *Optical Biopsy XVIII: Toward Real-Time Spectroscopic Imaging and Diagnosis*, 2020.
- Jure Sokolić, Raja Giryes, Guillermo Sapiro, and Miguel RD Rodrigues. Robust large margin deep neural networks. *IEEE Transactions on Signal Processing*, 2017.
- Christian Szegedy, Wojciech Zaremba, Ilya Sutskever, Joan Bruna, Dumitru Erhan, Ian Goodfellow, and Rob Fergus. Intriguing properties of neural networks. *arXiv*, 2013.

- Christian Szegedy, Wojciech Zaremba, Ilya Sutskever, Joan Bruna, Dumitru Erhan, Ian J. Goodfellow, and Rob Fergus. Intriguing properties of neural networks. In *International Conference on Learning Representations (ICLR)*, 2014.
- Qi Tian, Kun Kuang, Kelu Jiang, Fei Wu, and Yisen Wang. Analysis and applications of class-wise robustness in adversarial training. In *ACM SIGKDD Conference on Knowledge Discovery & Data Mining (KDD)*, 2021.
- Florian Tramèr, Alexey Kurakin, Nicolas Papernot, Ian Goodfellow, Dan Boneh, and Patrick McDaniel. Ensemble adversarial training: Attacks and defenses. *arXiv*, 2017.
- Florian Tramer, Nicholas Carlini, Wieland Brendel, and Aleksander Madry. On Adaptive Attacks to Adversarial Example Defenses. *arXiv*, 2020.
- Stefano Trebeschi, Joost JM van Griethuysen, Doenja MJ Lambregts, Max J Lahaye, Chintan Parmar, Frans CH Bakers, Nicky HGM Peters, Regina GH Beets-Tan, and Hugo JWL Aerts. Deep learning for fully-automated localization and segmentation of rectal cancer on multiparametric mr. *Nature Scientific Reports*, 2017.
- Dimitris Tsipras, Shibani Santurkar, Logan Engstrom, Alexander Turner, and Aleksander Madry. Robustness may be at odds with accuracy. In *International Conference on Learning Representations (ICLR)*, 2019.
- Dmitry Ulyanov, Andrea Vedaldi, and Victor Lempitsky. Deep Image Prior. In *IEEE/CVF Conference on Computer Vision and Pattern Recognition (CVPR)*, 2018.
- Matthew Veres and Medhat Moussa. Deep learning for intelligent transportation systems: A survey of emerging trends. *IEEE Transactions on Intelligent transportation systems*, 2019.
- Aladin Virmaux and Kevin Scaman. Lipschitz regularity of deep neural networks: analysis and efficient estimation. In *Advances in Neural Information Processing Systems*, 2018.
- Bao Wang, Alex T Lin, Zuoqiang Shi, Wei Zhu, Penghang Yin, Andrea L Bertozzi, and Stanley J Osher. Adversarial defense via data dependent activation function and total variation minimization. *arXiv*, 2018a.
- Bao Wang, Xiyang Luo, Zhen Li, Wei Zhu, Zuoqiang Shi, and Stanley Osher. Deep neural nets with interpolating function as output activation. In *Advances in Neural Information Processing Systems (NeurIPS)*, 2018b.
- Bao Wang, Zuoqiang Shi, and Stanley Osher. Resnets ensemble via the feynman-kac formalism to improve natural and robust accuracies. *Advances in Neural Information Processing Systems (NeurIPS)*, 2019a.

- Huaizhi Wang, Zhenxing Lei, Xian Zhang, Bin Zhou, and Jianchun Peng. A review of deep learning for renewable energy forecasting. *Energy Conversion and Management*, 2019b.
- Mei Wang and Weihong Deng. Deep face recognition: A survey. *Neurocomputing*, 2021.
- Yisen Wang, Xingjun Ma, James Bailey, Jinfeng Yi, Bowen Zhou, and Quanquan Gu. On the convergence and robustness of adversarial training. In *International Conference on Machine Learning (ICML)*, 2019c.
- Yisen Wang, Difan Zou, Jinfeng Yi, James Bailey, Xingjun Ma, and Quanquan Gu. Improving adversarial robustness requires revisiting misclassified examples. In *International Conference on Learning Representations (ICLR)*, 2020.
- E Weinan. A proposal on machine learning via dynamical systems. *Communications in Mathematics and Statistics*, 2017.
- Eric Wong, Leslie Rice, and J. Zico Kolter. Fast is better than free: Revisiting adversarial training. In *International Conference on Learning Representations (ICLR)*, 2020.
- Dongxian Wu, Shu-Tao Xia, and Yisen Wang. Adversarial weight perturbation helps robust generalization. In *Advances in Neural Information Processing Systems (NeurIPS)*, 2020.
- Chang Xiao, Peilin Zhong, and Changxi Zheng. Enhancing adversarial defense by k-winners-take-all. In *International Conference on Learning Representations (ICLR)*, 2020.
- Han Xiao, Kashif Rasul, and Roland Vollgraf. Fashion-mnist: a novel image dataset for benchmarking machine learning algorithms. *arXiv*, 2017.
- Cihang Xie, Jianyu Wang, Zhishuai Zhang, Zhou Ren, and Alan L. Yuille. Mitigating adversarial effects through randomization. In *International Conference on Learning Representations (ICLR)*, 2018.
- Cihang Xie, Yuxin Wu, Laurens van der Maaten, Alan L. Yuille, and Kaiming He. Feature denoising for improving adversarial robustness. In *IEEE/CVF Conference on Computer Vision and Pattern Recognition (CVPR)*, 2019.
- Jun Xu, Lei Zhang, David Zhang, and Xiangchu Feng. Multi-channel Weighted Nuclear Norm Minimization for Real Color Image Denoising. In *IEEE/CVF International Conference on Computer Vision (ICCV)*, 2017.
- Jun Xu, Hui Li, Zhetong Liang, David Zhang, and Lei Zhang. Real-world Noisy Image Denoising: A New Benchmark. *arXiv*, 2018.

- Kaidi Xu, Sijia Liu, Gaoyuan Zhang, Mengshu Sun, Pu Zhao, Quanfu Fan, Chuang Gan, and Xue Lin. Interpreting Adversarial Examples by Activation Promotion and Suppression. *arXiv*, 2019.
- Kaidi Xu, Gaoyuan Zhang, Sijia Liu, Quanfu Fan, Mengshu Sun, Hongge Chen, Pin-Yu Chen, Yanzhi Wang, and Xue Lin. Adversarial t-shirt! evading person detectors in a physical world. In *European Conference on Computer Vision (ECCV)*, 2020.
- Hanshu Yan, Xuan Chen, Vincent YF Tan, Wenhan Yang, Joe Wu, and Jiashi Feng. Unsupervised image noise modeling with self-consistent gan. *arXiv*, 2019.
- Hanshu Yan, Jiawei Du, Vincent Y. F. Tan, and Jiashi Feng. On robustness of neural ordinary differential equations. In *International Conference on Learning Representations (ICLR)*, 2020.
- Hanshu Yan, Jingfeng Zhang, Gang Niu, Jiashi Feng, Vincent Tan, and Masashi Sugiyama. CIFS: Improving Adversarial Robustness of CNNs via Channel-wise Importance-based Feature Selection. In *International Conference on Machine Learning (ICML)*, 2021.
- Hanshu Yan, Jingfeng Zhang, Jiashi Feng, Masashi Sugiyama, and Vincent YF Tan. Towards adversarially robust deep image denoising. *arXiv*, 2022.
- Ziang Yan, Yiwen Guo, and Changshui Zhang. Deep defense: Training dnns with improved adversarial robustness. In *Advances in Neural Information Processing Systems (NeurIPS)*, 2018.
- Yuzhe Yang, Guo Zhang, Dina Katabi, and Zhi Xu. Me-net: Towards effective adversarial robustness with matrix estimation. *arXiv*, 2019.
- Matthew D. Zeiler and Rob Fergus. Visualizing and Understanding Convolutional Networks. In *European Conference on Computer Vision (ECCV)*, 2014.
- Hongyang Zhang, Yaodong Yu, Jiantao Jiao, Eric P Xing, Laurent El Ghaoui, and Michael I Jordan. Theoretically principled trade-off between robustness and accuracy. *arXiv*, 2019a.
- Hongyang Zhang, Yaodong Yu, Jiantao Jiao, Eric P. Xing, Laurent El Ghaoui, and Michael I. Jordan. Theoretically principled trade-off between robustness and accuracy. In *International Conference on Machine Learning (ICML)*, 2019b.
- Jingfeng Zhang, Xilie Xu, Bo Han, Gang Niu, Lizhen Cui, Masashi Sugiyama, and Mohan Kankanhalli. Attacks Which Do Not Kill Training Make Adversarial Learning Stronger. In *International Conference on Machine Learning (ICML)*, 2020.
- Jingfeng Zhang, Jianing Zhu, Gang Niu, Bo Han, Masashi Sugiyama, and Mohan Kankanhalli. Geometry-aware Instance-reweighted Adversarial Training. In *International Conference on Learning Representations (ICLR)*, 2021.

- Kai Zhang, Wangmeng Zuo, Yunjin Chen, Deyu Meng, and Lei Zhang. Beyond a Gaussian Denoiser: Residual Learning of Deep CNN for Image Denoising. *IEEE Transactions on Image Processing*, 2017a.
- Kai Zhang, Wangmeng Zuo, and Lei Zhang. FFDNet: Toward a Fast and Flexible Solution for CNN based Image Denoising. *IEEE Transactions on Image Processing*, 2018.
- Xingcheng Zhang, Zhizhong Li, Chen Change Loy, and Dahua Lin. Polynet: A pursuit of structural diversity in very deep networks. In *IEEE/CVF Conference on Computer Vision and Pattern Recognition (CVPR)*, 2017b.
- Yide Zhang, Yinhao Zhu, Evan Nichols, Qingfei Wang, Siyuan Zhang, Cody Smith, and Scott Howard. A Poisson_gaussian Denoising Dataset with Real Fluorescence Microscopy Images. In *IEEE/CVF Conference on Computer Vision and Pattern Recognition (CVPR)*, 2019c.
- Zhong-Qiu Zhao, Peng Zheng, Shou-tao Xu, and Xindong Wu. Object detection with deep learning: A review. *IEEE Transactions on Neural Networks and Learning Systems*, 2019.
- Chen Zhu, Yu Cheng, Zhe Gan, Siqi Sun, Tom Goldstein, and Jingjing Liu. Freelj: Enhanced adversarial training for natural language understanding. *arXiv*, 2019.
- Daniel Zoran, Mike Chrzanowski, Po-Sen Huang, Sven Gowal, Alex Mott, and Pushmeet Kohli. Towards robust image classification using sequential attention models. In *IEEE/CVF Conference on Computer Vision and Pattern Recognition (CVPR)*, 2020.